ISSN 1343-2230

CNS-REP-100
March, 2022

Annual Report 2020

Center for Nuclear Study,
Graduate School of Science, the University of Tokyo

Editor
Hiroki Nagahama

Center for Nuclear Study

CNS Reports are available from:
Wako-Branch at RIKEN
Center for Nuclear Study,
Graduate School of Science, the University of Tokyo
2-1 Hirosawa, Wako
351-0198, Japan
Tel: +81-48-464-4191
Fax: +81-48-464-4554

Annual Report 2020

Center for Nuclear Study,
Graduate School of Science, the University of Tokyo

Preface

This is the annual report of the Center for Nuclear Study (CNS), Graduate School of Science, the University of Tokyo, for the fiscal year 2020 (April 2020 through March 2021). During this period, a lot of research activities in various fields of nuclear physics have been carried out and a wide variety of fruitful results have been obtained at CNS. This report summarizes such research activities. I hereby mention some highlights of the report.

The Center for Nuclear Study (CNS) aims to elucidate the nature of nuclear system by producing the characteristic states where the Isospin, Spin and Quark degrees of freedom play central roles. These researches in CNS lead to the understanding of the matter based on common natures of many-body systems in various phases. We also aim at elucidating the explosion phenomena and the evolution of the universe by the direct measurements simulating nuclear reactions in the universe. In order to advance the nuclear science with heavy-ion reactions, we develop AVF upgrade, CRIB and SHARAQ facilities in the large-scale accelerators laboratories RIBF. The OEDO facility has been developed as an upgrade of the SHARAQ, where a RF deflector system has been introduced to obtain a good quality of low-energy beam. A new project for fundamental symmetry using heavy RIs has been starting to install new experimental devices in the RIBF. We promote collaboration programs at RIBF as well as RHIC-PHENIX and ALICE-LHC with scientists in the world, and host international meetings and conferences. We also provide educational opportunities to young scientists in the heavy-ion science through the graduate course as a member of the department of physics in the University of Tokyo and through hosting the international summer school.

The NUSPEQ (NUclear SPectroscopy for Extreme Quantum system) group studies exotic structures in high-isospin and/or high-spin states in nuclei. The CNS GRAPE (Gamma-Ray detector Array with Position and Energy sensitivity) is a major apparatus for high-resolution in-beam gamma-ray spectroscopy. Missing mass spectroscopy using the SHARAQ is used for another approach on exotic nuclei. The group plays a major role in the OEDO/SHARAQ project described below. In 2020, analysis of a new measurement of the ^{4}He(^{8}He, ^{8}Be)4n reaction for better statistics and better accuracy has been proceeding.

The main activity of the nuclear astrophysics group is to study astrophysical reactions and special nuclear structure, such as clusters, using the low-energy RI beam separator CRIB. To produce RI beams at CRIB with higher intensity, a project to improve the heat durability of the cryogenic gas target is in progress. In 2020, we used a high-current oxygen beam to test the heat durability of the gas target. Sealing foils of several materials and copper extention parts were employed in the test, and we have proven that the target can stand for the beam heat much exceeding the previous limit of 2 Watts per foil. The secondary beam development is also on going. A ^{6}He RI beam was first produced at CRIB in Mar. 2021, as the lightest RI beam ever created at CRIB. We successfully produced a ^{6}He beam at the intensity more than 10^5 pps, which is to be used for the approved ^{6}He+p scattering measurement, as well as other future experiments.

Main goal of the quark physics group is to understand the properties of hot and dense nuclear matter created by colliding heavy nuclei at relativistic energies. The group has been involved in the PHENIX experiment at Relativistic Heavy Ion Collider (RHIC) at Brookhaven National Laboratory, and the ALICE experiment at Large Hadron Collider (LHC) at CERN. As for ALICE, the group has involved in the data analyses, which include the measurement of low-mass lepton pairs in Pb-Pb collisions, the measurement of long range two particle correlations in p-Pb collisions, searches for thermal photons in high multiplicity pp and p-Pb collisions and for strangeness dibaryons. The group has involved in the ALICE-TPC upgrade using a Gas Electron Multiplier (GEM), where the group is very active in the development and benchmarking of the online space-charge distortion corrections using machine learning techniques running on the Graphical Processing Unit (GPU).

The Exotic Nuclear Reaction group studies various exotic reactions induced by beams of unstable nuclei. One subject is inverse-kinematics (p,n) measurement by using the neutron counter array PANDORA. Candidate nuclei to study are high spin isomers such as ^{52}Fe(12^+). Study of the production mechanism of high-spin isomer beams was in progress. Another is search of double Gamow-Teller resonance by a double charge exchange reaction (^{12}C,^{12}Be). Preparations including the development of MWDCs were ongoing.

The OEDO/SHARAQ group pursues experimental studies of RI beams by using the high-resolution beamline and the SHARAQ spectrometer. A mass measurement by TOF-Bρ technique for very neutron-rich nuclei successfully reaches titanium isotopes at N = 40, ^{62}Ti, of which the report was published in 2020. The experimental study of 0 ⁻ strength in nuclei using the parity-tansfer charge exchange (^{16}O, ^{16}F) will be reported soon. As for The OEDO beamline, the results of the first and second experiments for LLFPs will be finalized and reported soon. Since experimental studies using OEDO were newly proposed, we continue developments to improve the performance for coming these beam times, such as the intensity of low-energy RI beams and the suppression of X rays from RF deflector.

Three gaseous active target TPCs called CAT-S, CAT-M and GEM-MSTPC are developed and used for the missing mass spectroscopies. The CAT ' s are employed for the study of equation of state of nuclear matter. The measurement of giant monopole resonance in ^{132}Sn at RIBF with CAT-S and the data analysis is ongoing. The CAT-M was employed for the measurements of the proton inelastic scattering on Xe-136 at HIMAC and the proton elastic scattering on Sn-132. The development for the reduction of space charge due to the ion backflow and the reduction of delta-ray background is ongoing. The GEM-MSTPC is employed for the nuclear astrophysics study. The data analysis of (α, p) reaction on ^{18}Ne and ^{22}Mg and the β-decay of ^{16}Ne followed by α emission are ongoing.

A recoil particle detector for missing mass spectroscopy, named TiNA, had been upgraded under the collaboration with RIKEN and RCNP. The original TiNA consisted of 6 sector telescopes and 12 CsI (Tl) crystals. Four TTT-type (1024 channels) doubly-sided silicon detectors and twenty-two CsI(Tl) were added to make a TiNA2 array. The commissioning experiment of the TiNA2 was conducted at Kyushu University in January 2021. To improve the properties of the ionization chamber of the S1 focal plane detector, the electron mobility of the gas has been studied at the offline test bench. The production cross sections of ^{178m2}Hf were evaluated for the mass production in the future and will be reported soon. The digital signal processing devices for the GRAPE are under development. For the SHARAQ11 experiment which uses a tritium-doped titanium target, the safety devices has been developed with Tohoku University.

One of the major tasks of the accelerator group is the AVF upgrade project that includes development of ion sources, upgrading the AVF cyclotron of RIKEN and the beam transport system to CRIB, E7B, and C12 in the E7 experiment room. In the fiscal year 2020, the operating time of the HyperECR was 1137 hours. The beam extraction system of the HyperECR is developed to realize a high intensity and low emittance beam and the study of mixing gas is started for heavy ionization. The calculation model of injection beam orbit of the AVF cyclotron was completed and the longitudinal motion of injection beam orbit was studied. For the detailed studies on ion optics of the beamline to CRIB and experiment device of Fr-EDM measurement from AVF cyclotron, the development of 4-dimensional emittance monitor for high power ion beams was started and the prototype was completed and evaluated for performance.

The development of an optical lattice (OL) interferometer to search for a permanent electric dipole moment (EDM) with Francium (Fr) atoms is now in progress at RIKEN. The newly developed surface ionizer can produce the stable ^{210}Fr ions with about 10^6 Fr$^+$/s using the nuclear fusion reaction by a high intensity primary beam of ^{18}O supplied from the AVF cyclotron. We are now moving to the experimental phase to trap the Fr in the magneto-optical trap and OL to realize the cold Fr source with 10^7 atoms to measure the EDM. In parallel, the high intensity ^{225}Ac source, which is utilized as the generator for the ^{221}Fr, was developed successfully. The comparison of the EDM between ^{210}Fr and ^{221}Fr can be used to distinguish the origin of the CP violation such as the electron EDM, quark color charge EDM, and CP violation interactions.

The nuclear theory group participates in a project, “Program for Promoting Researches on the Supercomputer Fugaku” and promotes computational nuclear physics utilizing the Fugaku supercomputer. In FY2020, we proposed a new framework called the “quasi-particle vacua shell model”, which is an extension of the Monte Carlo shell model, and promoted its code developments. Based on these methodological developments, we investigated the exotic structure of nuclei, especially neutron-rich Mg isotopes, and discussed the mechanism to determine the neutron drip line. In addition, the nuclear Schiff moments of ^{129}Xe and ^{199}Hg were theoretically evaluated by large-scale shell-model calculations to contribute to the experimental search of time-reversal breaking. In parallel, we promoted the collaborative researches with experimental groups for investigating the exotic structure of unstable nuclei, such as ^{35}S, ^{30}Mg, ^{64}Ni, ^{75}Ni, ^{112}Sn and ^{137}Ba.

The 19th CNS International Summer School named A3F-CNSSS20 was organized in August 2020. The school was jointly hosted by CNS and the A3-Foresight program, and supported by RIKEN Nishina Center and ANPhA. Because of the pandemic of COVID-19, the school was held online. In addition to the participants from China, Korea and Vietnam, many participants from other countries such as Malaysia and India attended. Many invited lecturers including one foreign distinguished physicist gave classes.

Finally, I thank Ms. Shimane and other administrative staff members for their heartful contributions throughout the year.

Susumu Shimoura
Director of CNS
S. Shimoura

Table of Contents

1a. Experimental Nuclear Physics: Low and Intermediate Energies

1b. Experimental Nuclear Physics: PHENIX Experiment at BNL-RHIC and ALICE Experiment at CERN-LHC

2. Accelerator and Instrumentation

3. Theoretical Nuclear Physics

4. Other Activities

Appendices

Experimental Nuclear Physics: Low and Intermediate Energies

Surrogate reactions for neutron capture reaction

N. Imai, M. Dozono, S. Michimasa, S. Ota, T. Sumikama[a], D. Suzuki[a], O. Beliuskina, S. Hayakawa, C. Iwamoto, K. Kawata, N. Kitamura, S. Masuoka, P. Schrock, H. Shimizu, S. Shimoura, K. Wimmer[1b], K. Yako, H. Yamaguchi, L. Yang, N. Chiga[a], D. Nagae[a], S. Omika[a], H. Otsu[a], H. Sakurai[a], K. Yamada[a], S. Takeuchi[c], H. Miki[c], H. Yamada[c], S. Kawase[d], K. Nakano[d], Y. Watanabe[d], K. Iribe[e], T. Teranishi[e], N. Aoi[f], E. Ideguchi[f], H.J. Ong[f], R. Yanagihara[f]

Center for Nuclear Study, Graduate School of Science, University of Tokyo
[a]RIKEN Nishina Center
[b]Department of Physics, Univ. of Tokyo
[c]Tokyo Insititute of Technology
[d]Department of Advanced Energy Science and Engineering, Kyushu Univ.
[e]Department of Physics, Kyushu Univ.
[f]RCNP, Osaka Univ.

The neutron capture reaction cross-sections are important for understanding the origin of the elements in the universe as well as the nuclear engineering. In some cases, the target nuclei are short-lived so that the measurement of the cross section is not feasible.

^{79}Se is one of such nuclei. The nucleus is located on the path of s-process nucleosynthesis. Because the first excited state has a β decay branch, the ratio of the daughter nucleus ^{79}Br to ^{80}Se can determine the temperature when the s-process took [1]. However, although the main path of the s-process is the neutron capture to proceed to ^{80}Se, because ^{79}Se is radioactive the neutron capture cross section on ^{79}Se has not been measured directly.

The nucleus is also known as the one of the long-lived fission products (LLFPs) of the nuclear wastes. It is supposed to be stored for millions of years in the deep geological repository, which has not been determined yet in Japan [2]. The transmutation of such LLFPs would be a possible way to avoid the inheriting of the nuclear waste to the future. To design the facility for the transmutation, cross sections of any neutron induced reactions must be evaluated precisely.

In the past, the neutron capture cross section was evaluated by measuring the photon strength function [3]. The neutron capture was deduced from the strength function assuming the level density, which are strongly model-dependent. As a result the evaluated cross section have a large uncertainty of a factor 7.

To evaluate the cross section of ^{79}Se(n,γ) independently, a surrogate ratio technique [4] was employed. In general, the compound neutron capture reaction is considered to be composed of two factors: the formation cross section of the compound states and the γ decay probability from the unbound states. The energy-dependent formation cross section can be obtained by using the global optical potential. On the other hand, the γ emission probability strongly depends on the nuclear structure of the nucleus. Once the γ emission probability is obtained experimentally, the neutron capture cross sections can be determined. In the surrogate method, the same unbound states as those populated by the compound reaction are assumed to be excited by an alternative nuclear reaction such as (*d, p*) reaction. In the case of (*d, p*) reaction, the excitation energy can be determined by measuring the recoiled protons. Therefore, when γ emission channel at each excitation energy is identified, the neutron capture cross section can be determined.

So far, for the surrogate ratio method, the γ emission probability was determined by measuring deexcitation γ rays which requires the decay scheme from the unbound state. On the other hand, in our new method, the probability was determined by measuring reaction residues in coincidence with the recoiled proton, instead of measuring γ ray. Our new technique is free from the small efficiency of detecting γ rays and statistical model to estimate the deexcitation from the unbound state. The transfer reaction in the inverse kinematics made feasible the measurement.

The secondary ^{77,79}Se beams were produced at RIBF by the in-flight fission of ^{238}U beams with a rotating Be target of 3 mm thickness. By tuning the thicknesses of the degraders at F1 and F2 the beam energy was adjusted to 120 MeV/nucleon at F5. The beam energy was further degraded with a thick Al degrader at F5 to 23 MeV/nucleon. The energy was further degraded to 20 MeV/nucleon at the secondary target by passing through the beam line detectors of parallel plate avalanche counte (PPAC)s. Diamond detectors of 3×3 cm^2 and 300 μm thickness were placed at F3 and F5 to measure the timing when the beam passed through. The small active area of the diamond limited the momentum slit at F1 $\pm1\%$. The parallel beam was made by the super conducting triplet quadrupole magnet at FE10, where the RF deflector is installed.

Two PPACs were installed upstream of the secondary target, FE12, to register the timing and the trajectory of the beams on the target. Time of flight (TOF) between F5 and FE12 was measured to identify the beam and the respective beam energy. The RF deflector at OEDO decreased the beam spot in a diameter of 2 cm (σ) at a deuterated polyethylene CD$_2$ target of 4 mg/cm^2 thickness. The target size was 3 cm in diameter. The recoiled particles of (d,p) reactions were detected by six telescopes, each of which consisted of SSD at the first layer and two CsI(Tl)s detectors

[1] Present Address:GSI, Darmstdt, Germany

at the second layer. The telescope covered the scattering angles from 100 to 150 degrees in the laboratory frame. The SSD was divided to 16 channels in polar angle. The momenta of the outgoing nuclei were analyzed by the first part of the SHARAQ spectrometer. At the exit of the D1 magnet of the spectrometer, two PPACs and an ionization chamber were installed as the focal plane detectors. PPACs gave us the TOF of ions. The trajectory obtained from PPACs also gave the $B\rho$ values of the residual nuclei. The ionization chamber yielded the energy loss (dE) and the range in the gas. The TOF-dE-range and $B\rho$ information enables us to identify the ions.

In the surrogate ratio method, the spin distribution of the reference nucleus is required to be the same as that of the reaction of the interest. In the present case the ground state spin parity of ^{77}Se is $1/2^-$, while that of ^{79}Se is $7/2^+$. The spin distributios of the neutron capture reactions are compared to those of the transfer reaction in Fig. 1. The panel (a) shows spin distributions for the neutron capture reactions on ^{79}Se($7/2^+$) (solid) and the isomeric state of ^{79}Se($^*1/2^-$) (dashed) with 0.2 MeV. The spin distribution on the isomeric state centers around $J = 2$. The panel (b) compares the spin distributions on ^{77}Se ground state of $1/2^-$ (solid) and the isomeric state of $7/2^+$ (dashed). These two figures clearly demonstrate that the spin of the target nuclei are important to determine the cross sections by the surrogate ratio method. The panel (c) presents the spin distributions of the transfer reactions on the ground states of ^{77,79}Se by dashed and solid lines, respectively. The spin distribution are found to be the same, indicating that the contamination of the isomeric states in ^{77,79}Se beams won't affect the final result.

The final neutron capture cross section was deduced by using the γ emission probabilities. The manuscript summarizing the result will be submitted soon.

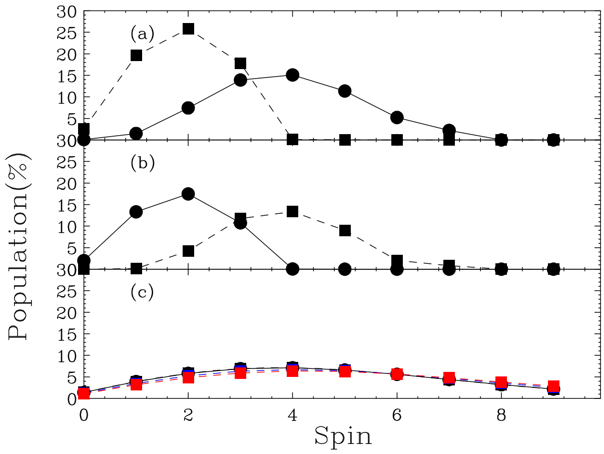

Figure 1. The spin distribution of nuclear reactions. (a) those for neutron capture reactions on ^{79}Se(g.s.) (solid) and the isomeric state (dashed). (b) those for neutron capture reactions on ^{77}Se(g.s.) (solid) and the isomeric state (dashed). (c) those for neutron transfer reactions on ^{77}Se(g.s) (dashed) and ^{79}Se(g.s.) (solid). See the text for details.

Acknowledgment

The work was funded by ImPACT Program of Council for Science, Technology and Innovation (Cabinet Office, Government of Japan).

References

[1] F. Kappler, H. Beer, and K. Wisshak, Rep. of Prog. in Phys. 52, 945 (1989).

[2] https://www.numo.or.jp/en/ .

[3] A. Makinaga et al., Phys. Rev. C **94**, 044304 (2016).

[4] J. E. Escher et al., Rev. of Mod. Phys. 84, 353 (2012).

Commissioning of the Si and CsI detector array TiNA

B. Mauss, N. Ma[a], J.W. Hwang[a,b], D. Suzuki, N. Imai[a], T. Teranishi[c] S. Ota[a], A. Kohda[d], M. Dozono[a], S. Michimasa[a], T. Sumikama, C. Iwamoto, N. Iwasa[e]

RIKEN (The Institute of Physical and Chemical Research)
[a] Center for Nuclear Study, Graduate School of Science, University of Tokyo
[b] Center for Exotic Nuclear Studies, Institute for Basic Science
[c]Department of Physics, Kyushu University
[d]Research Center for Nuclear Physics, Osaka University
[e]Department of Physics, Tohoku University

The energy-degrading beamline OEDO was built at RIBF to increase the scope of reactions available for the study of radioactive nuclei. Beam energies can be degraded down to few tens of MeV per nucleon, where transfer reactions become relevant for the study of nuclear structure and of nucleosynthesis processes [1]. In this context, the Si and CsI detector array TiNA was designed for the detection of recoil nuclei from transfer reactions [2] at OEDO. It has been used in several transfer experiments [3, 4].

The TiNA detector was upgraded in 2020 to increase the solid angle and improve the resolution in angle and energy [5]. The upgraded TiNA consists of two types of detector assemblies. The first detector assembly consists of four 300 μm thick Micron TTT2-type Double sided Strip Silicon Detectors (DSSD), each followed by four 25 mm thick CsI crystals in a 2×2 matrix to cover the $100 \times 100\,\mathrm{mm}^2$ active area. The DSSDs are arranged in a barrel configuration and placed close to the reaction target. The second detector assembly is a lampshade array consisting of six trapezoidal telescopes. Each has a 300 μm thick, Micron YY1-type, Single sided Strip Silicon Detectors (SSSD) followed by a total of three trapezoidal shape CsI crystals with a thickness of 25 mm. The second assembly is placed further away to extend the angular coverage toward the beam axis. The total angular coverage by all telescopes ranges from 10° to 80° in the laboratory frame, with an angular resolution better than 0.8° for the square telescopes and better than 1.2° for the lampshade array. The chamber will be rotated by 180 ° to cover the backward angles from 100° to 170° for (d,p) transfer reactions in inverse kinematics at OEDO.

For the data taking, two different systems were unified. First, the DSSDs are connected to the General Electronics for TPCs (GET), an integrated system allowing the processing of the 1024 channels. The test of the GET electronics is reported elsewhere [5]. The signals from the rest of the detectors including the CsI crystals and the SSSD are fed into standard analog amplifiers and digitized by VME-standard ADC modules. Triggers from both systems are currently merged in a trigger module. A common trigger is sent to both data acquisition (DAQs) systems and synchronizes the event number. Timestamps for both systems were also recorded.

After a benchmark test of the full setup using a standard ^{241}Am alpha source at RIKEN RIBF, the detector was commissioned in-beam at the tandem accelerator facility of the Center for Accelerator and Beam Applied Science, Kyushu University. One of the goals of this commissioning was to test the performances of the DAQ systems, in particular the event correlation between the two DAQ systems and the maximum trigger rate that can be accepted. Another goal was to test the in-beam energy and angular resolution of the detector with various light ions over a wide range of energies and verify the particle identification capabilities of the system.

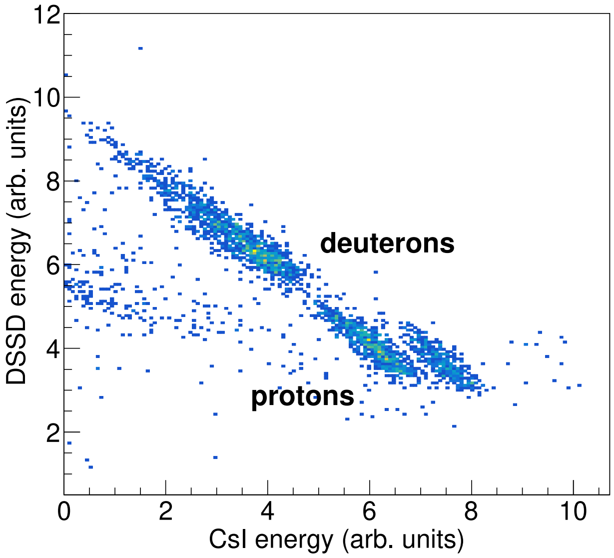

Figure 1. E–ΔE plot of the energies measured by DSSD and CsI detectors. Protons and deuterons are identified. The different cluster correspond to different reaction kinematics. Preliminary results.

Deuteron beams at 14 MeV and 11.8 MeV impinged on a 1 mg/cm^2 $^{\mathrm{nat}}$C target provided by the RCNP, Osaka University. In addition to elastic scattering, inelastic scattering to excited states and transfer (d,p) and (d,α) reactions are also allowed with this beam energy. It will allow to evaluate the particle identification capabilities, the detector energy resolution for various particles and the angular resolution. Part of protons and deuterons punch through the DSSDs and hit the CsI detectors. Figure 1 shows an E–ΔE plot for such particles using the energy information taken by the DSSDs and CsI detectors. The protons and deuterons are well differentiated in separate loci, demonstrating the good quality of the particle identification. This also confirms that the

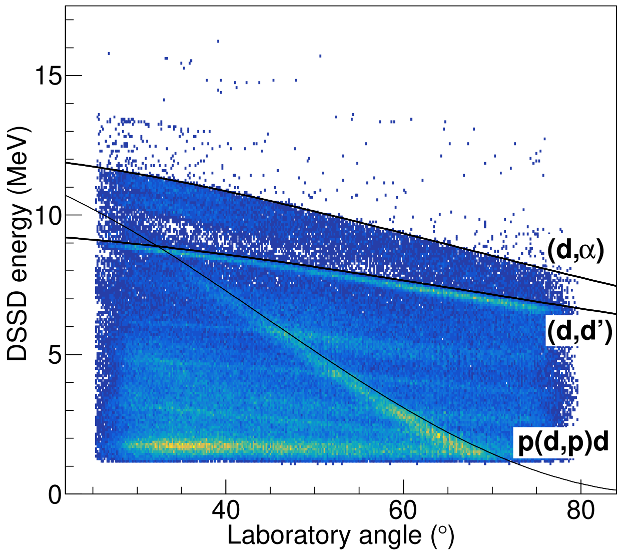

Figure 2. A scattered plot of total kinetic energy vs. emission angles measured by the DSSDs. In black are three theoretical lines. The energy was not corrected for the energy loss in the reaction target and in the dead zone of the DSSDs. The loci seen in the figure are thus lower in energies compared to the calculated kinematical curves. Preliminary results.

event correlation was correctly carried out between the two data acquisition systems. To test the trigger rate, several data were taken by varying beam intensities. The maximum trigger rate of about 600 Hz was achieved with a live time of 85%.

A scattered plot of total kinetic energies against emission angles is shown in Fig. 2 and compared to the theoretical kinematical curves for inelastic scattering to the first 2^+ state at 4.4 MeV and for the ^{12}C(d,α)^{10}B reaction to the ground state of ^{10}B. Since the energy loss in the target is not corrected for this plot, the energies of the loci seen in the data are found lower than the kinematical curves. A distinct locus visible at lower energies is attributed to the ^{1}H(d,p)d reaction. This background was likely generated from a deposit of water or organic molecules to the target surface. The excitation energy resolution is estimated to be 141 keV FWHM for the first 2^+ state of ^{12}C via inelastic scattering. For better resolutions, the analysis is still ongoing to improve the calibrations by estimating the energy loss in the dead zone of the DSSDs.

In conclusion, the full setup of the TiNA detector was successfully commissioned at the tandem accelerator facility of the Kyushu University. The event correlation between the two independent data acquisition systems was validated. A trigger rate of 600 Hz was achieved in this commissioning. We were limited in data flow from the GET electronics and we expect to improve this performance. The treatment of the data flow will be accelerated by installing the DAQ on a server and use optical fiber for data transport. The preliminary results from the data analysis help evaluate the performance of particle identification and excitation energy resolution. There is still room to further improve the energy resolution by reducing the noise level in-beam to the level measured during the α-source test at RIKEN RIBF.

References

[1] S. Michimasa *et al.*, Prog. Theor. Exp. Phys. 2019, 043D01

[2] P. Schrock *et al.*, CNS Annual Report 2016, CNS-REP-**96**, 7-8 (2017).

[3] K. Wimmer *et al.*, CNS Annual Report 2017, CNS-REP-**97**, 7 (2019).

[4] N. Imai *et al.*, CNS Annual Report 2018, CNS-REP-**98**, 1-2 (2020).

[5] B. Mauss *et al.*, CNS Annual Report 2019, CNS-REP-**19**, 13-14 (2021).

Search for tetra-neutron resonance
- Re-measurement of the $^{4}He(^{8}He,^{8}Be)$ reaction -

S. Masuoka, S. Shimoura, M. Takaki, S. Ota, S. Michimasa, M. Dozono, C. Iwamoto, K. Kawata, N. Imai, N. Kitamura, M. Kobayashi, R. Nakajima, H. Tokieda, R. Yokoyama, D. S. Ahn[a], H. Baba[a], N. Fukuda[a], T. Harada[b], E. Ideguchi[c], N. Inabe[a], Y. Kondo[d], T. Kubo[a], Y. Maeda[e], F. M. Marqués[f], M. Matsushita, T. Nakamura[d], N. Orr[f], H. Sakai[a], H. Sato[a], P. Schrock, L. Stuhl[b], T. Sumikama[a], H. Suzuki[a], H. Takeda[a], K. Taniue[e], T. Uesaka[a], K. Wimmer[g], K. Yako, Y. Yamaguchi, Y. Yanagisawa[a], K. Yoshida[a], and J. Zenihiro[a]

Center for Nuclear Study, the University of Tokyo
[a]RIKEN Nishina Center
[b]Department of Physics, Toho University
[c]Research Center for Nuclear Physics, Osaka University
[d]Department of Physics, Tokyo Institute of Technology
[e]Faculty of Engineering, Univ. of Miyazaki
[f]Laboratorie de Physique Corpusculaire, IN2P3-CNRS, ENSICAEN et Université de Caen
[g]Department of Physics, the University of Tokyo

In our previous study, the candidate resonance of the 4n system (tetra-neutron) was determined using the $^{4}He(^{8}He,^{8}Be)4n$ reaction with a 186 MeV/nucleon ^{8}He beam [1]. A new measurement with better statistics and better accuracy was performed to confirm the existence of the tetra-neutron system [2].

The intensity of the ^{8}He beam was 3.5×10^{6} particles per second at the liquid helium target, which was approximately twice compared to that of the previous experiment. Low pressure multi-wire drift chambers (LP-MWDCs) were installed at the focal planes F3, F6, and F-H10(S0), to measure the trajectory and momentum of the beam. The time reference to determine the drift time in LP-MWDCs was obtained from a plastic scintillator at F3.

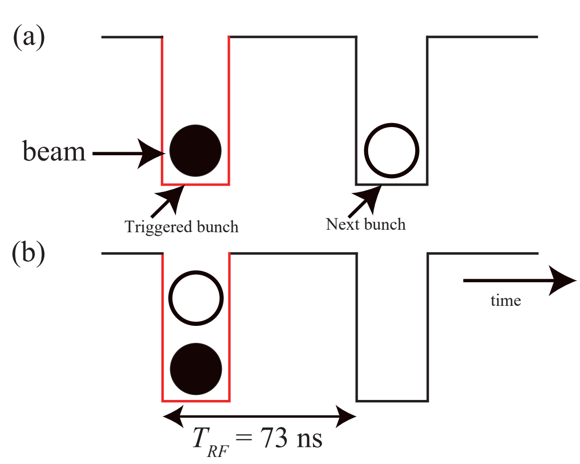

Figure 1. Time structure of the beam bunch. The solid circles show particles triggering data acquisition, and the open circles are accidental particles. (a) Beam contains both the 'Triggered bunch' and 'Next bunch'. (b) Two particles are in the triggered bunch.

We present the analysis of the LP-MWDCs developed to eliminate accidental coincidence events induced by the high intensity beam. The ^{8}He beam from the SRC had a bunch structure with a periodic cycle of 73 ns. There are two cases of accidental coincidence as illustrated in Fig. 1(a) and (b). The filled circles represent the particle, which triggered the data acquisition. The other particle in the next bunch (open circle) hits in (a), whereas two particles together hit in the same bunch in (b). In the analysis, we carefully treated these events, which created multiple hits within the maximum drift time of 120 ns in the LP-MWDCs. The events of Fig. 1(a) were successfully identified by selecting the drift-time region of the LP-MWDC and the total traveling time from F3 to S2 focus corresponding to the beam energy.

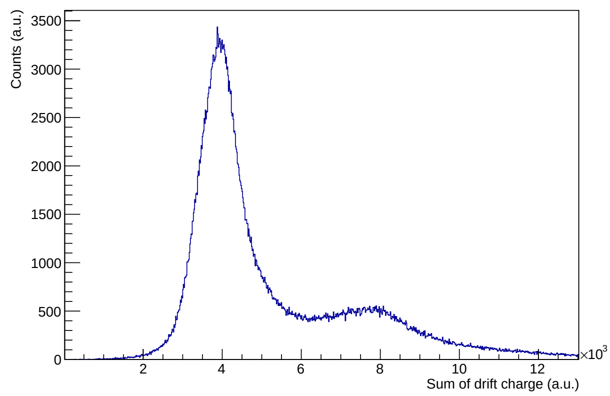

Figure 2. Energy distribution of LP-MWDC.

In the case of Fig. 1(b), we simply eliminated such events because the triggered beam particle and accidental particle in the same bunch cannot be distinguished. To identify such cases, we extracted the total energy spectrum obtained by using the Time-Over-Threshold data of its signal. Figure 2 shows the total energy distributions measured at LP-MWDC; two peaks are visible. The peak at higher energies results from multiple-hit events, and 75% of the multiple hit events were rejected by selecting energies below 6,000.

This value is consistent with the probability of an occurrence of pile up events.

After the pile-up rejection, the tracking efficiency of the beam was 95%. In this experiment, although one LP-MWDC installed at F-H10 was damaged under intense irradiation of the ^{8}He beam and operated with a low efficiency of 48%, we try to recover the lost tracking events by using the ion-optical analysis. The image(x_T, y_T) and incident angle(a_T, b_t) at the target is described by F3 tracking (x_3, y_3, a_3, b_3) and momentum of the beam δ:

$$
\begin{aligned}
x_T &= (x|x)x_3 + (x|a)a_3 + (x|aa)a_3^2 \\
&+ (x|\delta)\delta + (x|a\delta)a_3\delta, \\
a_T &= (a|x)x_3 + (a|a)a_3 + (a|aa)a_3^2 \\
&+ (a|\delta)\delta + (a|a\delta)a_3\delta, \\
y_T &= (y|y)y_3 + (y|b)b_3 + (y|bbb)b_3^3 + (y|b\delta)b_3\delta, \\
b_T &= (b|b)b_3
\end{aligned}
$$

. The transfer matrix between the F3 and the F-H10 was obtained by using low intensity triton beam data. To derivative the target image without using LP-MWDCs at F-H10, it is required to detect both the focal plane image of the F3 (initial tracking of the beam) and the F6 (measure the momentum of the beam) in the same event. Then, a tracking of the target is derived by using upper equations. The overall tracking efficiency of the ^{8}He beam is estimated 80%, which still ensures better statistics than the previous experiment.

Data analysis is now in progress.

References

[1] K. Kisamori et al., Phys. Rev. Lett. **116**, 052501 (2016).
[2] S. Masuoka et al., CNS Ann. Rep. **2017**, 25 (2019)

Effect of the angular momentum transfer in projectile fragmentation

Keita Kawata [a,b], Shinsuke Ota [a], Masanori Dozono [a], Juzo Zenihiro [b], Chihiro Iwamoto [a], Noritaka Kitamura[a], Hideyuki Sakai[b], Shoichiro Masuoka[a,b], Shin'ichiro Michimasa[a], Kentaro Yako[a], Tomoya Harada[b,c], Hiroki Nishibata[b], Rieko Tsunoda[a], Nobuaki Imai[a], Tomoya Sato[b], Jongwon Hwang[a], Ningtao Zhang[d], Fumitaka Endo [e]

[a] *Center for Nuclear Study,University of Tokyo*
[b] *Riken Nishina Center,*
[c] *Toho Universicity*
[d] *Institute of Modern Physics*
[e] *Tohoku University*

The projectile fragmentation is one of the most popular method to obtain unstable nuclei with high intensity and intermediate energy in flight. Projectile nuclei of several hundred MeV/u bombard with a production target, and beam-like fragments are used as unstable nuclei beam.

In general, the momentum distribution of fragment particle has the width and its width is mainly due to Fermi motion.

In the rest frame of the projectile the total momentum is equal to zero. Then the momentum distribution of fragment may become a symmetric distribution, which is described by Goldharber model(G.H. model) [1]. The width of the momentum can be derived from the total momentum conservation.

$$\sigma^2 = \sigma_0^2 \frac{A_f(A_p - A_f)}{A_p - 1} \tag{1}$$

Here, A_f and A_p show the mass number of fragment and projectile, σ_0 shows about 90 MeV/c.

However, the measured momentum distributions do not always obey this model, especially in their low-momentum side. This remains an open question. Phenomena appear that are unique to nuclear physics and cannot be explained kinematically.

In the G.H model the fragment stays in its ground state during the fragmentation process. However the long-lived excited states called isomeric state are produced with the projectile fragmentation. The production of isomeric state is natural when we consider the existence of intermediate state in two-stage fragmentation reaction process as shown in the Fig1, which is proposed in the Abrasion-ablation model developed from the G.H model.

When the fragment is excited, the fragment is thought to be gaining angular momentum. Until now, the Abrasion-ablation model has not clarified the relationship between momentum and angular momentum. Angular momentum may be a key to solve the open question mentioned above.

In order to investigate the relationship between angular momentum transfer and momentum, we will use high-spin isomers in the fragments. The reason for using isomers is as follows. By selecting isomeric state, the lowest average angular momentum of the intermediate state is cut off while all the angular momentum contribute to the production of ground state. This difference allow us to evaluate the effect of angular momentum transfer quantitatively by comparing the momentum distributions of the isomeric state and ground state. Projectile nuclei with finite angular momentum as well as 0^+ projectile enable us to control the value of the angular momentum transfer.

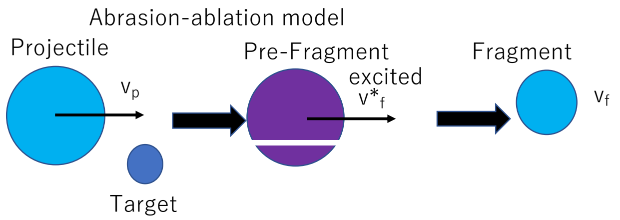

Figure 1. The figure shows the Abrasion-ablation model. The prefragment is de-excited by emitting gamma rays and nucleons. For this reaction process, the velocity difference between before and after the reaction do not necessarily coincide.

In this paper, we report a new systematic measurement of momentum distributions of the ground and isomers, aiming at the clarification of the angular momentum transfer in fragmentation reaction.

The experiment (the project number of H362) was performed at the SB2 course in HIMAC in Chiba. The primary beams of ^{58}Ni and ^{59}Co with 350 MeV/u, bombarded the production target of a14-mm thick ^{9}Be target. The fragments of ^{52}Fe, ^{53}Fe, ^{54}Co and contaminants are separated by two dipoles and momentum analyzed by a fragment separator consisting of two dipole magnets and quadrupole magnets. The isomeric state is identified by measuring the de-excitation γ rays. The detail of the experimental setup is reported in [2]

Figure 2 shows the momentum distribution of the production yield for the ground state and isomeric state ^{52}Fe, which is normalized with the primary beam. Triangle data points show the production ratio of ground state and square data points show the production ratio of isometric state in each figure.

The production yield of the isomers was multiplied by a factor of 100 for ^{58}Ni and by a factor of 10 for ^{59}Co. The momentum difference is set to 0 when the speed before and

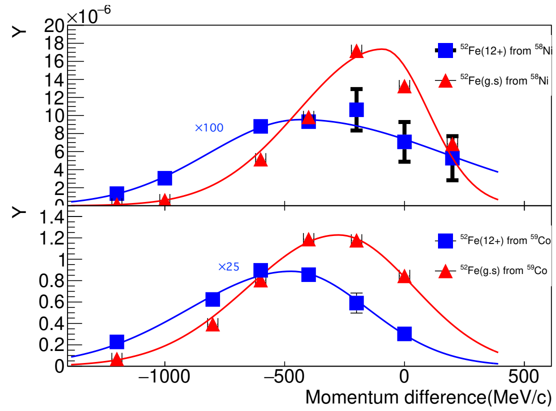

Figure 2. Top panel shows the result of production ratio of ^{52}Fe(12+) and ^{52}Fe(g.s) from ^{58}Ni with the momentum difference. Bottom panel shows the result of production ratio of ^{52}Fe(12+) and ^{52}Fe(g.s) from ^{59}Co.

after the reaction is the same as when the reaction occurs at the center of the target.

The momentum distributions show an asymmetric distribution which is different from the prediction of the G.H. model. The peak positions for isometric state and ground state are different from each other in both the projectile nuclei. This difference may originate from the effective angular momentum transfer to produce each state. To quantify the peak position, an asymmetric Gaussian distribution [3], which is described below, is fitted to the measured data points.

$$f(p) = \begin{cases} a_0 \exp(-\frac{(p-c)^2}{2\sigma_H^2}) & (p > c) \\ a_0 \exp(-\frac{(p-c)^2}{2\sigma_L^2}) & (p <= c) \end{cases}$$

We will discuss the relationship between difference(Δp) of peak position and the angular momentum transfer. When the nucleus in the ground state is an odd nucleus, it has a finite angular momentum. The angular momentum of the ground state of the fragment is expected to be neglected in calculating the angular momentum transfer, based on the following discussions. All the possible angular momentum transfer can contribute to produce the ground state even if the nuclear spin of the ground state is finite. This means that the peak position of the momentum distribution will be the same both for the zero-spin and finite-spin ground state. Assuming that the nuclei spin does not affect the momentum distribution, the angular momentum transfer is defined as the difference between the total angular momenta of the isomer (L_{iso}), the ground state($L_{g.s.}$) and the projectile (L_{proj}).

$$L_{trans} = L_{iso} - L_{g.s.} - L_{proj} \quad (2)$$

Figure 3 shows the correlation between Δp and L_{trans}. The solid line shows L_{trans}=r×Δp in the case of A=52 and r=1.2A$^{1/3}$.

Each data point is close to the solid line representing the classical angular momentum transfer, indicating that there

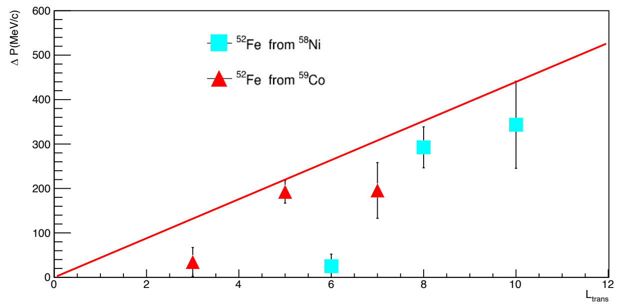

Figure 3. L_{trans} vs Δp plot. Solid line shows the calculation from the classical kinematically relationship between angular momentum and momentum.

is a correlation between the measured linear momentum shift Δp and the angular momentum(L_{trans}).

However, the data point of ^{54}Co with L_{trans}.=3,6 is out of this correlation. In the case of ^{54}Co, the excitation energy is 200 keV, which is very small and lower than that of the other isomers, and it is thought that transitions to isomer can be allowed from higher states where angular momentum of pre-fragment is lower than the isomeric state.

The momentum distributions of isomeric state and ground states of three fragments were measured with two projectiles in this study. The momentum distributions of isomers and ground states were different in each nuclei except for the ^{54}Co. The cut off of the lowest angular momentum affect the peak position of the momentum distribution , and the difference can be explained by classical kinematic theory. The angular momentum of the projectile also affects the momentum distribution of the isomer, suggesting that the angular momentum is responsible for a part of the low-momentum component of the momentum distribution in the ground state, which has not been explained.

References

[1] A.S. Goldhaber *et al.*, Physics Letters **B53** 306 - 308(1974).
[2] K.Kawata *et al.*, CNS Annual report (2019)
[3] M. Notani *et al.*, Phys. Rev. C.**15** ,044605(2007).

First production of ^{6}He beam at CRIB

H. Yamaguchi, M. Sferrazza[a], S. Hayakawa, N.R. Ma, H. Shimizu, K. Okawa, T. Furuno[b], S. Okamoto[c], N. Imai, T. Chillery, J.T. Li, S. Ota, N. Iwasa[d], T. Kawabata[b]

Center for Nuclear Study, Graduate School of Science, the University of Tokyo
[a]*Department of Physics, Université Libre de Bruxelles*
[b]*Department of Physics, Osaka University*
[c]*Department of Physics, Kyoto University*
[d]*Department of Physics, Tohoku University*

^{6}He is the second lightest unstable nuclide that could be used as a radioactive-isotope (RI) beam. In 2021, we performed a production test of ^{6}He beam at CRIB [1–4] for the first time, aiming to assess the feasibility of future experiments using this RI beam. Various studies are expected to be feasible with the low-energy ^{6}He beam at CRIB. Presently we are interested in the investigation of the interplay between the halo nucleus structure of ^{6}He and the scattering properties in the ^{6}He+p [5] reactions, where the neutron transfer reactions, and the effects of the break-up mechanism and resonance will be probed in detail. Further studies using this exotic beam will be performed, involving both light and heavy targets. In particular, the effect of both weakly-bound beam and target will untangle interesting properties of the halo structure and of the break-up process. Reactions of the halo nucleus ^{6}He with a heavy target have been studied [6,7] and they confirmed an enhancement of the break-up.

Our approved proposal of the ^{6}He+p measurement [5] assumed a ^{6}He beam with an energy around 5–10 MeV/u and an intensity more than 10^{5} pps. The main purpose of the present work was to investigate the experimental parameters for an optimized beam production at CRIB. Considering the present limitation of the magnetic field at the CRIB, the maximum energy of the ^{6}He beam that can be separated with CRIB is about 8 MeV/u. The beam production was performed as a Machine Study beamtime in March, 2021. The primary beam was ^{7}Li^{3+}, accelerated with the AVF cyclotron up to an energy of 8.3 MeV/u. The maximum beam current at the entrance of CRIB during the beamtime was 3 pμA (= 9 eμA). The RI beam was produced with the ^{7}Li(d,^{3}He)^{6}He reaction, which was also used in other in-flight facilities, such as RESOLUT of Florida State University [8]. At RESOLUT, a ^{6}He beam was produced with an energy range of 18–29 MeV (3–5 MeV/u), an intensity of 10^{4} pps, and a purity of 40%. The target gas we used at CRIB was D_2 at 730 Torr, confined in a 80-mm-long cell, and cooled to 90K with the cryogenic gas target system [3].

We tested the beam production at two magnetic rigidity conditions: 1) Bρ=1.227 Tm (^{6}He^{2+}: 7.99 MeV/u) with the original primary beam, and 2) Bρ=1.032 Tm (^{6}He^{2+}: 5.66 MeV/u) by degrading the primary beam energy to 6.5 MeV/u with a 48-μm-thick Havar foil. Particle identification (PI) was performed by measuring the time-of-flight and energy of the secondary beam with the PPACs and silicon detectors at the F2 and F3 focal planes. Fig. 1 shows the

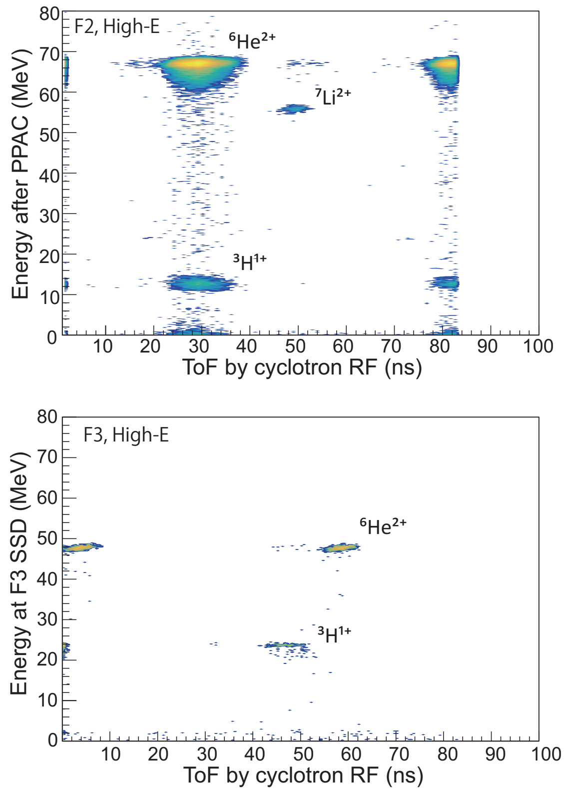

Figure 1. (Color online) PI diagrams of the secondary beams at F2 (top) and F3 (bottom), in the high-energy condition (Bρ =1.227 Tm).

PI diagrams at F2 (PPAC+SSD) and F3 (SSD alone) in the high energy condition. The identified particles are ^{6}He^{2+}, ^{3}H^{1+}, and a small number of ^{7}Li^{2+}, all of which had energies and relative time-of-flights (ToF) consistent with calculation [1].

After the optimization at F2 to maximize the ^{6}He beam intensity, the beam was transported to F3 with a transmission efficiency of 28%. ^{7}Li^{2+} disappeared from the PI diagram, while ^{3}H^{1+} remained due to its charge-to-mass ratio identical to ^{6}He. Table 1 summarizes the purities of secondary beam particles in each condition. The purity of ^{3}H^{1+} appeared to be higher at F3 compared to F2, how-

[1]The SSD at F2 was deteriorated and our measurement result indicates its partial depletion within the thickness of 750 μm, in spite of its nominal thickness of 1.5 mm. The spread energy profile at F2 is mainly due to that partial depletion.

Table 1. Summary of the secondary beam purity. Note that the F2 data were taken with the PPAC trigger, and F3 were with the SSD.

Ion	High Bρ (1.227 Tm)		Low Bρ (1.032 Tm)	
	F2	F3	F2	F3
$^{6}He^{2+}$	85%	73%	60%	61%
$^{3}H^{1+}$	15%	27%	17%	23%
$^{7}Li^{2+}$	0.2%	–	22%[a]	5.9%
$^{4}He^{2+}$	–	–		9.7%

[a] Summed purity of $^{7}Li^{2+}$ and $^{4}He^{2+}$.

ever, this is supposed to be from the limited detection efficiency of the PPAC, which triggered the measurement at F2, against the light $^{3}H^{1+}$ ion. The ^{6}He energy after one PPAC (thickness equivalent to 9.5 μm Mylar) was measured as (47.80±0.44) MeV or (7.943±0.073) MeV/u, where the energy loss in the PPAC (0.29 MeV) was in a good agreement with a calculated value (0.28 MeV).

We increased the primary beam current to confirm the highest intensity ^{6}He beam we can obtain. The ^{6}He rate increased almost proportional to the primary beam current with a ratio of 370 kcps/eμA. The detection efficiency of the PPAC was 70–80% or better, when the secondary beam rate was 300–400 kcps. The intensity test was performed up to the primary beam current of 2 eμA, at which the PPAC efficiency dropped down to 42% for the secondary-beam intensity of 630 kcps, even though we applied the possible maximum voltages on the PPAC electrodes. Target gas circulation [3] was found to be effective when the primary beam current was 2 eμA, as the trigger rate of the F3 PPAC (the upstream one) increased from 630 kcps to 750 kcps, corresponding to a recovery of the secondary beam rate of 20%.

The beam production test in the low-energy condition was performed basically in the same procedure as the high-energy case. The PI diagrams are as shown in Fig. 2, and the main difference was that there are more contamination ions of $^{7}Li^{3+}$ and $^{4}He^{2+}$, even after the Wien filter operated at ±50 kV. Consequently, we had a lower ^{6}He purity of about 60%, as shown in Table 1. The ratio of ^{6}He beam rate at F3 to the primary beam current was 200 kcps/eμA, lower than that of the high-energy condition.

In conclusion, we succeeded in producing a ^{6}He RI beam at 8.0 MeV/u with an intensity of the order of 10^{5} pps, superior to the beam at RESOLUT [8], satisfying the requirement by the proposed ^{6}He+p experiment [5]. The practical beam intensity is presently limited to about 2×10^{5} pps by the low detection efficiency of the PPAC for such a light-ion beam. To make the efficiency higher, we are planning to use wire chambers (MWDC) in the main experiment. The main contamination of the beam was $^{3}H^{1+}$, which can amount up to 27% of the secondary beam. As $^{3}H^{1+}$ cannot be eliminated by the electromagnetic separator, we may use a degrader (thicker than 5-μm Mylar) at the F1 focal plane to purify the ^{6}He beam.

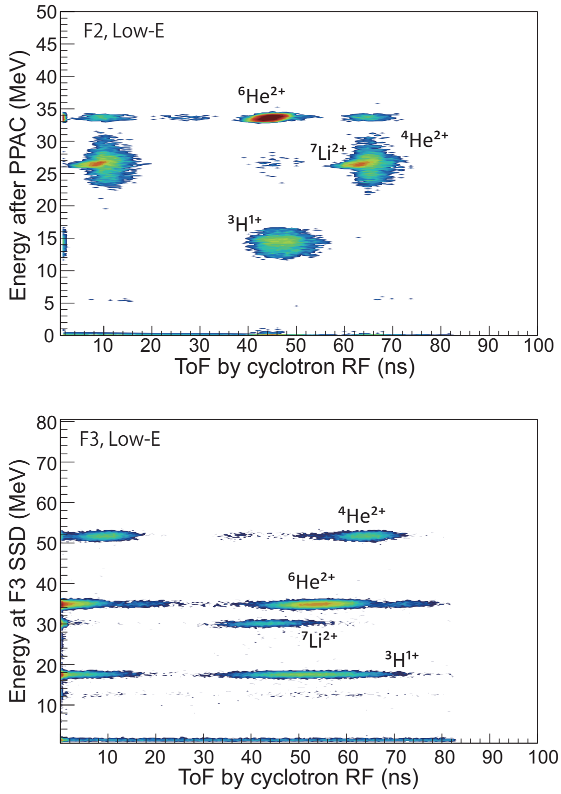

Figure 2. (Color online) PI diagrams of the secondary beams at F2 (top) and F3 (bottom), in the low-energy condition (Bρ =1.032 Tm). The locus on the right side of ^{6}He in the F2 diagram could also be ^{6}He, recorded with an illegal timing.

References

[1] S. Kubono *et al.*, Eur. Phys. J. A **13** (2002) 217.

[2] Y. Yanagisawa *et al.*, Nucl. Instrum. Methods Phys. Res., Sect. A **539** (2005) 74.

[3] H. Yamaguchi *et al.*, Nucl. Instrum. Meth. Phys. Res., Sect. A **589**, (2008) 150–156.

[4] H. Yamaguchi, D. Kahl and S. Kubono, Nuclear Physics News International **30**, No. 2, (2020) 21–27.

[5] M. Sferrazza, H. Yamaguchi et al, proposal for RIBF NP-PAC-21, NP2021-AVF70 (2020, unpublished).

[6] A. Di Pietro, et al., Phys. Rev. C **69** (2004) 044613.

[7] J.J. Kolata, Phys. Rev. C **75**, (2016) 031302(R).

[8] Web page of RESOLUT: https://fsunuc.physics.fsu.edu/research/experimental_devices/#resolut

Excitation function of α clustering study in ^{14}O

N. R. Ma[a,b], M. Sferrazza[c], H. Yamaguchi[b], T. Kawabata[d], S. Okamoto[e], S. Hayakawa[b], H. Shimizu[b], P. Descouvemont[c], S. Cherubini[f], M. La Cognata[f], T. Doi[e], Y. Fujikawa[e], K. Inaba[e], N. Itagaki[g], A. Kohda[b], G. Manicòò[f], S. Palmerini[h], R. G. Pizzone[f], A. Sakaue[e] and K. Sakanashi[d]

[a] *Center for Nuclear Study, Graduate School of Science, University of Tokyo*
[b] *Department of Nuclear Physics, China Institute of Atomic Energy*
[c] *Department of Physics, Universitéé Libre de Brussels, Belgium*
[d] *Department of Physics, Osaka University*
[e] *Department of Physics, Kyoto University*
[f] *INFN-LNS and dipartimento di Fisica e Astronomia "E. Majorana", University of Catania, Italy*
[g] *YITP, Kyoto, Japan*
[h] *INFN sez. di Perugia and dept. di Fisica e Geologia, University of Perugia, Italy*

α clustering is a well-known effect in light nuclei, and the linear-chain cluster state (LCCS) is an interesting topic in nuclear physics. The study of this novel cluster structure can provide us understanding the nature of the exotic nuclear formation. α clustering are often observed in nuclei close to the valley of stability, while the study of LCCS has focused on neutron-rich nuclei, since the valence neutrons play a glue-like role to stabilize extreme shapes. This role is well known as the molecular orbits, and they are classified into two types: the π orbit which is perpendicular to the z axis of the 2α core, and the σ orbit which is parallel to the z axis [1].

The resonances observed by the α+^{10}Be elastic scattering [2,3] exhibit level energy spacings and J^{π} that perfectly agree with the prediction of LCCS π-bond nuclear-cluster band, therefore, LCCS is likely to exist in ^{14}C. Also with the TTIK method, we measured the mirror symmetric α+^{10}C resonant scattering with a radioactive ^{10}C beam to study the α clustering near the proton drip line. By the study of α clustering in mirror nuclei we want to address the important issue in cluster physics: how strong the charge symmetry breaking in cluster states is.

Initial data analysis has provided the yield of resonant scattering α at different energies [4]. Then the detection solid angles at different center-of-mass energy E_{cm} and at different scattering angle θ_α were calculated by means of Monte Carlo simulation. The solid angle simulation was performed based on the real incident ^{10}C particle trajectories, the energy threshold for every silicon telescope was set as 4.5 MeV. There were totally 3 telescopes installed, separately at 0°, +13° and −15° with respect to the beam axis. As shown in Fig.1, the telescope 1 at 0° has a high detection efficiency at the most forward laboratory angle, corresponding to the center-of-mass angle $\theta_{c.m.}$=180° and forward kinematic laboratory angle θ_α=180°, and it can provide us with the clearest identification of ^{10}C+α resonances. While the two supplemental telescopes at +13° and −15° can effectively cover the large scattering angle α particles.

Using the yield of scattered α, the number of the incident ^{10}C particles, the effective target thickness, and the detection solid angle, the resonant scattering differential cross

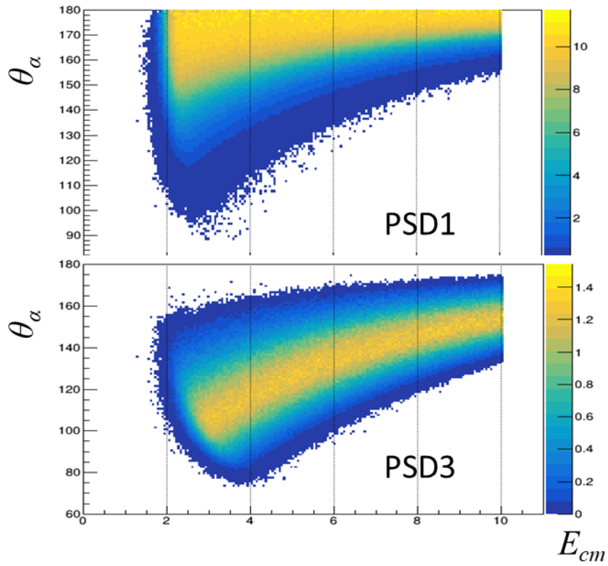

Figure 1. Calculated solid angle versus E_{cm} and θ_α.

section $(d\sigma/d\Omega)_{c.m.}$ was calculated. The obtained resonant scattering differential cross section versus E_{cm} and θ_α is shown in Fig.2 (a). By an R-matrix analysis [5] with SAMMY8 [6], we obtained the main resonance energies and estimated the spins for the dominant resonances. The resonant scattering excitation function for $\theta_\alpha = 164° - 180°$ and the preliminary R-matrix fitting results are shown in Fig.2 (b).

The best parameters at present obtained from the R-matrix calculation with SAMMY8 [6] are summarized in Table.1. Around the excitation energy of 13.5 MeV, a 0^+ resonance was observed clearly, just as predicted, the ^{10}C+α (0^+) state is broad. Around 14.28 MeV and 17.97 MeV we observed two 4^+ resonances which diminish quickly as θ_α decreased. At the large scattering angle region detected by telescope 2 and 3 such resonances nearly vanished. The resonance peak at 17.97 MeV is asymmetric and relatively broad. Based on the study of ^{10}Be+α [3], we fitted this peak as a doublet of 5^- and 4^+.

We had difficulties in confirming all resonance parameters. Between 15.0 MeV and 17.0 MeV, at least four resonant peaks were needed to reproduce the excitation func-

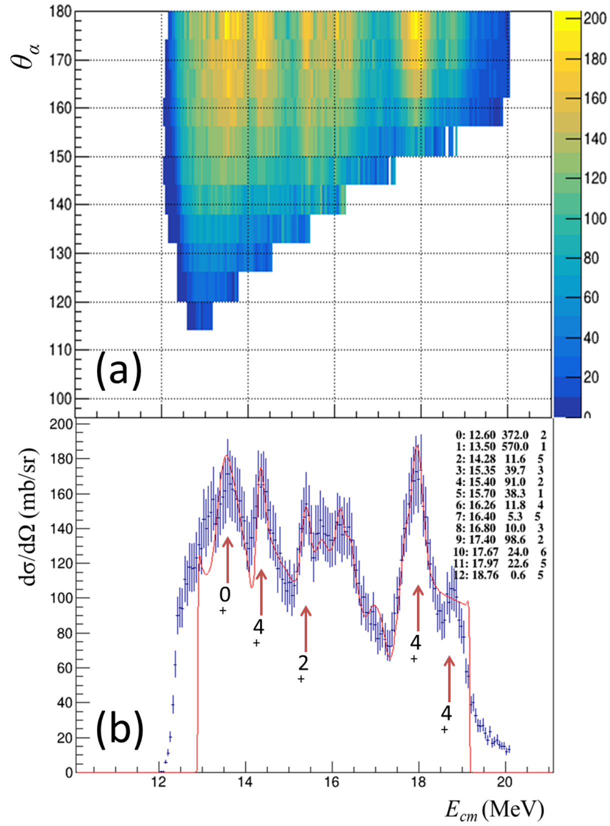

Figure 2. a) Measured resonant scattering differential cross section versus E_{cm} and θ_α. b) Measured resonant scattering excitation function for $\theta_\alpha = 164° - 180°$ and the preliminary R-matrix fitting results with SAMMY8 [6].

tion, which are close to each other and may cause a large error in our R-matrix calculation results. The rightmost resonance peak around 18.8 MeV is located on the high energy tail of the lower energy resonances. The analysis with SAMMY8 also failed to fit this peak as a distinct resonance. Since the resonance energy is close to the upper limit of the detection system, and a sharp decrease is seen on the right side of this peak, we consider that the 4^+ resonance around 18.8 MeV was only partially detected in the experiment, which resulted in a resonance peak much smaller than what it should be.

A further analysis would be necessary for confirming the resonance parameters. We are also planning to check the fitting results of SAMMY8 [6] with another R-matrix calculation code AZURE2 [7] to confirm the consistency of the two calculation codes.

References

[1] T. Baba and M. Kimura, Phys. Rev. C, **99** 021303(R) (2019).

[2] A. Fritsch, S. Beceiro-Novo, D. Suzuki *et al.*, Phys. Rev. C, **93**, 014321 (2016).

[3] H. Yamaguchi, D. Kahl, S. Hayakawa *et al.*, Phys. Lett. B, **766** (2017) 11.

[4] N.R. Ma, M. Sferrazza, T. Kawabata *et al.*, CNS Annual Report 2019, CNS-REP-19, —— (2021).

Table 1. The preliminary resonance parameters in ^{14}O determined by R-matrix fitting.

J^π	E_{cm} MeV	E_x MeV	$\Gamma_{\alpha 0}$ MeV	$\theta^2_{\alpha 0}$ %
1^-	2.48	12.6	0.372	78.7
0^+	3.38	13.5	0.57	36.0
4^+	4.16	14.28	0.0116	6.92
2^+	5.23	15.35	0.0397	1.89
1^-	5.28	15.4	0.091	3.26
0^+	5.58	15.7	0.0383	1.15
3^-	6.14	16.26	0.0118	0.63
4^+	6.28	16.4	0.0053	0.53
0^+	6.79	16.91	0.0041	0.10
1^-	7.12	17.24	0.0271	0.69
5^-	7.55	17.67	0.0235	3.15
4^+	7.85	17.97	0.0232	1.23
4^+	8.64	18.76	0.0006	0.03

[5] P. Descouvemont and D. Baye, Rep. Prog. Phys. **73** (2010) 036301.

[6] N. Larson, ORNL/TM-9179/R5, 2000, unpublished.

[7] R.E. Azuma, E. Uberseder, E.C. Simpson *et al.*, Phys. Rev. C 81 (2010) 045805.

Insight into the reaction dynamics of proton drip-line nuclear system ^{17}F+^{58}Ni at near-barrier energies

L. Yang[a], C. J. Lin[a, p], H. Yamaguch[b, c], Jin Lei[d], P. W. Wen[a], M. Mazzocco[e, f], N. R. Ma[a], L. J. Sun[a], D. X. Wang[a], G. X. Zhang[g], K. Abe[b], S. M. Cha[h], K. Y. Chae[h], A. Diaz-Torres[i], J. L. Ferreira[j], S. Hayakawa[b], H. M. Jia[a], D. Kahl[a], A. Kim[k], M. S. Kwag[h], M. La Commara[l], R. Navarro Pérez[m], C. Parascandolo[n], D. Pierroutsakou[n], J. Rangel[j], Y. Sakaguchi[b], C. Signorini[e, f], E. Strano[e, f], X. X. Xu[a], F. Yang[a], Y. Y. Yang[o], G. L. Zhang[g], F. P. Zhong[a, p], and J. Lubian[j]

[a] *Department of Nuclear Physics, China Institute of Atomic Energy*
[b] *Center for Nuclear Study, University of Tokyo*
[c] *National Astronomical Observatory of Japan*
[d] *Institute of Nuclear and Particle Physics, and Department of Physics and Astronomy, Ohio University*
[e] *Dipartimento di Fisica, Universita di Padova*
[f] *Istituto Nazionale di Fisica Nucleare-Sezione di Padova*
[g] *School of Physics, Beihang University*
[h] *Department of Physics, Sungkyunkwan University*
[i] *Department of Physics, University of Surrey*
[j] *Instituto de Física, Universidade Federal Fluminense*
[k] *Department of Science Education, Ewha Womans University*
[l] *Department of Pharmacy, University Federico II*
[m] *Department of Physics, San Diego State University*
[n] *Istituto Nazionale di Fisica Nucleare-Sezione di Napoli*
[o] *Institute of Modern Physics, Chinese Academy of Sciences*
[p] *Department of Physics, Guangxi Normal University*

Nowadays, the availability of high-quality radioactive beams greatly increases our ability to study the reactions induced by exotic nuclei [1, 2]. In contrast to the neutron-halo projectiles, reactions induced by the weakly bound proton-rich nuclei, especially by the ones with proton-halo or valence-proton structures, present distinctive properties. Both the core and valence proton have long-range Coulomb interaction with the targe, thus the dynamic Coulomb polarization effect is of particular importance [3]. So far, research on reactions with proton drip-line nucleus is still in its infancy, mainly concentrating on ^{8}B and ^{17}F, as reviewed in Ref. [2]. Experimental data with these projectiles are still scarce, hence the reaction mechanism is still not yet clear. Compared with ^{17}F, the structure of ^{8}B is more complicated because of the non-inert core, ^{7}Be, which is also proton-rich and weakly bound nucleus. ^{17}F can be treated properly with a two-body model as an inert ^{16}O core and a loosely bound proton, which is able to reproduce successfully the known electromagnetic properties of ^{17}F [4]. Moreover, considering that ^{17}F is relatively easy to be produced experimentally, it is a more suitable case for a thorough study on the reaction mechanisms of weakly bound proton-rich systems as a breakthrough point.

In this report, we present the results of the complete kinematics measurements to investigate the reaction mechanisms of ^{17}F interacting with ^{58}Ni at energies around the Coulomb barrier. The experiment was performed at CRIB (Center for Nuclear Study Radioactive Ion Beam separator) [5]. A cryogenic deuterium gas target was used as the primary target. After purification by the double achromatic system and the following Wien filter of CRIB, the ^{17}F beam was sent onto a 1.0 mg/cm^{2}-thick self-supporting and isotopically enriched ^{58}Ni target, with a typical intensity of 6--10×10^{5} particle per second and a purity of $\sim 85\%$. By adjusting the pressure of the primary gas target and inserting aluminium degraders with different thicknesses, ^{17}F with four distinct energies, i.e., 43.6 ± 0.7, 47.5 ± 0.7, 55.7 ± 0.8 and 63.1 ± 0.9 MeV in the middle of the target, were produced. A Multi-layer Ionization-chamber Telescope Array (MITA) [6] was used to detect the reaction products over a large range of Z. Angular distributions of elastic scattering, exclusive and inclusive breakup, as well as the total fusion (TF) cross sections were derived simultaneously for the first time.

The excitation functions of the total reaction (σ_{R}), inclusive ($\sigma_{\mathrm{Inc.}^{16}\mathrm{O}}$) and exclusive ($\sigma_{\mathrm{Exc.}^{16}\mathrm{O}}$) ^{16}O, as well as the TF from evaporation protons are shown in Fig. 1. One can see that, fusion reaction dominates in the above-barrier region, and it reduces exponentially as the energy decreases. The $\sigma_{\mathrm{Inc.}^{16}\mathrm{O}}$ and $\sigma_{\mathrm{Exc.}^{16}\mathrm{O}}$, however, vary smoothly with the energy, and the $\sigma_{\mathrm{Inc.}^{16}\mathrm{O}}$ becomes the major component in the sub-barrier region. The comparisons of the reduced σ_{R} and σ_{TF} between ^{17}F and ^{16,17}O with a ^{58}Ni target [7–9] are shown in Figs. 2 (a) and (b), respectively. For the σ_{R}, the excitation function of ^{17}F is nearly superimposed to the curve for the ^{16,17}O systems in the above barrier region, while the

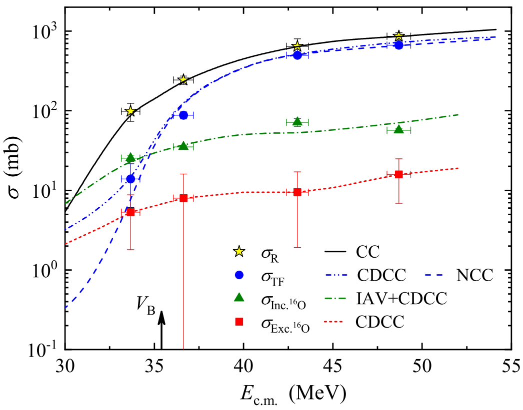

Figure 1. Excitation functions of total reaction (stars), exclusive (squares) and inclusive (triangles) breakups, and the TF (circles). The curves denote the corresponding theoretical results: the solid line denotes the coupled channel (CC) result, the dot-dot-dashed and dotted curves are the CDCC results for TF and elastic breakup, the dashed line shows the CDCC calculations switching off the couplings from the continuum states (NCC), and the dot-dashed line is the result of the IAV model plus CDCC. The arrow indicates the nominal position of the Coulomb barrier.

values at sub-barrier energies suggest a clear enhancement of the σ_R for ^{17}F+^{58}Ni. A similar behavior is also observed in the fusion reactions as shown in Fig. 2 (b), where the σ_{TF} and the $E_{\rm c.m.}$ are reduced as: $F(x)$=$2E_{\rm c.m.}\sigma_{TF}/\hbar\omega R_B^2$ and x=$(E_{\rm c.m.}-V_B)\hbar\omega$ [10]. R_B, V_B and $\hbar\omega$ are respectively the parameters associated with the barrier radius, height and curvature. The benchmark curve of the Universal Fusion Function (UFF) is also shown in Fig. 2 (b) by the solid line. It can be seen that the TF cross section of ^{17}F is in good agreement with the ^{16}O projectile at above barrier energies, while in the sub-barrier region, fusion with ^{17}F is enhanced relative to the ^{16}O system and the UFF. According to the CDCC calculations with and without the couplings to the continuum states (dot-dot-dashed and dashed curves in Fig. 1), the enhancement of TF at the sub-barrier energy is mainly due to the breakup couplings, which becomes more significant as the energy decreases. To further confirm this coupling effect, we plan to perform a complete kinematics measurement of ^{17}F+^{58}Ni at a lower energy in the sub-barrier region.

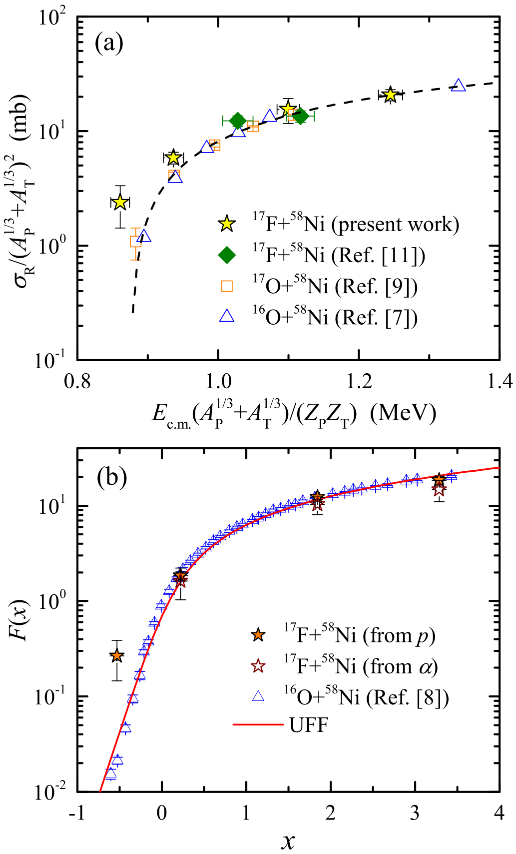

Figure 2. (Color online) Comparison of the reduced σ_R (a) and σ_{TF} (b) between ^{17}F+^{58}Ni and its neighbor systems. The dashed curve in (a) denotes the trend of the excitation functions of ^{16,17}O+^{58}Ni. The solid curve in (b) represents the benchmark UFF.

References

[1] L. F. Canto, P. R. S. Gomes, R. Donangelo *et al.*: Phys. Rep. **596** (2015) 1.

[2] J. J. Kolata, V. Guimarães, and E. F. Aguilera: Eur. Phys. J. A **52** (2016) 123 .

[3] M. Ito, K. Yabana, T. Nakatsukasa: M. Ueda, Nucl. Phys. A **787** (2007) 267c.

[4] C. A. Bertulani, P. Danielewicz, Nucl. Phys. A **717** (2003) 199.

[5] Y. Yanagisawa, S. Kubono, T. Teranishi *et al.*: Nucl. Instrum. Methods A **539** (2005) 74.

[6] N. R. Ma, L. Yang, C. J. Lin *et al.*: Eur. Phys. J. A **55** (2019) 87.

[7] N. Keeley, J. A. Christley, N. M. Clarke *et al.*, Nucl. Phys. A **582** (1995) 314.

[8] N. Keeley, J. S. Lilley, J. X. Wei *et al.*, Nucl. Phys. A **628** (1998) 1.

[9] E. Strano, D. Torresi, M. Mazzocco, N. Keeley, A. Boiano, C. Boiano *et al.*, Phys. Rev. C **94** (2016) 024622.

[10] L. F. Canto *et al.*, J. Phys. G **36** (2009) 015109.

[11] M. Mazzocco, C. Signorini, D. Pierroutsakou, T. Glodariu, A. Boiano, C. Boiano *et al.*, Phys. Rev. C **82** (2010) 054604.

Development of the analysis method to extract the CP violating sources from the EDM of ^{210}Fr

Y. Sakemi, B.P. Das[a], N. Shitara[a] B.K. Sahoo[b], S. Prasanna[b], H. Nagahama, K. Nakamura, N. Ozawa, S. Nagase, M. Sato[c], T. Nakashita[c], K. Yamane[c], T. Hayamizu[d]

Center for Nuclear Study, Graduate School of Science, The University of Tokyo
[a]International Education and Research Center of Science and Department of Physics, Tokyo Institute of Technology
[b]Atomic, Molecular and Optical Physics Division, Physical Research Laboratory
[c]Institute of Physics, Graduate School of Arts and Sciences, The University of Tokyo
[d]RIKEN Nishina Center

The development of an optical lattice interferometer to search for a permanent electric dipole moment (EDM) with Francium (Fr) atoms is now in progress at RIKEN [1]. The lattice-like potential with a standing wave of laser light, which is called an optical lattice (OL), can realize the long interaction time of the trapped Fr with external fields, so that we can get a high measurement sensitivity. The newly developed surface ionizer can produce the stable Fr with about 10^6 Fr^+/s using the nuclear fusion reaction, which can be increased with the improvement of the primary beam intensity. We are now moving to the experimental phase to trap the Fr in the MOT and OL to realize the high intensity cold Fr sources with 10^7 atoms to measure the EDM.

Currently, the most promising systems for determining the upper bounds on the magnitude of the electron EDM (eEDM) are heavy open-shell atoms and polar molecules, since the enhancement of the eEDM for these quantum many body systems are quite high. The best experimental limit using atoms comes from ^{205}Tl at $|d_e| < 1.6 \times 10^{-27}$ e cm with 90 % confidence [2]. The best limit of the eEDM to date was set by experiments on thorium oxide (ThO) at $|d_e| < 1.1 \times 10^{-29}$ e cm with 90 % confidence [3]. It should be noted that the atoms and molecules have many contributions of the CP violating sources. At leading order, such effects may be quantified in terms of EDMs of the constituent nucleons, d_n and d_p, where the neutron EDM is already an observable, the EDM of the electron d_e, and CP-odd electron- nucleon and nucleon-nucleon interactions. In the relevant channels these latter interactions are dominated by pion exchange, and thus we must also consider the CP-odd pion-nucleon couplings $g_{\pi NN}$ which can be induced by CP-odd interactions between quarks and gluons. Among them, the two dominant sources of the CP violation are the eEDM and the scalar-pseudoscalar electron-nucleus interaction in the open-shell atoms such as the Fr.

In the atomic systems, the presence of an eEDM can induce an atomic EDM (D_a) which can be many times larger than the magnitude of the eEDM. To obtain an upper limit for the eEDM, the enhancement factor $R \equiv D_a/d_e$, defined as the ratio of the atomic EDM to the eEDM, must be evaluated. Paramagnetic systems such as Fr are also sensitive to CP violation due to the scalar-pseudoscalar (S-PS) interaction between the electrons and the nucleons (e-N), which arises from the exchanges of CP violating beyond Standard Model (SM) particle between the electron and quarks or gluons in the elementary process. This leads to a finite value of the e-N S-PS coupling coefficient (C^{S-PS}) which can be appeared in certain extensions of the SM and may be probed with the measurement of atomic EDMs. Analogous to R for the eEDM, we define S which shows the enhancement of the CP violating S-PS e-N interaction. The S-PS e-N interaction Hamiltonian in atomic systems scales as Z^3, where Z is the atomic number. Thus Fr being the heaviest alkali atom, is well suited to prove insights into the S-PS e-N interaction. The factors of R and S depend on the atomic and nucleus structures, and it is important to evaluate the R and S precisely to identify each contributions from the eEDM and the S-PS e-N interaction by the correlation patterns from the EDM data for many kinds of atoms and molecules. In this report, the R and S are evaluated with the relativistic coupled cluster model, and the analysis method to decompose these contributions are shown.

The Hamiltonians describing the eEDM and S-PS e-N interactions in atomic systems are given by

$$\begin{aligned} H^{eEDM} &= -d_e \beta \vec{\Sigma} \cdot \vec{\varepsilon} \\ H^{S-PS} &= i \frac{G_F}{\sqrt{2}} C^{S-PS} A \beta \gamma_5 \rho(r). \end{aligned} \tag{1}$$

The $\vec{\varepsilon}$ is the electric field felt by the electron in an atom, $\vec{\Sigma}$ is the four component spinor with Pauli matrix, A is the atomic mass number, $\rho(r)$ is the nuclear density, where we have assumed a Fermi charge distribution. An atomic state defined as $|\Psi_v^{(0)}\rangle$, in the absence of any external interaction, is an eigenstate of the atomic Hamiltonian ($\hat{H}^0$), and can be written as

$$\hat{H}_0 |\Psi_v^{(0)}\rangle = E_v^{(0)} |\Psi_v^{(0)}\rangle. \tag{2}$$

Here, $E_v^{(0)}$ means the corresponding energy. We consider first the Dirac-Coulomb (DC) interactions in $\hat{H}_0$ then add Breit and QED interactions systematically to study the importance of the higher-order relativistic effects. If H^{eEDM} or H^{S-PS} is considered as the first-order perturbation, the new atomic state wave function $|\Psi_v\rangle$ can be written as

$$|\Psi_v\rangle = |\Psi_v^{(0)}\rangle + \lambda |\Psi_v^{(1)}\rangle. \tag{3}$$

Then, the $|\Psi_v^{(1)}\rangle$ is the first-order perturbed wave function with the perturbation parameter $\lambda \equiv d_e$ (or C^{S-PS}) when the eEDM (or S-PS) interaction Hamiltonian is considered after defining the interaction Hamiltonian $H' = H^{eEDM}/d_e$ (or

$H' = H^{S-PS}/C^{S-PS}$). The perturbed wave function $|\Psi_v^{(1)}\rangle$ can be obtained by the following equation:

$$(\hat{H}_0 - E_v^{(0)})|\Psi_v^{(1)}\rangle = (E_v^{(1)} - H')|\Psi_v^{(0)}\rangle, \tag{4}$$

where $E_v^{(1)}$ is the first-order perturbed energy and is equal to zero here owing to the odd parity nature of H'. An important feature of solving for $|\Psi_v^{(1)}\rangle$ in this work is that it circumvents the problem of excluding high-lying intermediate states in the sum-over-states approach, thereby implicitly including all the intermediate states in the calculations.

The atomic EDM is given by

$$D_a = 2\lambda \frac{\langle \Psi_v^{(0)}|D_z|\Psi_v^{(1)}\rangle}{\langle \Psi_v^{(0)}|\Psi_v^{(0)}\rangle}, \tag{5}$$

where R and S are defined as

$$R = D_a/\lambda, \quad S = D_a/\lambda, \tag{6}$$

for $\lambda = d_e$ and $\lambda = C^{S-PS}$, respectively. It is worth noting that the D_a can be written as $\vec{D} = e\vec{r}$ and $\vec{D} = d_e\beta\vec{\Sigma}$ in the case of eEDM and S-PS interactions, respectively. The relativistic coupled-coupled cluster (RCC) model has been performed to determine R and S [4] to determine atomic wave functions of the Fr atoms. In the RCC theory, the unperturbed and perturbed wave functions of one valence system like Fr atom are expressed as

$$|\Psi_v^{(0)}\rangle = e^{T^{(0)}}\left\{1 + S_v^{(0)}\right\}|\Phi_v\rangle \tag{7}$$

Here $|\Psi_v^{(0)}\rangle = a_v^\dagger|\Psi_0\rangle$ is the Dirac-Hartree-Fock (DHF) wave function of the 6p closed-shell configuration, and v corresponds to the respective valence orbitals of the initial and final states. The RCC operators $T^{(0)}$ and $S^{(0)}$ excite electrons from $|\Psi_0\rangle$ and $|\Psi_v\rangle$, respectively, to the virtual space. We use several methods: DHF and RCC with a single and double excitations approximation, employing the Dirac-Coulomb (DC) Hamiltonian and single-particle orbitals generated by Gaussian-type orbitals (GTOs) [5]. We have estimated corrections from the Breit interaction, nuclear structure, and lower-order quantum electrodynamics (QED) effects due to the vacuum polarization and self-energy interactions. The obtained results of the R and S are shown in the table 1 for the DHF and RCC calculations.

	DHF	RCC
R	727.24	812.19
S	9.53	10.62

Table 1. DHF and RCC results for the enhancement factors R and S of the atomic EDM of ^{210}Fr. S values are given in units of 10^{-18}e cm.

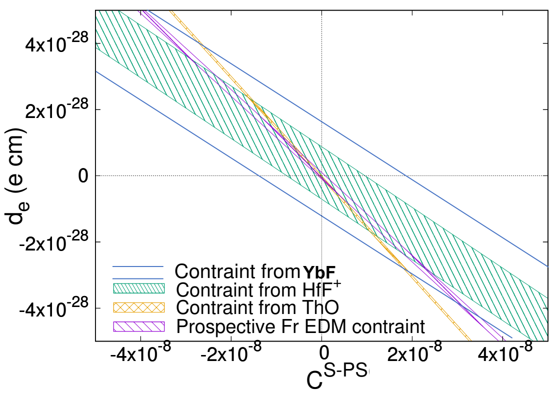

Figure 1. Correlations for the d_e and C^{S-PS} for the prospective sensitivity of the Fr EDM and existing data for the YbF, HfF$^+$, and ThO molecules.

We can see the correlation pattern of the eEDM and C^{S-PS} clearly in the Figure 1. Not only the ^{210}Fr result, but also the correlations for the other molecules and ion are shown. Since the values of the R and S depends on the atomic/molecular structure and nuclear charge density as shown above, the correlation shows the different pattern for ^{210}Fr, ThO, HfF$^+$, and YbF. It should be noted that different EDM measurements are required to pin down the CP violating sources such as eEDM and C^{S-PS}. In the next step, we are now discussing and preparing the evaluations of the R and S for the ^{221}Fr including the octupole deformation of its nucleus, and also Fr-Sr polar molecules.

References

[1] Y. Sakemi, JPS Conf. proc. **35** (2021) 011016.
[2] B.C. Regan et al., Phys. Rev. Lett. 88 (2002) 071805.
[3] ACME collaboration, Nature 562 (2018) 355.
[4] B.K. Sahoo, D.K.Nandy, B.P. Das, and Y. Sakemi, Phys.Rev. A**91** (2015) 042507.
[5] B. K. Sahoo and B. P. Das, Mol. Phys. **115** (2017) 2765.

Development of a novel detection system for francium ions extracted from the on–line surface ionizer

N. Ozawa, H. Nagahama[a], T. Hayamizu[b], K. Nakamura[a], M. Sato[b,c], S. Nagase, Y. Kotaka[a], K. Kamakura[a], K. S. Tanaka[d], M. Otsuka[b], T. Aoki[b,c], Y. Ichikawa[e], A. Takamine[b], H. Haba[b], H. Ueno[b] and Y. Sakemi[a]

Graduate School of Science, University of Tokyo
[a]Center for Nuclear Study, University of Tokyo
[b]RIKEN (The Institute of Physical and Chemical Research)
[c]Graduate School of Arts and Sciences, University of Tokyo
[d]Paul Scherrer Institute
[e]Department of Physics, Kyushu University

Cosmological observations indicate that the abundance of antimatter in our Universe is smaller than that of matter by orders of magnitude, although it is thought that matter and antimatter have been produced at equal rates. One of the conditions that lead to such an unbalance is the violation of CP symmetry [1], where C denotes charge conjugation and P denotes parity. Under the CPT theorem, which states that the C and P transformations combined with a time–reversal (T) transformation will leave physical laws unchanged, CP violation is equivalent to T violation. The permanent electric dipole moment (EDM) of elementary particles is a T– and P–violating observable. Therefore, a search for such an effect is equivalent to a search for a source of CP–violation, which probes the origin of the matter–antimatter asymmetry in the Universe.

The EDM of electrons (*e*EDM) is suggested to be enhanced in paramagnetic atoms with large proton numbers [2], up to approximately 800 times in the case of the heaviest alkali francium (Fr) [3]. In order to measure the *e*EDM at high precision, we are currently developing an *e*EDM measurement system using laser–cooled Fr atoms.

The scheme for the experiment is planned as follows. Since Fr does not have any stable isotope, it is produced as ions via the nuclear fusion–evaporation reaction $^{197}\mathrm{Au}\left(^{18}\mathrm{O},\, x\mathrm{n}\right)^{215-x}\mathrm{Fr}$ [4], followed by thermal diffusion and surface ionization from the solid Au target. The produced Fr ions are then neutralized by surface neutralization, and then laser cooled by a magneto–optical trap. The laser–cooled Fr atoms are then confined in an optical lattice. Finally, an atomic interferometer is formed to perform an EDM measurement. In the fiscal year 2019, a surface ionizer for Fr ion production was developed, and an experiment was conducted to produce Fr ions.

Fr ions are produced in the following manner. The primary beam is irradiated onto the Au target placed inside the surface ionizer, in which fusion reactions take place and Fr nuclei are produced. The produced Fr nuclei then thermally diffuse to the surface and are desorbed as singly–charged ions. As the rates of diffusion and desorption depend on temperature, the temperature of the Au target plays an essential role in determining the Fr ion extraction efficiency. In order to enhance Fr ion production, the Au target is heated up to approximately 1000°C by an infrared heater installed on the opposite side of the beam irradiation surface of the target.

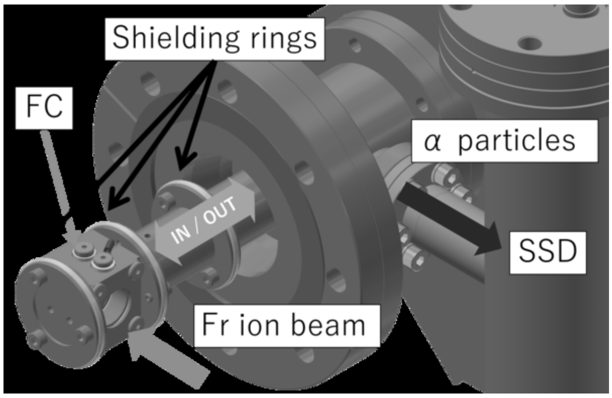

Figure 1. Developed Fr ion beam detector. Light from infrared heater is shielded by shielding rings.

The Fr ions desorbed from the Au target surface are electrostatically guided out of the surface ionizer towards the beam diagnostic system. A Si solid state detector (SSD) is used to detect the α particles emitted by the decaying Fr nuclei.

This scheme was used in the previous experiment when Fr ion production was confirmed, but we found that the infrared light from the heater induced noise in the signal from the SSD. Previously, the heater was turned off every time the SSD was operated, so that the effect on the obtained data was minimized. However, turning off the heater caused the Au target temperature to drop rapidly, which required several minutes to recover. Repeating this frequently during the experiment made the Fr production to become inefficient and time consuming.

In the fiscal year 2020, a novel beam diagnostic system was developed to overcome this problem. As shown in Fig. 1, a movable faraday cup (FC) accumulates the incoming Fr ions while reading out the beam current. The FC is then pulled in towards the SSD and the emitted α particles are detected. Four shielding rings made of PEEK (polyether ether ketone) are attached to the rod supporting the FC, which fit to the cylindrical inner wall of the stainless steel vacuum chamber. The positions of the shielding rings are calculated so that at least one ring is always in contact with the wall; therefore there is no clearance left for

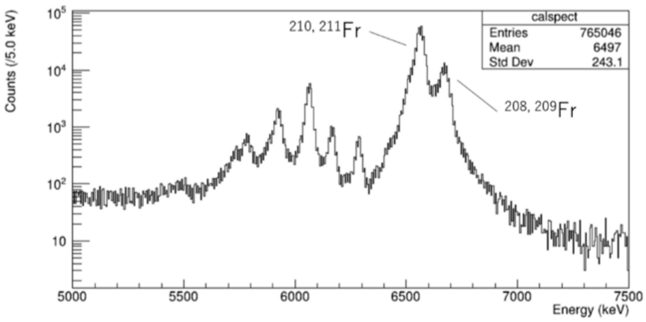

Figure 2. Typical energy spectrum of α particles emitted during decay of ions captured on FC surface, obtained using the SSD. Labelled peaks within the range of 6.5–6.8 MeV are identified as Fr.

infrared light to directly enter the SSD.

In September 2020, an experiment was conducted to produce Fr ions and evaluate the extraction rate using the newly developed beam diagnostic system. Figure 2 shows the typical energy spectrum of the α particles obtained by the SSD. Analysis of the spectrum showed that a ^{210}Fr ion beam of $\sim 5 \times 10^6$ /s, corresponding to $\sim 20\%$ extraction efficiency, was extracted. The Au target was heated up to 960°C with the help of the infrared heater. The primary beam used was an $^{18}O^{6+}$ beam of 1 particle μA accelerated to 7 MeV/nucleon using the AVF cyclotron at RIKEN.

The experiment was conducted for a duration of 12 hours. Throughout the experiment, no apparent damage to the SSD was observed, although the infrared heater was kept on. Therefore, the newly developed Fr ion beam diagnostic system enables beam diagnosis and Fr production evaluation without stopping the infrared heater, which is advantageous for stable and efficient production of Fr ions. Following this established Fr ion beam production scheme, we are continuing our development of the neutralizer and magneto–optical trap for the production of laser–cooled Fr atoms, aiming for a high–precision EDM measurement.

Acknowledgement

This work has been supported by JSR Fellowship, University of Tokyo.

References

[1] A.D. Sakharov, Sov. Phys. Usp. **34** (1991) 392.
[2] M. Popeslov *et al.*, Ann. Phys. **318** (2005) 119.
[3] N. Shitara *et al.*, J. High Energ. Phys. **2021** (2021) 124.
[4] G. Stancari *et al.*, Nucl. Instrum. Meth. A **557** (2006) 390.

Experimental Nuclear Physics: PHENIX Experiment at BNL-RHIC and ALICE Experiment at CERN-LHC

Highlights of the ALICE LS2 upgrade activities in 2020

T. Gunji

Center for Nuclear Study, Graduate School of Science, The University of Tokyo, Japan

1. Introduction

ALICE is one of the experiments at the Large Hadron Collider (LHC) in CERN [1]. The mission of ALICE is to study the strongly interacting matter composed of deconfined quarks and gluons, called quark-gluon plasma, at extreme energy densities. The ALICE detector is optimized to the heavy-ion collisions at the ultra-relativistic energies and is designed to measure as many observables as possible for a wide coverage of transverse momentum and pseudorapidity [1]. The ALICE detector consists of central barrel and a forward muon spectrometer. Central barrel is composed of silicon detectors (ITS), time projection chamber (TPC), transition radiation detector (TRD), and time-of-flight detector (TOF). A forward muon spectrometer consists of a front absorber, five tracking stations (MCH) and muon triggering chambers (MID).

The author has been an ALICE Run Coordinator since 2019 and is fully responsible to progress the ALICE commissioning during the 2nd Long Shutdown (LS2, 2019-2021). This paper describes the main progress being made during 2020.

2. ALICE upgrade in LS2

After the second Long Shutdown (LS2, 2019-2021), the LHC will deliver Pb beams colliding at an interaction rate of about 50 kHz. To fully exploit the LHC potential in Runs 3 and 4 (2021-2029), ALICE will record all minimum bias events delivered by the LHC. ALICE aims at integrating a luminosity of 13 nb^{-1} Pb–Pb collisions, which corresponds to a minimum bias data sample larger by $\times$50-100 with respect to Run 2. In order to benefit from the increasing luminosity, ALICE is going to upgrade several detector systems during LS2.

The 6 layers of silicon detectors (ITS) will be replaced with a 7 layers of new silicon pixel detectors. This new tracker will be made up of about 25000 Monolithic Active Pixel Sensors with fast readout and with reduced material thickness down to 0.3% (inner layers) – 1% (outer layers) of the radiation length and a granularity of $28 \times 28\ \mu m^2$ [2]. The assembly of the three innermost layers forming the Inner Barrel (IB) and of the four outermost ones, forming the Outer Barrel (OB), was completed in November 2019. Staves in layers are connected to the final version of the services, including readout, power supply systems, Detector Control System (DCS) and a safety system.

After the pause due to COVID-19 lockdown the preparation activities were resumed in August, starting with the verification of the functionality of the Outer Barrel staves. Each stave was fully characterised through electrical and functional checks and fully verified. All functional parameters were optimised and noise calibration procedure was developed. The thresholds for each sensor were tuned in order to achieve the target fake hit rate value 10^{-6} hits/pixel/event.

After calibration both IB and OB underwent, the continuous cosmic rays data taking was started from August 2020. This cosmic data taking was useful to optimize clustering and tracking algorithms, verify the detector geometry description, and perform detector pre-alignment studies. Due to the very low recorded chip noise, hits coming from cosmic particles passing through the detector can be clustered together and used to reconstruct the associated tracks. Figure 1 shows the cluster correlation distribution from cosmics tracks and the event display, as an example of tracks reconstructed from 6 aligned hits. This cluster correlation distribution shows the displacement of staves in layers is the order of 100 μm.

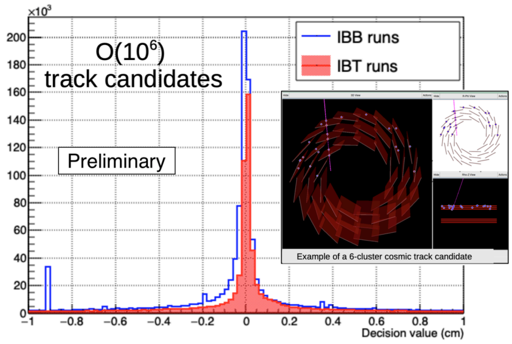

Figure 1. The cluster correlation distribution from cosmics tracks for ITS-IB layers and the event display

The second major upgrade is to replace the readout chambers of the TPC with Micro Pattern Gaseous Detectors [4]. The new readout chambers consist of stacks of 4 Gas Electron Multiplier (GEM) foils with different hole pitches. With this 4 GEM layer configuration, ion backflow can be kept less than 1%, which enables the TPC to operate continuously without a gating grid.

The TPC was moved from the cavern to the surface in March 2019. The chamber replacement, electronics installation, and tests with a laser system, cosmic rays and X-rays were carried out over a year. Various modes of data taking such as noise runs, pulser runs, laser runs, and X-ray runs, was conducted to verify the proper functioning of all chambers and electronics. Figure 2 shows the noise distribution of all pads (black) as well as for the pad regions corresponding to the four GEM stacks from inner and outer readout chambers (IROC, ORORC1, OROC2, OROC3). The pads of each stack roughly have the same pad size and the mean noise over all pads is 0.97 ADC counts, which corresponds to 670e and is within requirements.

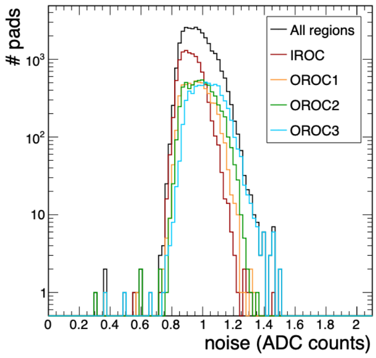

Figure 2. Noise distribution of one sector pair, separately for the IROC, OROC 1, OROC 2, and OROC 3.

Data taken with an X-ray generator are used to study the chamber stability under high load, to determine the average gas gain, and to study pad-wise gain variations. An Amptek Mini X-ray generator with Ag anode was used to irradiate the TPC. Figure 3 shows example of relative gain variations over the pad area of one full sector. Topological gain variations over the pad area are expected due to manufacturing tolerances in the hole sizes. A more robust gain calibration and equalization will be done using a ^{83}Kr source shortly before every years data taking with beams.

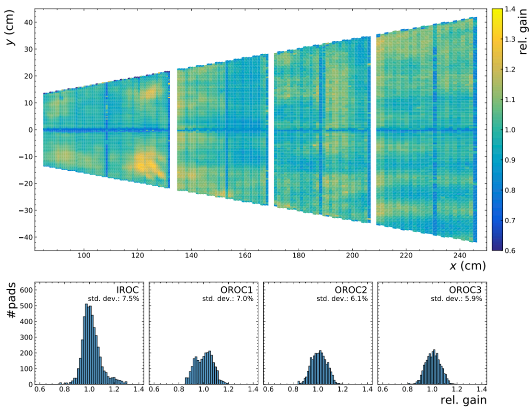

Figure 3. Top: Gain map extracted from reconstructed X-ray clusters in one sector. Bottom: gain distributions in the separate pad regions

In the beginning of August 2020, the TPC was moved from surface to the cavern and re-installed in the experimental area. After the re-installation, cabling, connection to all services (DCS, gas, cooling), and basic checks were done till the end 2020 and finally the TPC was re-commissioned in 2020.

The third major upgrade is the new readout and online DAQ system, which needs to handle 3 TB/s raw data rate [5]. The data from continuously readout detectors are reconstructed in several steps synchronously in the First Level Processors (FLP) and Event Processing Nodes (EPN). 4-8 GPUs will be housed in the EPN in order to accelerate the processing of the TPC reconstruction. ALICE has been developing a new data processing framework, called O^2. One of the milestones in the O^2 development in 2020 was to exercise the combined data taking between different detectors and validate data synchronization, event building, online processing, and reconstruction. Figure 4 shows cosmic ray event measured in the TPC and the TOF (outer of TPC). Left is $r-\phi$ view and right is $r-z$ view. Two clusters at most-outer radii are from TOF. Clear correlation of the cluster positionns between TPC and TOF is clearly visible.

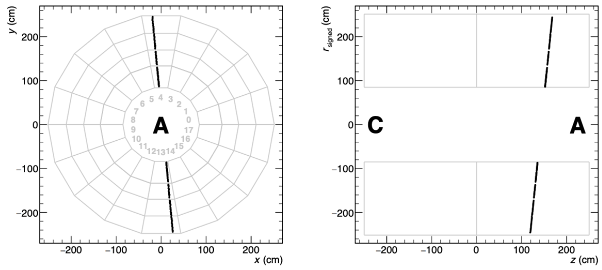

Figure 4. Combine TPC+TOF data taking and event display for cosmic tracks detected by the TOF and the TPC

3. Summary and Outlook

The surface commissioning of the new ITS and TPC was continnued in 2020. TPC was re-installed in August 2020 and the final commissioning was in progress. ITS will be installed in 2021. All detectors will be ready for global commissioning in July 2021. ALICE will start global commissioning Summer 2021 and prepare for the LHC pilot beam tests in October 2021.

References

[1] ALICE Collaboration, Int. J. Mod. Phys. A 29 (2014) 1430044

[2] ALICE Collaboration, CERN-LHCC-2012-013, CERN-LHCC-2013-024

[3] ALICE Collaboration, CERN-LHCC-2015-001

[4] ALICE Collaboration, CERN-LHCC-2013-020

[5] ALICE Collaboration, CERN-LHCC-2013-019, CERN-LHCC-2015-006

Production of low-mass dielectron in Pb–Pb collisions at $\sqrt{s_{\rm NN}}$ = 5.02 TeV with ALICE

D. Sekihata and T. Gunji

Center for Nuclear Study, Graduate School of Science, University of Tokyo

1. Introduction

The goal of performing high-energy heavy-ion collisions is to understand the properties of the quark-gluon plasma (QGP), which is a phase of matter composed of deconfined quarks and gluons under extreme conditions at high temperature and high energy density [1, 2]. Photons and dileptons are one of the tools to investigate the space-time evolution of the high-energy heavy-ion collisions. These electromagnetic probes are produced by various sources during the entire evolution and traverse the medium without strong interaction. Thus, they carry undistorted information at the time of their production [3].

Thermal Photons emitted from partonic and hadronic phases, and prompt photons produced by the initial hard scattering are called direct photons. Thermal photons carry information on the thermodynamics of the system and prompt photons are suitable for testing perturbative QCD (pQCD) calculations. Experimentally, the hadronic background is dominated and subtracted from inclusive photons by "hadronic cocktail" which simulates photons from all known hadronic decays. Photons from hadron decays are simulated based on their measured yields with detector realistic resolution. For the non-measured hadrons, their transverse momentum ($p_{\rm T}$) spectra are scaled from the measured pions called $m_{\rm T}$-scaling technique.

In particular, thermal photons are dominated in the low $p_{\rm T}$ region, typically $p_{\rm T} < 3$ GeV/c. The measurement of real direct photons at low $p_{\rm T}$ is challenging due to the large background from π^0 decays which amounts $\sim$ 85 % of total backgrounds, followed by $\eta \sim 12\%$, $\omega \sim 2\%$ and $\eta' \sim 1\%$. Alternative approach to measure the direct photons is to measure direct virtual photons via dielectron channels. One of the advantages of dielectrons compared to real photons is that the dominant background of π^0 decays is significantly reduced by measuring virtual direct photons in the dielectron invariant mass ($m_{\rm ee}$) region above π^0 mass 135 MeV/c^2. The fraction of direct virtual photons over inclusive virtual photons in the kinematic range of quasi-real photons ($p_{\rm T,ee} \gg m_{\rm ee}$) is expected to be equivalent to that of real photons in the mass-less limit $m_{\rm ee} \to 0$. Therefore, the measurement of direct virtual photons decaying into dielectron is independent and complementary to that of direct real photons [4].

2. Analysis

In November and December of 2018, ALICE took data in Pb–Pb collisions at $\sqrt{s_{\rm NN}}$ = 5.02 TeV with enhanced triggers for central semi-central collisions. As the collision rate was at 8 kHz and bunch spacing was 100 and 75 ns, there were out-of-bunch pileup collisions that distort tracking performance in Time Projection Chamber (TPC), where the drift time is 100 μs for primary electrons. As a first step, pileup events are rejected to analyze clean events without pileup collisions. Figure 1 shows the correlation between the number of TPC clusters and Inner Tracking System (ITS) which consists of 2 layers of Silicon Pixel Detector (SPD), 2 layers of Silicon Drift Detector (SDD) and 2 layers of Silicon Strip Detector (SSD). The drift time of TPC is 100 μs, while that of ITS is about 100 ns. The correlation is expected to be linear in clean events without pileup collisions. On the other hand, the long tail is found in the number of TPC clusters in pileup events. Thus, the left side of the curve is selected for further physics analyses. After applying the pileup rejection, the number of events for physics analyses is 70 M in the 0-10% and 60 M in the 30-50% centrality classes respectively.

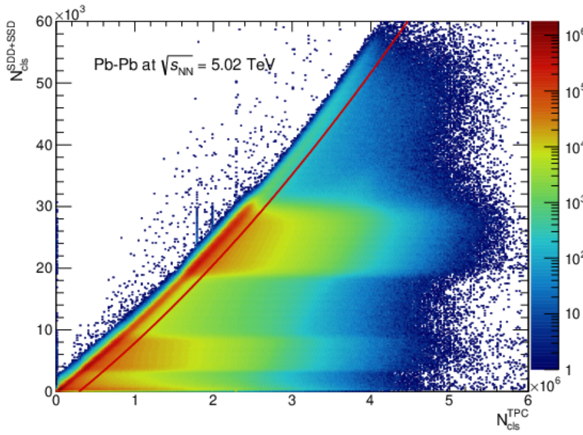

Figure 1. The correlation between the number of clusters on SDD + SSD and TPC. It is expected to be linear in clean events, namely events without pileup collisions. The curve is the criterion to select such clean events.

In this analysis, charged particles with $p_{\rm T} > 0.2$ GeV/c and pseudo-rapidity $|\eta| < 0.8$ are selected. Hits on both ITS and TPC are required to analyze charged particles from the primary vertex. Especially, a hit on the first SPD layer, which is the innermost tracker in ALICE, is required to reduce photon conversions ($\gamma \to e^+e^-$) in detector materials. The specific ionizing energy loss in unit length dE/dx measured in TPC for the electron identification described in Figure 2. To simplify the particle identification and to get relative distance from the expected value in unit of the number of σ is introduced as:

$$\mathrm{n\text{œ}_i} = \frac{\mathrm{dE/dx} - \langle \mathrm{dE/dx} \rangle_{\rm i}}{\text{œ}_{\rm dE/dx,i}},$$

where, index i is for particle species, and $\langle$dE/dx$\rangle$ is mean value and $\text{œ}_{\rm dE/dx}$ is standard deviation of the dE/dx.

The electron band within $|\text{nœ}_{\mathrm{e}}| < 3$ is selected and overlapped regions with pions and kaons, protons are rejected by $\text{nœ}_{ß} > 3.5$ and $|\text{nœ}_{\mathrm{K,p}}| > 3$ respectively. In addition to this, information on the time-of-flight with the TOF detector $|\text{nœ}_{\mathrm{e}}^{\mathrm{TOF}}| < 3$ is used to recover the rejected electrons at the crossing region with charged hadrons above.

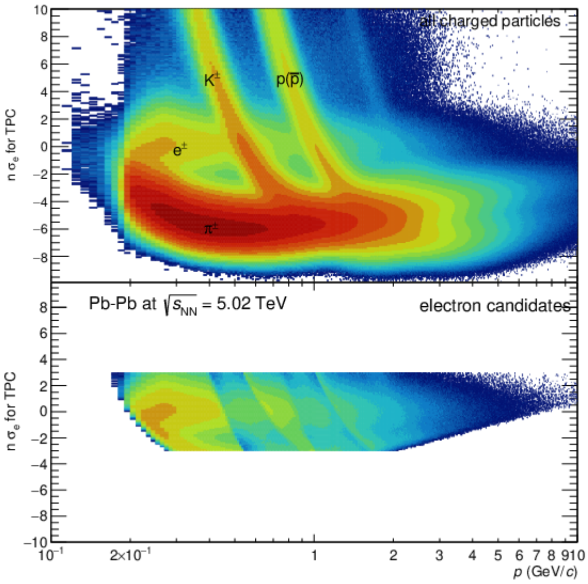

Figure 2. The number of sigmas based on ionizing energy loss in unit length measured in TPC as a function of momentum of the charged particle in minimum-bias Pb–Pb collisions at $\sqrt{s_{\mathrm{NN}}}$ = 5.02 TeV, before (top) and after (bottom) electron selection.

In the pair analysis, there are huge combinatorial backgrounds in unlike-sign pairs (ULS: e^+e^-). The combinatorial background is estimated by the like-sign technique (LS: e^+e^+ or e^-e^-). Signal S is defined as :

$$S = N_{+-} - 2R \times \sqrt{N_{++} \cdot N_{--}},$$

where R is a correction factor for different detection efficiencies between electrons and positrons obtained from the event mixing technique by:

$$R = \frac{N_{+-}^{\mathrm{mix}}}{2 \times \sqrt{N_{++}^{\mathrm{mix}} \cdot N_{--}^{\mathrm{mix}}}}$$

The reconstruction efficiency for dielectron pairs is evaluated in the Monte-Carlo simulation together with detector response. The corrected dielectron invariant mass distribution is shown in Figure 3. Data points are described within the cocktail uncertainty (gray band) originating from hadron measurements. The excess at $m_{\mathrm{ee}} < 0.5$ GeV/c^2 is interpreted as virtual photon signals to be understood in further studies.

3. Summary and outlook

The measurement of dielectron production is performed in central Pb–Pb collisions at $\sqrt{s_{\mathrm{NN}}}$ = 5.02 TeV recorded in 2018. The corrected dielectron invariant mass distribution have been extracted. Virtual photon signals are observed in the mass range of $m_{\mathrm{ee}} < 0.5$ GeV/c^2. An estimation of systematic uncertainties (e.g. tracking performance and particle identification etc.) is on-going. The direct photon excess will be extracted and compared to real direct photons at the next step. For the ultimate goal, the thermal radiation will be studied in order to understand the space-time evolution [5, 6] of high-energy heavy-ion collisions.

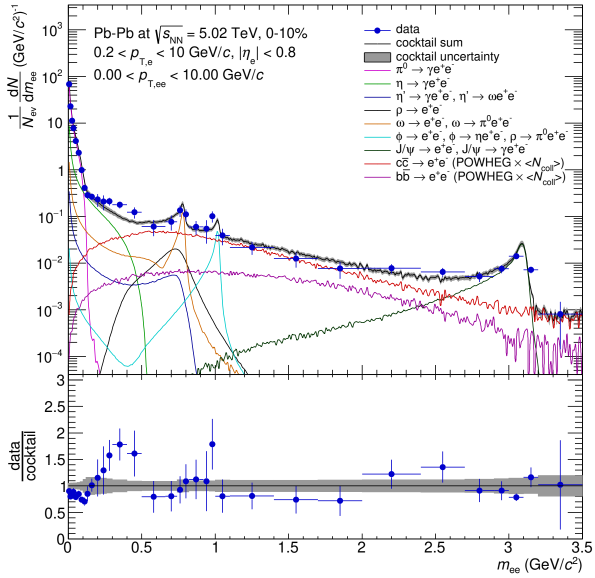

Figure 3. The corrected invariant mass distribution in central Pb–Pb collisions at $\sqrt{s_{\mathrm{NN}}}$ = 5.02 TeV. The data points are compared with known hadronic sources. The vertical bar represents the statistical uncertainty. The excess at $m_{\mathrm{ee}} < 0.5$ GeV/c^2 is interpreted as virtual photon signals.

References

[1] A. Bazavov et al., Phys. Rev. D 85, 054503 (2012)
[2] S. Borsányi et al., Phys. Lett. B 730 (2014) 99-104
[3] J. E. Alam et al., Phys. Rep. 273, 243 (1996)
[4] A. Adare et al. (PHENIX Collaboration), Phys. Rev. C 81, 034911 (2010)
[5] R.Rapp, Adv. High Energy Phys. 2013 (2013) 148253
[6] G.Vujanovic et al., Phys. Rev. C 101, 044904 (2020)

Correction to space-charge distortion with machine leaning approach for the ALICE-TPC

D. Sekihata and T. Gunji

Center for Nuclear Study, Graduate School of Science, University of Tokyo

1. Introduction

A Large Ion Collider Experiment (ALICE) [1] at the Large Hadron Collider (LHC) is an experiment dedicated to high-energy heavy-ion collisions in order to study strongly interacting matter at the highest energy density, an extreme phase of matter called quark-gluon plasma (QGP). Our early universe is thought to have been in such a state at $10^{-6} \sim 10^{-5}$ second after the Big Bang.

The Time Projection Chamber (TPC) in ALICE [2] is a gaseous tracking detector at the mid-rapidity. The reconstruction of charged particles and the particle identification are carried out. The momentum of charged particle is measured by the curvature of the trajectories in the solenoid magnet at 0.5 T. The particle identification is performed by the energy loss in the gas. An electric field of 400 V/cm is achieved in the drift volume of TPC by applying -100 kV at the central electrode. The fine-segmented field cage on the inner and outer wall allows a very high homogeneity of the electric field. The readout chamber at the end cap ($z = \pm 250$ cm) is divided into 18 sectors in azimuthal angle φ. In each sector, there are inner and outer readout chamber, called IROC and OROC, whose active area are between 85 and 132 cm for IROC, and 135 and 247 cm for OROC in radial direction. The readout chambers consist of Multi-Wire Proportional Chamber (MWPC) with gating grid in Run 1 (2009-2013) and 2 (2015-2018).

In Run 3 starting from 2021, LHC experiments will take data in Pb–Pb collisions at $\sqrt{s_{\rm NN}}$ = 5.5 TeV, which is the highest collision energy all over the world. Currently, upgrade of the TPC [3] is ongoing in order to accumulate huge statistics. The new readout chamber consists of stacks of four Gas Electron Multiplier (GEM) foils without gating grid which enables continuous data taking in Pb-Pb collisions at 50 kHz. Under the high collision rate, a lot of positive ions is produced by the amplification process on GEMs. With the gain of the GEMs of 2000 and 1% of IBF, 20 ions per a primary electron are expected to go back to the drift volume. Due to the long drifting time for positive ion 160 ms, 8000 pileup collisions are expected in this time window, meaning that the electric field inside the drift volume is distorted and needs to be corrected.

2. Strategy for calibration

The simulated space-charge density $\rho_{\rm SC}$ at 50 kHz of Pb-Pb collisions is shown in Figure 1. The resulting distortion in radial direction dr obtained by solving Poisson and Langevin equation is shown in Figure 2. It is shown that electrons deflect towards the radial center of the drift volume. The absolute value of the distortions in radial direction dr increases towards the inner and outer wall, reaching 20 cm at the inner wall close to the central electrode. The

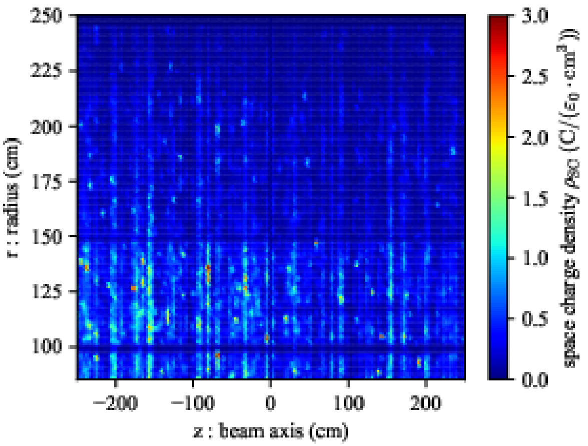

Figure 1. The simulated space-charge density $\rho_{\rm SC}$ at 50 kHz of Pb-Pb collisions in r-z plane. The striped pattern in z originating from the fluctuation of the charged-particle multiplicity corresponds to timing structure of collisions.

calibration will be performed in two steps. A first correction is applied online before tracking. The TPC clusters are corrected by a 3D correction map obtained by tracklets from the Inner Tracking System (ITS), Transition Radiation Detector (TRD) and Time-Of-Flight detector (TOF) as a reference for the true track position. The map is updated to the current average charged particles density in the time interval of $\mathscr{O}$(min) scaled by the digital currents from the readout chambers integrated over the drifting time of ions. At the second step, the space-charge density fluctuations $\mathscr{O}(mm)$ are taken into account and the intrinsic resolution of TPC $\mathscr{O}(200\mu m)$ must be restored. The correction has to be applied for every about 5 ms with scaling a high-resolution map by the integrated digital currents. The high-resolution correction map is obtained by reference tracks interpolated from ITS, TOF and TRD.

3. Machine learning approach

In this study, the goal is to correct the residual distortion fluctuation from $\mathscr{O}(mm)$ to $\mathscr{O}(200\mu m)$. Standard way is to solve Poisson equation and obtain the distorted electric field map. Then, by solving the Langevin equation, distortions of drift lines are finally obtained. Here, numerical calculations take $\mathscr{O}(0.5s)$ with 10^5 voxels. Alternative approach to speed up the computation is to use machine learning approach. In order to correct rapidly, convolutional neural network (CNN) is employed in a correction framework. UNet model [4] is used so far. It is originally developed for biomedical image segmentation. The variables for input and output are following :

$$\langle \rho_{\rm SC} \rangle, \rho_{\rm SC} - \langle \rho_{\rm SC} \rangle \leftrightarrow dr - \langle dr \rangle, rd\varphi - \langle rd\varphi \rangle, dz - \langle dz \rangle.$$

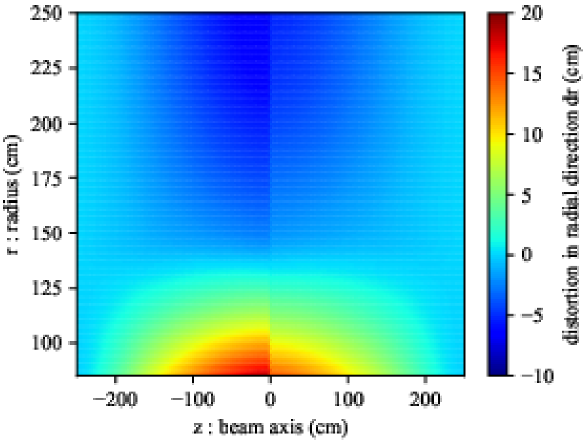

Figure 2. The expected distortion in radial direction dr at 50 kHz of Pb-Pb collisions in r-z plane.

The network is trained by the correlation between space-charge density fluctuations $\rho_{SC} - \langle\rho_{SC}\rangle$ and distortion fluctuations ($dX - \langle dX\rangle$, $X = r, r\varphi, z$). As the fluctuation strongly depends on mean value of space-change density $\langle\rho_{SC}\rangle$, it is also used as one of the training inputs here. In the simulated data, space points in the TPC volume is divided into (r, φ, z) = (33,180,33). The training is performed on a GPU server (Tesla V100 [5]) at CERN and takes about 20 minutes for 10^5 voxels. After the training, the network predicts distortion fluctuations within 10 μs from the space-charge density and its fluctuation. Figure 3 shows the root mean square error (RMSE) of the difference between predicted and numerical distortion fluctuations in radial direction as a function of the number of epochs, which indicates the training is converged well in different configurations. Figure 4 shows the mean value and RMSE in radial direction as a function of the radius in TPC for $0 < z < 5$ cm and the relative space-charge fluctuation is $5 \sim 7$ % corresponding to 1 σ. RMSE increases towards the most inner radius for all models and reaches 600 μm for the high grid granularity. These results indicate that the models for grid size 90×17 with 10k training events is trained well, but undertrained for 180×33 with 18k training events.

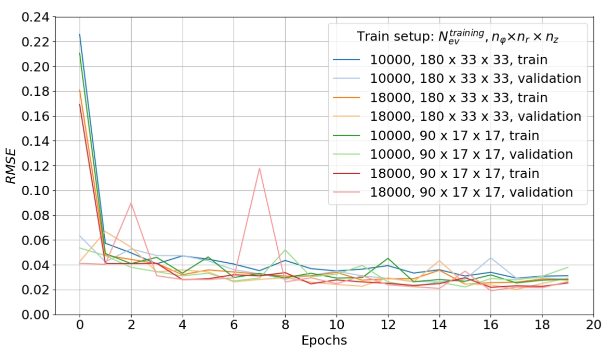

Figure 3. RMSE between predicted value and numerical calculation of distortion fluctuations as a function of the number of epochs. The training converges well.

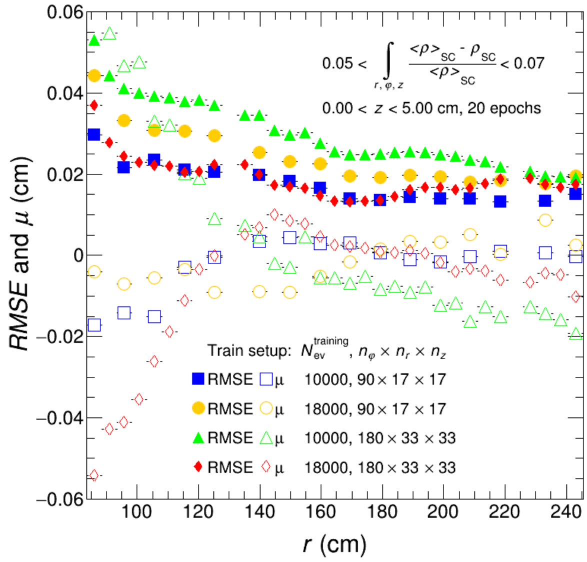

Figure 4. The mean value μ and RMSE of the difference between predicted value and numerical calculation of distortion fluctuations in radial direction.

4. Summary and outlook

ALICE will take Pb–Pb data continuously at 50 kHz with the upgraded GEM-TPC from Run 3. Under the high collision rate, huge space-charge distortions of the electric field in the TPC is expected. In order to correct the distortions, a machine-learning-based framework is being developed. At the current stage, the results do not satisfy the required resolution ±200 ¯m yet. For further study, it is suggeted to apply another correction by taking only z direction into account before the 3D correction. As the z direction in TPC is equivalent to the collision timing, the fluctuation of the space-charge density shows strong z dependence. Thus, a simplifid 1D(z) correction is expected to reduce the distortion fluctuation.

References

[1] B. Abelev et al. (The ALICE Collaboration), Int. J. Mod. Phys. A 29 (2014) 1430044

[2] The ALICE Collaboration, CERN-LHCC-2000-001

[3] The ALICE Collaboration, CERN-LHCC-2013-020

[4] Olaf Ronneberger, Philipp Fischer, Thomas Brox, arXiv:1505.04597

[5] https://www.nvidia.com/ja-jp/data-center/v100/

Long-range correlation in small collision systems with ALICE

Y. Sekiguchi for the ALICE Collaboration

Center for Nuclear Study, Graduate School of Science, the University of Tokyo

1. Introduction

The long-range correlations in the rapidity space, called "ridge", were firstly observed in Au–Au collisions at $\sqrt{s_{\mathrm{NN}}}$= 200 GeV at RHIC [1, 2]. The long-range correlations are well understood as derived from the collective expansion of the initial collision geometry and its fluctuations in heavy-ion collisions. Similar long-range correlations have been observed in high-multiplicity pp and p–Pb collisions at the LHC [3]. The measurements of a ridge structure with a large rapidity gap and its multiplicity dependence are important for quantifying the final-state interactions. We presents results on long-range two-particle correlations with a pseudorapidity gap $|\Delta\eta| \sim 8$, which is an unprecedented $\Delta\eta$ range at the LHC, and extracted the second-order azimuthal anisotropy as a function of pseudorapidity ($v_2(\blacksquare)$) at $-3.4 < \eta < 5$ in p–Pb collisions at $\sqrt{s_{\mathrm{NN}}}$=5.02 TeV.

2. Experimental setup

The main sub-detectors in this analysis are the Time Projection Chamber (TPC) and the Forward Multiplicity Detector (FMD). The TPC is used for charged particle tracking. It covers a pseudorapidity of $|\eta| < 0.8$, where a 2π coverage in azimuthal angle is ensured. The FMD is located at $-3.4< \eta < -1.7$ (FMD3) and $1.7< \eta <5.1$ (FMD1,2) with 2π acceptance in azimuthal angle. The FMD is not a tracking detector. However, it can measure the multiplicities with a granularity of $\Delta\varphi = 1/20\pi$ and $\Delta\eta = 0.05$. For event trigger and centrality determination, the V0 detectors, which are placed at $-3.7< \eta < -1.7$ (V0C) and $2.8< \eta <5.1$ (V0A), are used. Minimum-bias events are triggered by using a coincidence signal between V0A and V0C. The positive pseudorapidity is in Pb-going direction in p–Pb collisions.

3. Analysis

The two-particle correlations between trigger and associated particles are measured as a function of the pseudorapidity difference $\Delta\eta$ and the azimuthal angle difference $\Delta\varphi$ for a given event. The TPC can measure the track of charged particles one by one, however, the FMD is not a tracking detector and the multiplicities measured in each FMD segment are treated as the number of tracks in the average φ and η of each segment. The correlation function as a function of $\Delta\eta$ and $\Delta\varphi$ between two charged particles is defined as

$$\frac{1}{N_{\mathrm{trig}}}\frac{\mathrm{d}^2N_{\mathrm{asso}}}{\mathrm{d}\Delta\blacksquare\mathrm{d}\Delta'} = \frac{S(\Delta\eta,\Delta\varphi)}{B(\Delta\eta,\Delta\varphi)}, \quad (1)$$

where N_{trig} is the total number of triggered particles in the event class, the signal distribution $S(\Delta\eta,\Delta\varphi) = \frac{1}{N_{\mathrm{trig}}}\frac{\mathrm{d}^2N_{\mathrm{same}}}{\mathrm{d}\Delta\blacksquare\mathrm{d}\Delta'}$ is the associated yield per trigger particle in the same event, and the background function $B(\Delta\eta,\Delta\varphi) = \alpha\frac{\mathrm{d}^2\mathrm{N}_{\mathrm{mixed}}}{\mathrm{d}\Delta\blacksquare\mathrm{d}\Delta'}$ is the pair yield between trigger in one event and associated particles from other events in the same event class. The α factor is chosen so that $B(\Delta\eta,\Delta\varphi)$ is unity at the maximum bin. By dividing $S(\Delta\eta,\Delta\varphi)$ by $B(\Delta\eta,\Delta\varphi)$, pair acceptance and pair efficiency are corrected. Figure 1 shows the associated yield per unidentified hadron trigger particles for TPC-FMD1,2 at $2.9 < \eta <3.1$ (left) and TPC-FMD3 at $-3.1< \eta <-2.9$ (center) with $0.2< p_T^{trig} <3$ GeV and FMD1,2–FMD3 correlations between $4.6< \eta <4.8$ and $-3.1< \eta <-2.9$ (right) in 0–5 % and 60–100 %centrality classes, respectively. Centrality is a quantity that represents the center of collision and the particle multiplicity is larger in central collisions than in peripheral collisions. The long-range correlations in the near-side ($-\pi/2 < \Delta\varphi < \pi/2$), called ridge, can be observed in 0–5% events for TPC-FMD1,2, TPC-FMD3, and FMD1,2-FMD3, while it is not significant in 60–100 % events.

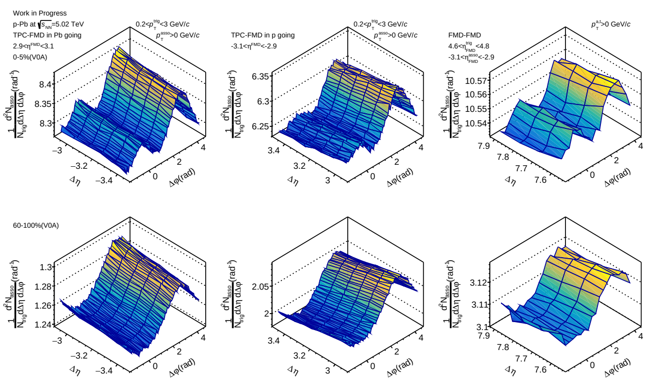

Figure 1. Correlation functions between TPC-FMD1,2 (left), TPC-FMD3 (center), and FMD1,2-FMD3 (right) in central collisions (0–5%) and in peripheral collisions (60–100%), respectively.

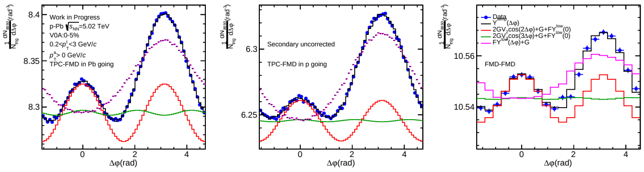

Figure 2. Projection onto $\Delta\varphi$ of correlation functions in central collisions (0–5%) between TPC-FMD1,2 (left), TPC-FMD3 (center), and FMD1,2-FMD3 (right), respectively

Figure 2 shows the projection of correlation functions to $\Delta\varphi$ in central collisions (0–5%) for TPC-FMD1.2 (left), TPC-FMD3 (center), and FMD1,2-FMD3 (right). The template fitting procedure [4] is applied to reduce the non-flow

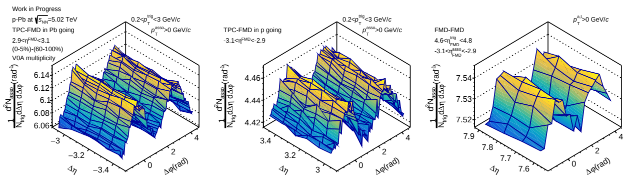

Figure 3. Correlation functions in central events after the peripheral subtraction between TPC-FMD1,2 (left), TPC-FMD3 (center), and FMD1,2-FMD3 (right), respectively

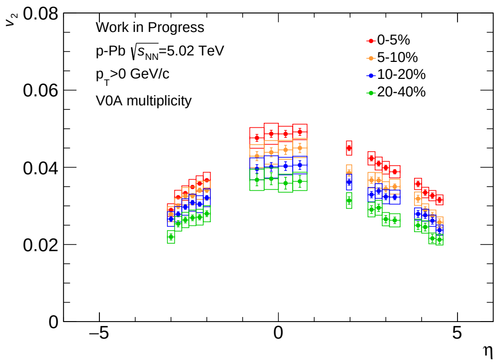

Figure 4. $v_2(\eta)$ as a function of centrality in p–Pb collisions

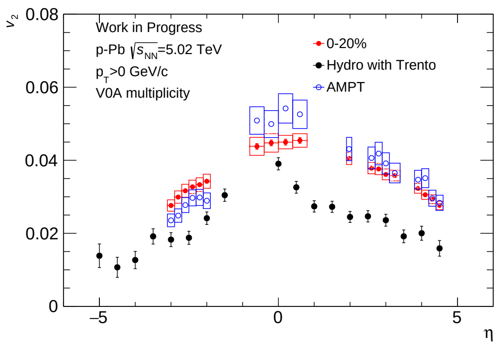

Figure 5. $v_2(\eta)$ compared to the Hydro and the AMPT calculation in 0–20 % p–Pb collisions

contamination from jets and resonance decay. The correlation function is assumed to result from a superposition of scaled correlations in peripheral events and flow components.

$$Y_{\text{cent.}}(\Delta\varphi) = FY_{\text{peri.}}(\Delta\varphi) + G\{1 + 2\sum_{n=2}^{3} V_n \cos(n\Delta\varphi)\} \quad (2)$$

$Y_{\text{cent.}}(\Delta\varphi)$ and $Y_{\text{peri.}}(\Delta\varphi)$ are the correlation functions in central and peripheral events, respectively. F, G, V_n are free parameters. Figure 3 shows correlation functions in high-multiplicity events after the peripheral subtraction ((0–5%)−(60–100%)) for TPC-FMD1,2 (left) and TPC-FMD3 (center), and FMD1,2-FMD3 (right). Long-range structure on both the near and away side is observed up to $\Delta\eta \sim 8$ in central p–Pb collisions. From the relative modulations V_n, the azimuthal anisotropy at a certain η can be obtained by using the three-sub event method. V_2 is the product of $v_2(\eta_1)$ and $v_2(\eta_2)$. The pseudorapidity dependence of v_2 is obtained as

$$v_2(\eta_{\text{FMD1,2}}) = \sqrt{\frac{V_2(\eta_{\text{TPC}}, \eta_{FMD1,2})V_2(\eta_{\text{FMD1,2}}, \eta_{\text{FMD3}})}{V_2(\eta_{\text{TPC}}, \eta_{\text{FMD3}})}}. \quad (3)$$

Since the measured p_{T} region is different between TPC and FMD, it is necessary to extrapolate v_2 of the TPC region to $p_{\text{T}} > 0$ in order to compare v_2 in the entire rapidity region. The extrapolation factor is extracted by using p_{T} spectrum and p_{T} differential v_2.

$$\alpha = \frac{\int_0 v_2 \frac{dN}{dp_T} dp_T}{\int_0 \frac{dN}{dp_T} dp_T} / \frac{\int_{0.2} v_2 \frac{dN}{dp_T} dp_T}{\int_{0.2} \frac{dN}{dp_T} dp_T} \quad (4)$$

The integrated v_2 is obtained as $v_2^{p_T>0} > \alpha v_2^{p_T>0.2}$. Figure 4 shows the extracted $v_2(\eta)$ as a function of centrality in p–Pb collisions after the p_{T} extrapolation. The v_2 is larger in the central rapidity region than in the Pb-going direction and the p-going direction. Figure 5 shows $v_2(\eta)$ in 0–20 % centrality events compared to the hydro with Trento-initial condition and A Multi-Phase Trans-port (AMPT) calculations. The hydro model calculation underestimates the data, while the AMPT describes the data qualitatively over the entire rapidity region. It indicates that the initial effect such as initial momentum anisotropy and longitudinal fluctuation plays an important role in small collision systems.

4. Summary

The long-range two-particle correlations are measured by using the TPC and the FMD in p–Pb collisions at $\sqrt{s_{NN}}$=5.02 TeV. The long-range correlations are observed up to $\Delta\eta \sim 8$ in central p–Pb collisions. The pseudorapidity dependence of v_2 is extracted by using the three-sub event method. It has centrality and pseudorapidity dependence. We also compared the data to the hydro and AMPT calculations. The AMPT describes the data qualitatively over the entire rapidity region while the Hydro calculation underestimates the data. A model is required that describes comprehensively from the initial state to the final states for further discussion.

References

[1] STAR Collaboration, Phys. Rev. C80 064912 (2009).
[2] PHOBOS Collaboration, Phys. Rev. Lett. 104 062301 (2010).
[3] CMS Collaboration, JHEP 09 091 (2010).
[4] ATLAS Collaboration, Phys. Rev. Lett. 116, 172301 (2016).

Accelerator and Instrumentation

Study of electron mobility in the mixed gas for the ionization chamber

N. Imai, Y. Nambu[a], M. Dozono, S. Michimasa, R. Tsunoda

Center for Nuclear Study, Graduate School of Science, University of Tokyo
[a]*Department of Physics, Rikkyo University*

At the coming experiments for surrogate reactions at OEDO, heavy reaction residues will be measured at the final focal plane of the OEDO/SHARAQ beam line which is placed downstream of the first dipole magnet of the SHARAQ spectrometer. The final focal plane detectors consist of two parallel plate avalanche counters (PPACs) and an ionization chamber (IC). The PPACs tell us the trajectory of the ions, while the IC measures the Bragg Curve, which allow us to identify the reaction residues.

In the Day-0 experiment of the OEDO, the IC was filled with tetrafluoromethane (CF_4) of 100 Torr. Because the beam intensity provided by OEDO is more than 10^4 cps, the fast electron mobility is required to avoid the overlapping the wave forms [1]. In general, it is well known that in the CF_4 gas the electron mobility is fast. However, the drawback is that it functions as the quencher gas, namely it reduces the number electrons produced by the ions. To improve the resolving power of the Bragg Curve, the number of electrons are as important as the electron mobility. In addition, in a reference it was reported that the higher electron mobility was obtained by mixing Ar in CF_4 [2]. The electron mobility and the amplitude by mixing Ar in CF_4 was studied.

Normally, the electron mobility is obtained as a function of the reduced electric field, which is defined as the ratio of the electric field to the pressure of gas. In the references, the data were usually taken around 760 Torr or higher. On the other hand, the pressure was as low as several 10 Torr for our experiment because of the short range of low-energy RI beams. The velocity of electron in the gas at the low-pressure needs to be measured experimentally. To measure the electron mobility in the low pressure, we made a small ionization chamber and measured the mobility by changing the pressure and the mixture rate of the gas.

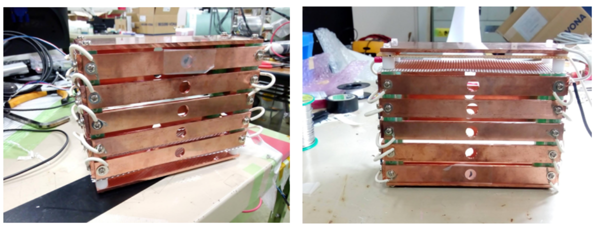

Figure 1. A photo of the proportional counter. See the text in detail.

The electron mobility is measured by the traveling time of electrons in the uniform electric field. The pairs of electron and hole are produced by the energy loss of the α particle from ^{241}Am. Because the energy loss of the α was too low to measure in the ionization counter, four wires were placed as proportional counters. The lid of the counter was

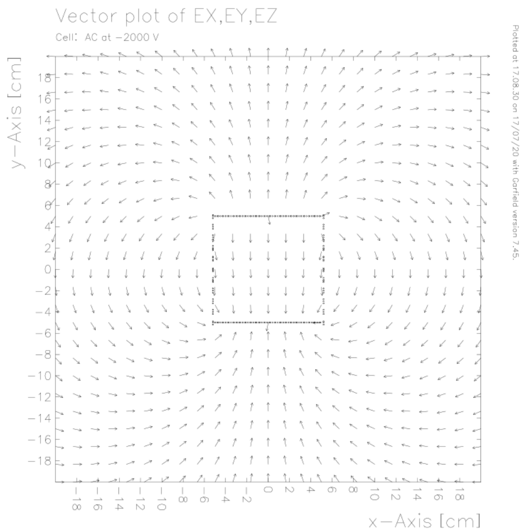

Figure 2. The distribution of the electric field simulated by Garfield. The number of side slabs and the space between them were changed to make a uniform electric field inside the proportional chamber.

a 3 mm thick copper plate of 5×15 cm^2 which was biased with around -1000 V. Each side of the counter was covered with five 0.8 cm-width copper slabs of 3 mm thickness with 0.2 cm space. A stainless mesh plate of 5 mm pitch was placed at 10 cm below the lid. The mesh was connected to the ground. The side slabs were connected via a 10 MΩ register. In total 50 MΩ were connected. The width of the side slabs were determined to make a uniform electric field inside the counter. Figure 2 shows the simulated electric field using the Garfield [3]. Below the mesh plate, four wires of Au/Cu of 50 μ diameters were placed to amplify the number of the electrons. The wires were connected together to a preamplifier biased with around 700 V. At the bottom of the counter, a 3mm thick copper plate was placed and connected to the ground. At the long-side of the slab, a hole of 1 cm diameter was made to pass the α particles through. ^{241}Am was placed around the hole at the one side of the counter, while a photodiode was located around the other side of the hole, to provide the start signals.

The proportional counter was placed in the scattering chamber. At first, the chamber was pumped down with a turbo molecular pump to 0.1 Pa for 1 hours. Then the gas of around 100 Torr was started to flow in the chamber. As the gas, CF_4 and mixture of Ar and CF_4 were used, separately. The mixture ratio of CF_4 was changed from 10% to 100%. It was found that the gas flow needed to measure the mobility. When the gas flow was stopped the mobility was observed to decrease quickly because of the out-gas from the chamber.

The circuit diagram is presented in Fig. 3. The time difference between the start and the stop signals were converted to the analog output by Time to Analog Converter and then recorded by the multi channel analyzer. To confirm the stability of the electron mobility, the measurements were repeated five times. Each measurement time was 2000 s.

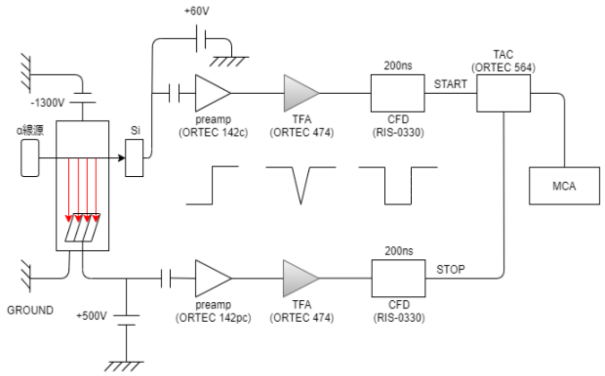

Figure 3. The circuit diagram to measure the traveling time of the electrons produced by the α particle from ^{241}Am.

The electron velocity as a function of the reduced electric field is shown in Fig. 4. The velocity with the pure CF_4 gas was around 9 cm/μs and peaked around $E/P = 0.7$ cm/μs. On the other hand, when 40 $\sim$ 50% of Ar was mixed, the velocity was observed to increase by 10%. When E/P value increases, the velocity seems increase further. However, when the reduced bias was higher than 0.8, discharge frequently happened so that the data points were not measured. On the other hand, once the CF_4 gas was introduced, the amplitude suddenly reduced and was observed to be independent of the mixture ratio.

Although the dependence of the reduced electric field in the literature are slightly different, the present result shows that the mixture of Ar can increase the velocity, which was observed to be consistent. Since the larger amplitude cannot be expected with the mixture and the velocity won't be improved so much, we will adopt the pure CF_4 gas in the OEDO experiment.

Acknowledgment

The work was partly funded by Grant-in-Aid for Scientific Research (B) 19H01903.

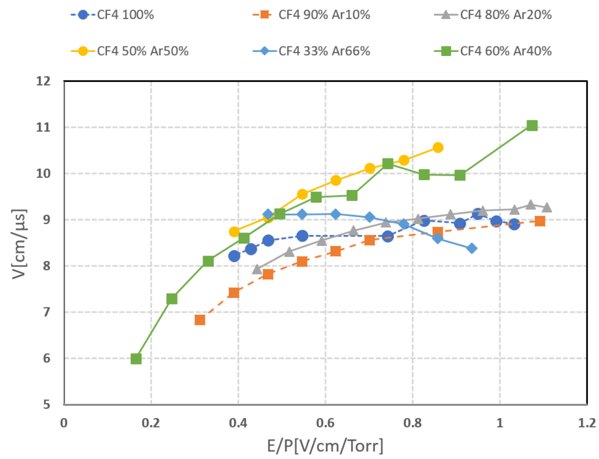

Figure 4. The electron mobility as a function of the reduced electric field.

References

[1] N. Chiga, et al., Proceedings of Symposium on Technology in Laboratories, National Institute of Fusion Science, p6, (2018).
[2] A. Peisert, and F. Sauli, CERN 84-8 (1984).
[3] https://garfield.web.cern.ch/garfield/files/ .

Safety for a Ti-^{3}H target at OEDO/SHARAQ beam line

N. Imai, K. Miki[a], S. Michimasa, K. Tanaka[b]

Center for Nuclear Study, Graduate School of Science, University of Tokyo
[a]Department of Physics, Tohoku University
[b]Safety management group, RIKEN Nishina Center

In NP1712-SHARAQ11, tri-neutron state will be studied by the charge exchange reaction, ^{3}H(^{3}H, 3n)^{3}He using the SHARAQ spectrometer. The key device of the experiment is a tritium-absorbed titanium target of 1.6 TBq which has been developed by Tohoku and Toyama Universities. This is the first experiment for SHARAQ to employ the unsealed radioactive target.

Because tritium can be easily replaced with the hydrogen, the legal regulation on the tritium is rather hard in Japan. The highest possible radioactivity at the experimental vault is 0.8 Bq/cm^3 in the form of ^{1}H^{3}HO. The residual surface activities needs to be less than 4 Bq/cm^2.

The beam line must be in vacuum for the experiment, namely the beam line will be always pumped by turbo molecular pumps (TMPs). To limit the contamination of ^{3}H to the beam line as small as possible, the vacuum of the beam line, where the target is stored, should be separated from the upstream beam-line. In the coming experiment, a thin foil will be installed downstream of FE7. Downstream beam-line including four focal plane vacuum chambers from FE8 to S2 will be pumped down only with the TMP of 1000 L/s and a fore-line rotary pump of 1500 L/s placed at S2. The valves in front of all other pumps will be closed.

The tritium gas emerged from the target was taken care at the hotlab in RIBF. The exhaust of the fore-line pump of S2 was also stored and processed at the hotlab. At the ion source of the isotope separator on-Line in Japan Atomic Energy Agency (JAEA), the exhaust of the pumps was stored in a buffer tank of 1000 L. By referring to the exhaust system of JAEA [1], a buffer tank was designed and made for the safety of the beam line at OEDO/SHARAQ.

As the first step, the out-gas rate from FE7 down to S2 was measured. The beam line from FE7 to S2 was connected and the valves of all pumps other than S2 were closed. The exhaust of the fore-line pump of S2 was connected to a $30 \times 30 \times 30$ cm^3 buffer chamber, which was in vacuum before the connection. Then, the pressure of the buffer chamber was measured for 17 hours, as shown in Fig. 1. It was found that the pressure increased gradually but that the ramping rate was not so high. The figure indicates that even the small buffer chamber can store the exhaust for several days until the pressure reaches an atomospheric pressure. At the main experiment, a larger buffer tank needs to keep exhaust for 1 month from the preparation to the end of the main experiment. A large exhaust buffer tank of 40 cm diameter and 100 cm length was made as shown in Fig. 2. The stored gas which may include tritium must be thrown away from the exhaust line of the hot-lab of RIBF, which includes the special filter. To bring the buffer chamber easily, the wheels were attached to the chamber. To monitor the pressure of the buffer tank and the beam lines, analog outputs of the vacuum gauges will be read and recorded by the raspbery-pi. The logger is under development.

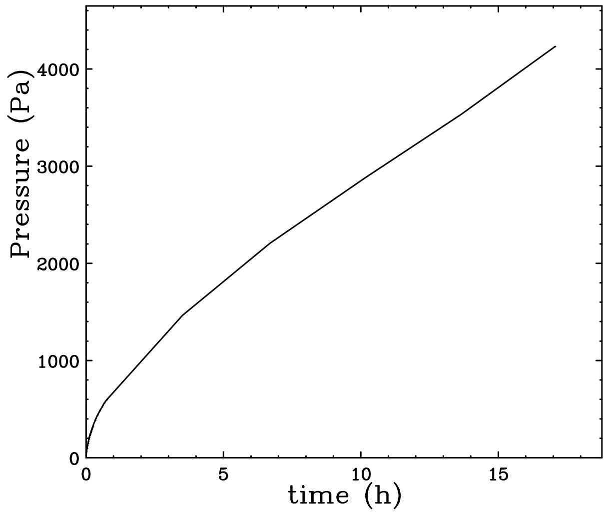

Figure 1. The variation of the pressure of the beam line connected from FE7 to S2 for 17 hours. The valves in front of the TMPs except for S2 were closed.

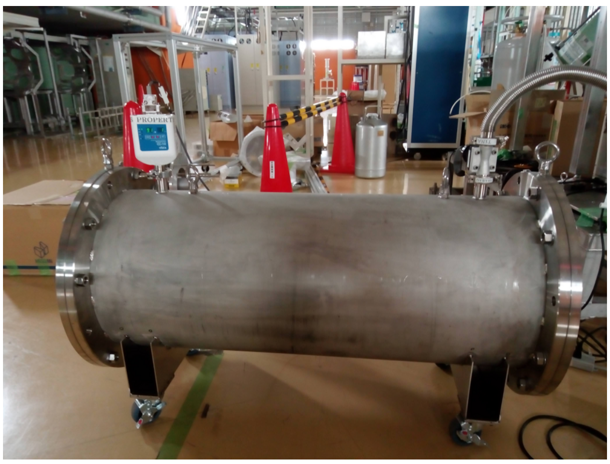

Figure 2. The buffer tank of 40 cm diameter and 100 cm length.

Besides the buffer tank, to isolate the Ti-^{3}H target at S0 from the beam line, two thin windows will be placed upstream and downstream of the target. Accordingly, to avoid breaking the foils between the target chamber and the beam-line, the differential pressure valves have been developed. When the difference is larger 3 kPa, the vacuum lines to these two areas are closed not to break the thin foils.

The experiment will be conducted in the first half of 2021.

Acknowledgment

The work was partly funded by Grant-in-Aid for Scientific Research (B) 20H01924.

References

[1] T. Sato, private communications.

Measurement of X rays from OEDO RF deflector system

S. Michimasa, N. Imai, S. Ota, T. Chillery, M. Dozono, N. Kitamura, S. Koyama, and S. Shimoura

Center for Nuclear Study, Graduate School of Science, the University of Tokyo

1. Introduction

The OEDO system [1] was launched in the end of fiscal year 2016 at RI Beam Factory to promote experimental nuclear studies via direct reactions induced by intense slowed-down RI beams at around 50 MeV/u with BigRIPS separator [2] and High-resolution beamline [3]. To obtain a slowed-down beam with a small spot size and a small energy spread, the system transforms the spreads of horizontal position and angle of the beam to the timing spread. This ion optics corresponds to the rotation of the phase space ellipse on the position-timing plane, as shown illustratively in Fig. 11 of Ref. [1]. The main components of the OEDO system are an aluminum degrader at the entrance of the system, a radio-frequency electric-field deflector (RFD) synchronized with the cyclotron's RF (= 18.25 MHz) and 2 sets of superconducting triplet quadrupole (STQ) magnets. The degrader is installed to control the beam energy, and the STQs provide a stable magnetic field to transport beam particles effectively. The RFD provides a sinusoidal electric field horizontally to rotate the phase space ellipse on the lateral-timing plane, where a voltage of $\sim$ 300 kV is typically applied between the RFD electrodes.

To date, a lot of experimental proposals using OEDO are under discussion. Among them, γ-ray spectroscopy is a potential techniques for maximizing the performance of experiments at OEDO. However, while operating the RFD, strong x rays are produced by collisions between RFD electrodes and electrons accelerated by the RF electric field. The X rays from the RFD will introduce accidental coincidences in the γ-ray spectra measured at the secondary target. With the intention of performing γ-ray spectroscopy at OEDO, we measured x-ray spectra at the secondary target location as a function of RFD operation high voltage (HV), and examined the impact of a lead shield on reducing the x-ray background.

2. Measurement

We obtained x-ray spectra by using a $CeBr_3$ scintillator with a photomultiplier tube. The detector setup is illustrated in Fig. 1. A $CeBr_3$ crystal of 1 inch in diameter and depth was set at the S0 focus, the specified site for installation of secondary targets for RI beams. Signals from the crystal were sharp with a decay time $\sim$ 70 ns, meaning the x-ray spectra were collected with almost no pile-up events. To check effectivity of x-ray shielding at the RFD, a lead plate (Pb) with a size of 1000 mm(H)$\times$1500 mm(V)$\times$8 mm(T) was set downstream of the RFD (on the same side of $CeBr_3$). Figure 2 is a photograph of the lead shield with a part of RFD. The vertical center of the plate was set to be the height of the beam axis. By using the detector setup, we measured a time structure and energy spectrum of background x-rays with and without the lead shield.

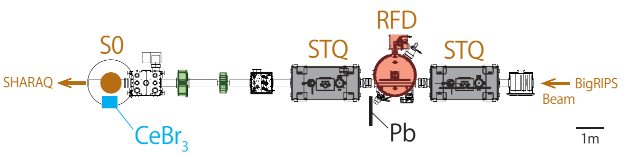

Figure 1. Detector setup for measurements around OEDO RFD. Details are written in text.

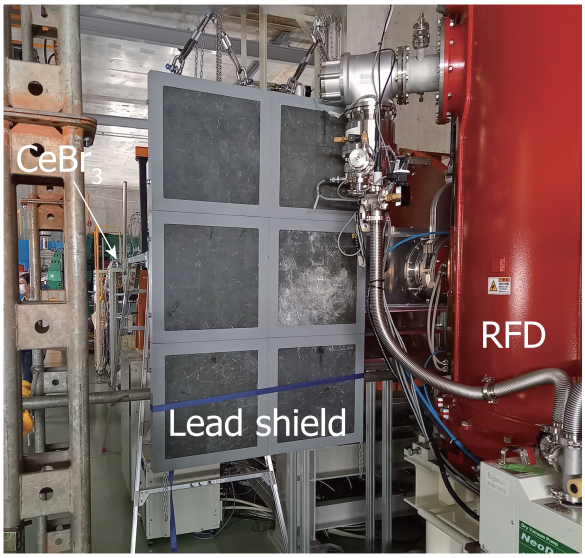

Figure 2. A photograph of the lead shield of RFD.

3. Results

The time structure of x-rays detected at S0 is shown in Fig. 3. The x axis corresponds to a phase of the applied RFD high voltage, and the colored hatches show half periods of operation frequency. The figure illustrates that the x-ray intensity strongly correlates with the function of ap-

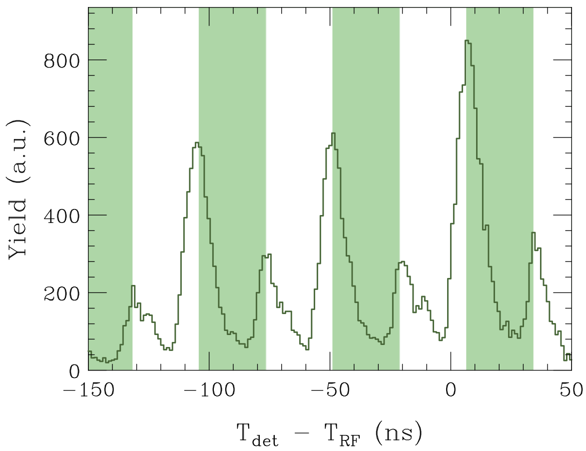

Figure 3. Time structure of x rays from RFD at S0. The shown spectrum was obtained without the lead shield.

plied voltage. Therefore, it is assumed that x rays from the RFD reach the detector with minimal scatterings on the wall, floor and/or roof of the experimental room.

Based on this assumption, the lead shield was positioned to shade the view downstream from the RFD. Figure 4 shows x-ray energy spectra, where colors indicate operation voltages of OEDO. The figure clearly illustrates a rapid in-

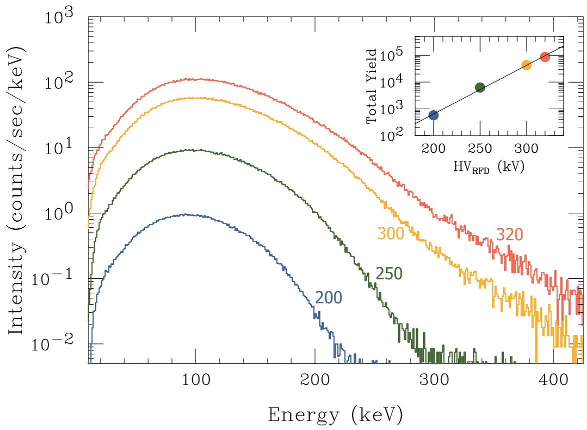

Figure 4. Energy spectra of x rays from RFD at several operation voltages. Inset shows total count rate as the function of the operation voltage.

crease of the x-ray background as the function of HV. As shown in the inset, the total x-ray count rate closely follows an exponential function. However, obtained x-ray energy distributions are relatively similar for different HVs with the exception of their intensity. The most frequent energies of the distributions are $\sim$ 100 keV in all the spectra. Therefore, to reduce the background x rays, the shielding of x rays at $\sim$ 100 keV is considered to be most efficient.

For 100-keV x rays, the reduction ratios of 20-mm-thick aluminum and 20-mm-thick iron are respectively estimated to be 7% and 94%. Therefore, heavier elements, such as lead, are suitable as a shield material for the RFD. Figure 5 shows a comparison between background x-ray energy spectra with and without the lead shield. Although the

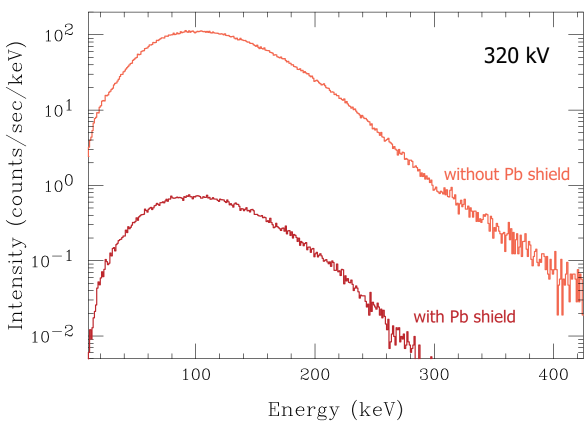

Figure 5. Energy spectra of x rays from RFD at 320 kV with and without the lead shield.

shielding area was relatively small, it was confirmed that this lead plate reduced the detection rate of background x rays by 1/164. An energy dependence of x-ray reduction is found to be almost constant. Also, it was confirmed that a shielding of the view between RFD and photon detectors was very effective. Now the background count rate of x rays could be reduced down to about 500 counts/sec, and this rate is acceptable to perform γ-ray spectroscopic studies at OEDO.

4. Perspective

The present measurement provided a positive result about x-ray background reduction by using lead shielding of the RFD. In order to effectively detect the de-excitation γ-rays from the secondary target, a lot of γ-ray detectors will be positioned to surround the secondary target at S0. Therefore, it is mandatory to increase the number of lead shield and shade direct photons from the RFD to the detectors. Soon, we will prepare the additional lead shields and examine the background reduction by using a larger shield at the RFD.

References

[1] S. Michimasa *et al.*, Prog. Theor. Exp. Phys. **2019**, 043D01 (2019).

[2] T. Kubo, Nucl, Instrum. Methods Phys. Res., Sect. B **204**, 97 (2003).

[3] T. Uesaka *et al.*, Prog. Theor. Exp. Phys. **2012**, 03C007 (2012).

OEDO Optics Study for Upcoming Measurement of the ^{130}Sn(n,γ)^{131}Sn Reaction using the Surrogate Technique

T. Chillery, S. Michimasa, J.W. Hwang[a], N. Imai, S. Ota, S. Shimoura, K. Yako

Center for Nuclear Study, Graduate School of Science, University of Tokyo, Wako, Saitama 351-0198, Japan
[a] Center for Exotic Nuclear Studies, Institute for Basic Science (IBS), Daejeon 34126, Rep. of Korea

Construction of the OEDO (Optimized Energy Degrading Optics) system [1] was completed in 2017. The principle aim of OEDO is to provide medium-heavy energy-degraded radioactive ion (RI) beams for both nuclear physics and nuclear astrophysics studies. The system is designed to slow down beams provided by the BigRIPS SRC from ~ 200 MeV/u to $15-50$ MeV/u, thereby accessing a mass-energy region previously unreachable by current RI beam facilities. Experiments performed at OEDO can also incorporate the high-resolution SHARAQ spectrometer located downstream of OEDO. Details of SHARAQ may be found in reference [2]. The OEDO-SHARAQ system has already been used in the study of transfer reactions on ^{77,79}Se, ^{93}Zr, and ^{107}Pd. Data analysis of these studies is ongoing and results are expected to be published soon.

Following this early success, a new experiment was accepted for machine time (MT) at BigRIPS-OEDO to measure the ^{130}Sn(n,γ)^{131}Sn reaction cross-section using the surrogate technique. Situated close to the N=82 second *r*-process peak, ^{130}Sn is an essential probe to confirm astrophysical production sites of isotopes heavier than iron. Results from this study are expected to expand our knowledge of present reaction rates in the A=130, N=82 region of the nuclear chart, thereby improving the *r*-process calculations. This report covers the work performed in fiscal year 2020 towards finding a good optics solution for the OEDO experiment.

Beamtime is expected to be allocated during spring 2022. A ^{130}Sn^{50+} beam will be produced at F0 by bombarding a 3 mm thick ^{9}Be target with a 345 MeV/u ^{238}U^{86+} beam. The ^{130}Sn will be accelerated into the BigRIPS beamline at energy 338 MeV/u and subsequently slow down through Al degraders to an energy 20 MeV/u at the S0 focus in OEDO. At S0 a solid CD_2 target of thickness 0.3 mg/cm^2 will be installed, and surrounded by the TINA silicon-detector array [3]. For this study the angle-tunable wedge degrader at FE9 and the OEDO RF deflector (RFD) located at FE10 will be required to filter the beam energy at S0, and the first half of SHARAQ (two quadrupoles and one dipole) will be used to analyze the reaction fragments at S1.

The beam trajectories calculated by ion-transport code COSY between F3 - FE9 are shown in figure 1. The beam parameters (in 1 œ) at F3 were assumed to be x = 3 mm, a = 20 mrad, y = 3 mm, b = 30 mrad, and δ = 3.5 %. The 1st order matrix elements are provided in table 1. The F3 - FE9 focusing is set as dispersive focus, and for the present study is described by $(x|\delta)_{\text{F3-FE9}} \simeq 12$ mm/%.

Precise control over the secondary beam energy and focusing at S0 will be possible by using an angle-tunable

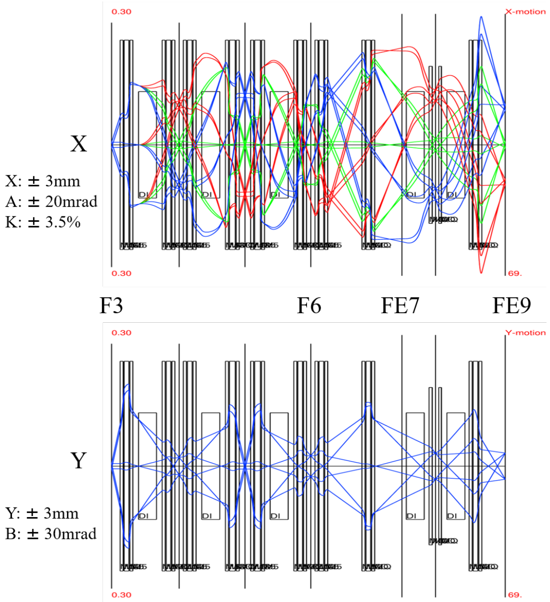

Figure 1. COSY-calculated 1st order beam trajectories in the X and Y planes between F3 - FE9 for upcoming ^{130}Sn study at OEDO-SHARAQ.

Table 1. COSY matrix elements of F3 - FE9 for present OEDO configuration. The reference particle is ^{132}Sn at 279 MeV/u. x and y in mm, a and b in mrad, and δ is energy dispersion in %.

	|x)	|a)	|y)	|b)	|δ)
(x|	+1.03	+0.00	+0.00	+0.00	+12.03
(a|	+1.07	+0.97	+0.00	+0.00	-0.97
(y|	+0.00	+0.00	-5.00	+0.00	+0.00
(b|	+0.00	+0.00	-1.69	-0.20	+0.00
(δ|	+0.00	+0.00	+0.00	+0.00	+1.00

wedge degrader [4] installed at the FE9 focal position of OEDO. The FE9 degrader consists of two aluminum plates each with a quadratic cross section, with a total thickness x given by the function:

$$f(x) = (4c_1x_0 + 2c_2)x + d_0$$

where x_0 is the horizontal offset between the two plates, and c_1 and c_2 are coefficients $1/9000$ mm^{-1} and 0.01, respectively. The wedge angle, α, is calculated as $\tan^{-1}(4c_1x_0 + 2c_2)$ and the central thickness is $d_0 = 3$ mm. The wedge angle may therefore be varied between $0-40$ mrad by adjusting x_0 between -45 and $+45$ mm. The central degrader thickness at FE9 may be increased by d_1 using additional Al flat plates downstream from the wedge degrader. For the planned BigRIPS degrader configuration an additional flat degrader of thickness $\sim$ 5.1 mm at FE9 is required to slow down[2] the ^{130}Sn to the desired 20 MeV/u energy. The degrader angle is calculated as [4]:

$$(\delta|\delta)_{\text{total}} = (\delta|x)_{\text{d}}(x|\delta)_{\text{F3-FE9}} + (\delta|\delta)_{\text{d}}$$

where we introduce [5]:

$$(\delta|x)_{\text{d}} = \frac{-1}{\gamma R\left(1-\frac{\text{d}_0+d_1}{R}\right)}\left(\frac{\text{ffi}d}{\text{ffi}x}\right)_{x=0}$$

$$\gamma = \frac{\ln\left(1-\frac{\text{d}_0+d_1}{R}\right)}{\ln\left(\frac{E_{\text{d}}}{E_0}\right)}$$

$$(\delta|\delta)_{\text{d}} = \frac{1}{1-\frac{\text{d}_0}{R}}$$

where R is the total range through the degrader, E_0 and E_{d} are the beam energies pre- and post-degrader, respectively, and $\left(\frac{\delta d}{\delta x}\right)_{x=0}$ is the degrader angle, $\tan(\alpha)$. To achieve the desired mono-energetic beam post-degrader, the condition $(\delta|\delta)_{\text{total}} \sim 0$ is imposed. For a ^{130}Sn beam of energy 173.9 MeV/u incident on a 5.1 mm Al degrader, a calculated degrader angle $\alpha = 6.9$ mrad is required for $(\delta|\delta)_{\text{total}} < 0.1$. This wedge angle was independently verified with Monte Carlo simulation code "beamsimu" originally written by J.W. Hwang.

In addition to the FE9 degrader, the RFD parameters, specifically voltage and phase, need to be tuned to filter the desired 20 MeV/u ^{130}Sn for this study. The optimal parameters were determined using the "beamsimu" code, which models the RF effect on the beam position, x, and angle, a, as a function of peak voltage, V_0, and phase, ϕ [6]:

$$\begin{aligned} x =& x_0 + la_0 + \frac{1}{B\rho}\frac{V_0}{dw}\cos(\phi) \\ &+ \frac{1}{B\rho}\frac{lV_0}{dw^2T}\left[\sin(\phi) - \sin(wT+\phi)\right] \\ a =& a_0 + \frac{1}{B\rho}\frac{V_0}{dw}\left[\cos(\phi) - \cos(wT+\phi)\right] \end{aligned}$$

where l is the RFD electrode length (1.2 m), d is the RFD electrode separation (0.2 m), $B\rho$ is the beam's magnetic rigidity, T is the time-of-flight through the RFD, w is the angular frequency[3], and x_0 and a_0 are the beam ion's initial position and angle, respectively. To determine ideal RFD settings the "beamsimu" code simulated a range of phases and voltages. Figure 2 shows the ^{130}Sn horizontal position at target position S0, gated on beam energy 20 ± 2 MeV/u, for different phases (V_0 fixed at 180 kV) and voltages (ϕ fixed at 80^o). The optimal RFD settings simulated for this study are $\phi = 80^o$ and $V_0 = 215$ kV, however the S0 horizontal position of $1\sigma = 37$ mm is broader than the CD_2 target radius $r_{\text{targ}} = 25$ mm, which is clearly undesirable.

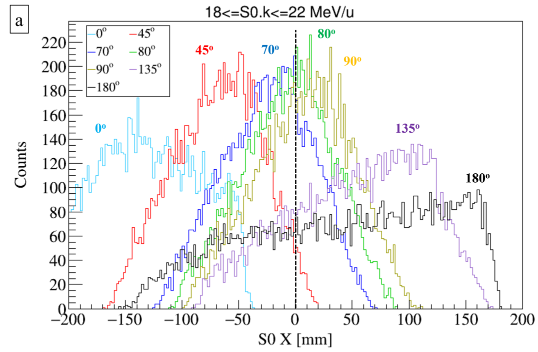

7.3cm

(a) b

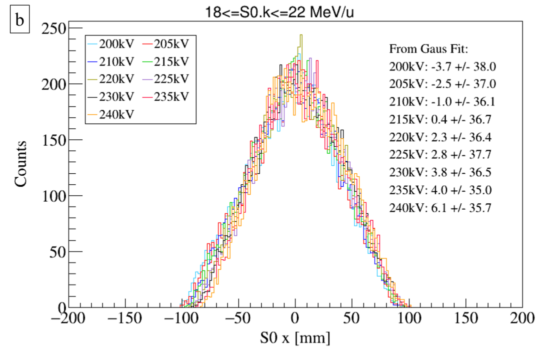

7.3cm

(b) b

Figure 2. Horizontal position at S0 determined by "beamsimu" code when adjusting a) RFD phase or b) RFD voltage. An RFD setting of phase = 80^o and voltage = 215 kV looks optimal, however the width needs reducing to match the target radius (25 mm).

The focusing power of the OEDO beamline is inhibited by its weakest magnet, which is presently the QE19 quadrupole located between focal positions FE11 and FE12. To remove this limitation the FE10 - FE12 section of the OEDO beamline will be reconfigured in spring 2021 such that QE19 is no longer used. The planned setup is expected to both improve the horizontal focusing at S0 and increase the F3 - S0 transmission by approximately threefold. This future setup will be used for the first time by experiments during the BigRIPS-SHARAQ light-ion campaign, scheduled between May - June 2021. Following this campaign the optimal optics conditions will need to be recalculated for the ^{130}Sn study, the MT of which is expected to run during spring 2022.

References

[1] S. Michimasa *et al.* PTEP **043D01** (2019).

[2] S. Michimasa *et al.* NIM B **317** 305-310 (2013).

[3] P. Schrock *et al.* RIKEN Accel. Prog. Rep. **51** 20 (2018).

[4] J.W. Hwang *et al.* PTEP **043D02** (2019).

[5] T. Shimoda *et al.* NIM B **70** 320-330 (1992).

[6] K. Yamada, T. Motobayashi, and I. Tanihata Nucl. Phys. A **746** 156c-160c (2004).

[2] Range and energy loss determined from ATIMA 1.2 stopping-power tables.

[3] $w = 2\text{ß}f$ where f is the BigRIPS SRC RF = 18.25 MHz

Development of a method for position calibration for SR-PPAC

S. Hanai, S. Ota, R. Kojima, M. Dozono, N. Imai, S. Michimasa, S. Shimoura, J. Zenihiro[a], K. Inaba[a], Y. Hijikata[a]

Center for Nuclear Study, Graduate School of Science, The University of Tokyo
[a]Department of Physics, Kyoto University

Strip Readout PPAC (SR-PPAC) is a tracking detector for heavy ion aimed at high efficiency and position resolution even for high intensity RI beams. SR-PPAC has a fast responce owing to correcting the signals of electrons from each strip of cathode plane individualy and directly. We have tested its parformance using ^{132}Xe beam with intensity of 700 kppp and obtained 230 μm (FWHM) reslution which can be comparable to LP-MWDC [1,2].

For the position extraction, charge distribution on the cathode plane is uesd. Figure 1 shows a induced charge distribution on a cathode plane. ID_0, ID_1 and ID_2 denote the highest charged-strip and the second-highest and the third respectively, Define Q_0, Q_1 and Q_2 as the amount of charge of ID_0, ID_1 and ID_2. There is a correlation between the charge difference, Q_0 - Q_1, and the beam position. The correlation is generally non-linear. However, assuming the uniformity of the beam distriution, the integration value of Q_0 - Q_1, define as δq, can be written as the single-valued funciton of the beam position. The distance from the edge of strip to the beam position, defined as δx, is given by the following formula,

$$k(\delta q) = \frac{\int_0^{\delta q} f(q)dq}{\int_0^{Q} f(q)dq} \tag{1}$$

$$\delta x = \frac{s}{2} \times k(\delta q) \tag{2}$$

where $k(\delta q)$ is the conversion coefficient as a function of the charge difference given by a integral of a distribution of charge difference $f(q)$. Q represents the maximum value of charge difference. s in the formula (2) is the strip size of the cathode. For instance, in the case that a beam comes to center of a strip, δq will be Q or δx is zero, and when a beam comes to edge of a strip, δq will be zero or δx is the half of a strip size. Figure 2 shows an example of a distribution of charge difference which is corresponding to f in the formula (1), and the conversion coefficient k derived from f. In the end, the beam position will be given by the following formula.

$$x = x_0 \pm (\frac{s}{2} - \delta x) \tag{3}$$

where x_0 is the position of the strip ID_0. The pluse or minus sign in the formula (3) is determined depending on which side of ID_0 a beam passed through.

In the previous study, we realized that the position distribution calculated by SR-PPAC has position dependence. Figure 3 shows the correlation between beam position calculated using LP-MWDC as a reference and its difference between positoin calculated using SR-PPAC. The deviation of Y-axis is correspoinding to the resolution of the detectors. Top two figures are the correlations calculated in the manner of formula (3). The right figure shows distribution of one strip. There are peaks at center of the strips and the distribution is discontinuous. When the beam comes around center of a strip, the value of Q_1 and Q_2 is almost the same, Therefore, the second highest charged strip can not be selected correctly due to the fluctuation. Consequentaly, the resolution become worse around center of strips, as seen in Fig.3.

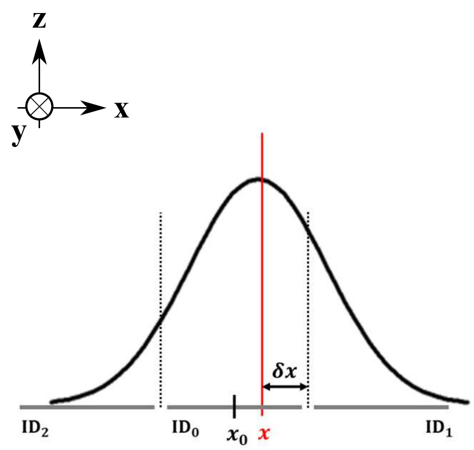

Figure 1. Illustration of charge distribution induced on the striped cathode. ID_0,ID_1 and ID_2 represents the highest-, the second-highest, and the third-highest charged strip respectivly.x is beam position and δx is distance from the edge of a strip. The z axis is along the beam direction.

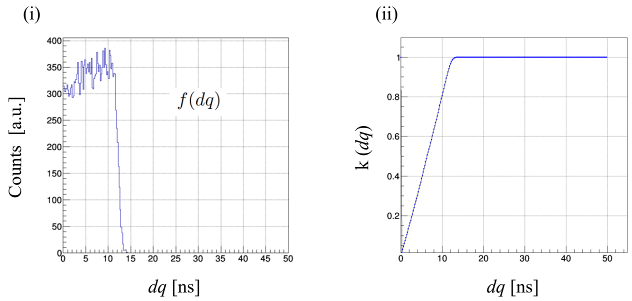

Figure 2. (i) Example of distribution of charge different between Q_0 and Q_1 denoted as dq. The distribution is correspoinding to f in formula (1). (ii) Conversion coefficient for calculating position from charge difference.

This problem can be solved by using a method without selecting Q_1 strip considering the amount of charge. First, calculate the conversion coefficiant using a difference between Q_0 and charge of the left side strip of ID_0 and the position. In the same way, calculate the position using difference between Q_0 and charge of the right strip . Finally, take the charge wighted average of x_L and x_R as following.

$$x = \frac{(Q_0 - Q_R)}{(2Q_0 - Q_L - Q_R)} \times x_L + \frac{(Q_0 - Q_L)}{(2Q_0 - Q_L - Q_R)} \times x_R \tag{4}$$

where Q_L and Q_R are the charge of left or right side strip and x_L and x_R are the position derived by $Q_0 - Q_L$ and $Q_0 - Q_R$.

The bottom two figures of Fig.3 show the result of the calculation using formula (4). The position dependence as seen in the top figures is improved and the distribution is continuous. The position resolution overall is improved by 10 μm (σ).

The position dependence of resolution within a strip can be improved by this new method, but the distribution remains zigzag corresponding to strip size as seen in left figure of Fig.3. This may be caused by the difference of gain of each strips. We are now going to develop a way of calibrate the charge of strips.

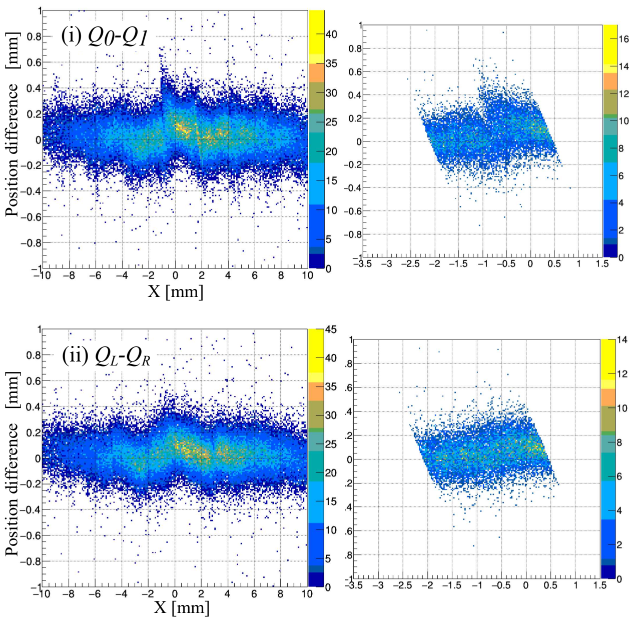

Figure 3. (i) The correlation between reference position and difference between the reference and position calculated by SR-PPAC. The deviation of Y-axis is corresponding to the position resolution. The right figure shows the distribution of one stip. The strip size was 2.55 mm. The distribution is discontinuous at center of the strip. (ii) The result of new method descrived as formula (4).

References

[1] H.Miya, *et al.*, Nucl. Instrum. Meth. Phys. Res., Sect. B, **312**, (2013) 701.

[2] S.Hanai, *et al.*, CNS Annual Reposrt.2019 **317**, (2021).

Development of a Positioning Extraction Method for Position-Sensitive Ge Detector GRAPE Using Machine Learning

S. Sugawara[a], D. Nishimura[a,b], N. Imai[b], H. Takahashi[a], and S. Shimoura[b]

[a]*Department of Natural Sciences, Tokyo City University*
[b] *Center for Nuclear Study, the University of Tokyo*

One of the difficulties associated with in-beam gamma-ray spectroscopy experiments is that the energy resolution of gamma-rays emitted from nuclei deteriorates due to the effect of Doppler shift. Therefore, it is important to develop a position-sensitive gamma-ray detector that can compensate for the Doppler shift accurately in order to study the nuclear structure with high resolution. The position-sensitive Ge detector GRAPE (Gamma-Ray detecter Array with Position sensitivity and Energy) can derive the position of gamma-ray interaction in the detector using waveform analysis.

GRAPE is a Ge detector array consisting of 18 detectors with gamma-ray interaction position sensitivity. Inside the hexagonal metal container, there is a cylindrical crystal of 70 mm diameter and 20 mm thickness. Two Ge crystals sandwich an anode of 70 mm diameter (applied voltage 2000 V). The cathode is circular in shape with a diameter of 60 mm and is divided into 3×3 segments, each of which reads the signal independently. x, y, and z axes are defined as shown in Fig. 1.

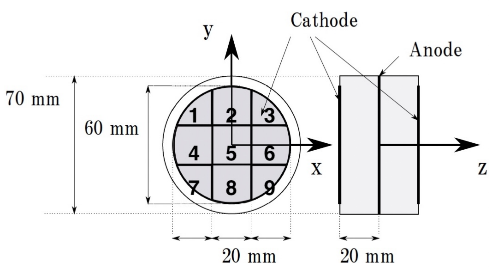

Figure 1. Crystals in one detector of the GRAPE and definition of the spatial axis

For the data acquisition system, we used the APV7110 module from Techno AP, a VME-type radiation measurement device equipped with Digital Signal Processing (DSP).(Fig. 2.) It has a built-in internal clock and timestamps the event data at 10 ns intervals. The TCP/IP protocol is used for data communication between the module and the CPU.

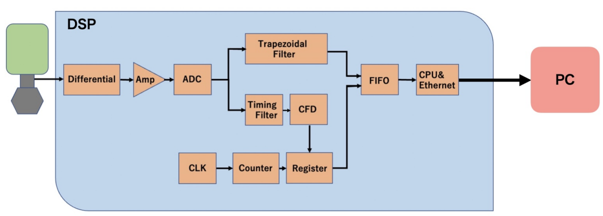

Figure 2. Schematic diagram of the elecrical circuits in APV7110.

In the experiment, we focused on the events where the gamma rays entering the 6th segment caused 90 degree Compton scattering and the scattered gamma rays were detected at the 3rd and 9th segments in the Ge crystal. A diagram of the setup is shown in Fig. 3. The incident gamma rays are scattered through a lead collimator of 2 mm diameter and 60 mm thickness to narrow down the scattering angle. The gamma-ray source used was 2-MBq of ^{137}Cs (CS516CE, JRIA). The distance between the gamma-ray interaction point and the anode (z-axis direction) was changed to z=0, 4, 8, 12, 16, and 20 mm, and the z-dependence of the waveform was confirmed. a two-axis electoric actuator (EZHS6A-20 and EZHS4A-20M, ORIENTAL MOTOR Co.,LTD) was used to change the z-axis direction. The electric actuator can move 0.01 mm per pulse, so we used a USB GPIO to control the actuator with 0.01 mm accuracy.

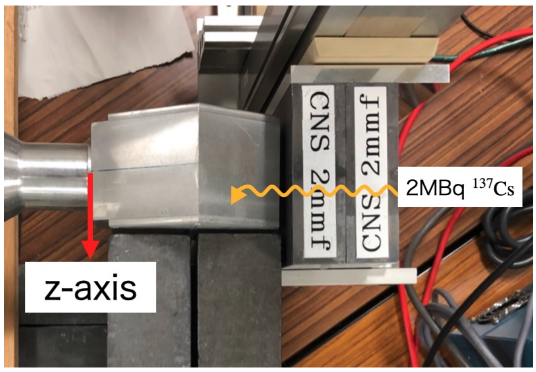

Figure 3. Top view of the experimental setup

For the event construction and data analysis system, we used "Fruit" and "Juice", which are developed by Yamaguchi *et al*. [2]. The typical waveforms of the nsegments when the gamma rays interacted with the sixth segment are shown in Fig. 4. Here we can see that segments 3, 5, and 9, which are adjacent to the sixth segment, also have characteristic waveforms. The output waveforms of the nine segments after narrowing down the events are shown in Fig. 5 Here, the scale of the vertical axis is changed between the waveform of the segment where the gamma rays first interacted and the waveform of the other segments.

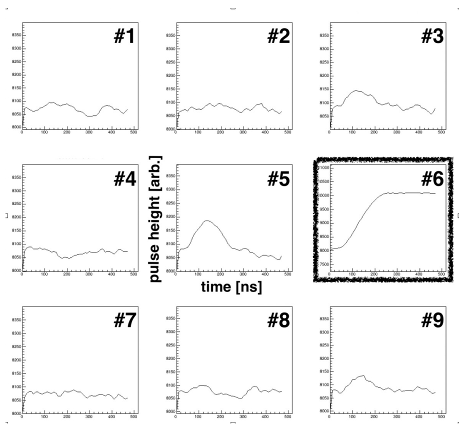

Figure 4. Waveforms of a 662-keV gamma ray interacting with only the sixth segment.

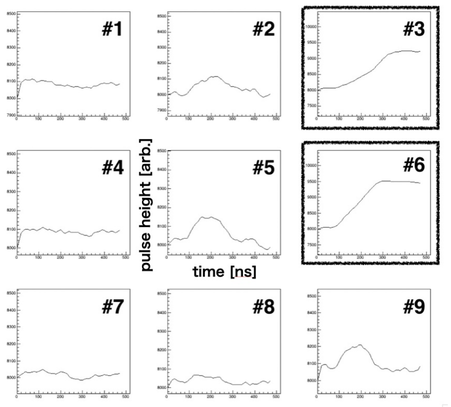

Figure 5. Waveforms of a 662-keV gamma ray interacting in not only the sixth segment but also the third segment.

Figure 6 shows the z-dependence of the waveform of the sixth segment, where the averages of about 50 events were drawn at z = 0, 4, 8, 12, 16, and 20 mm, respectively.

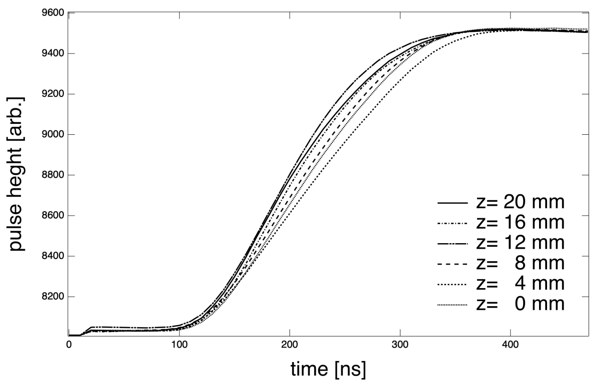

Figure 6. The z-dependence of the waveform of the sixth segment.

For machine learning, the success rate of waveform classification was 25% when 1st, 2nd, 3rd, and 4th order moments were used as features. The reason for the low classification success rate is the small amount of data and the large uncertainty of the gamma-ray interaction point caused by the angular fluctuation of the incident gamma rays. In the future, We plan to perform experiments with setups that allows us to minimize the uncertainty of the gamma-ray interaction points as much as possible, and analyze the waveforms using deep learning libraries such as `Keras`. The deep learning is a technology that can be used to learn data without any human intervention, from feature design to feature selection. The relationship between the waveform and the z position can be trained by using the teacher data of the gamma-ray sources. By using the training results, the actual interacting points of the gamma rays emitted from the nuclei in beam will be deduced.

References

[1] S. Shimoura, Nucl. Instrum. Meth. Phys. Res. A**515** (2001) 188.

[2] Y. Yamgaguchi *et al*., CNS Annual Report 2015 (2016) 53.

Development of neutron radiation shielding at CRIB

S. Hayakawa, N. R. Ma, K. Okawa, H. Shimizu, and H. Yamaguchi

Center for Nuclear Study, Graduate School of Science, University of Tokyo

CRIB [1–3], a low-energy radioactive isotope (RI) beam separator of the Center for Nuclear Study, has been in operation for almost 20 years since it was launched. With accumulating experience and developments of experimental devices such as the Wien filter and the cryogenic system for the primary gas target [4], the beam intensity is increasing year by year. Currently, the primary gas target body, installed in the F0 chamber, is also under further development aiming at higher heat durability against beam injection. Although maximizing beam intensity is preferred for RI beam experiments in general, it may also poses a challenge to the experimental devices. One of the serious problems that we face is the damage of the electronics involving semiconductor devices presumably by radiation of fast neutron-rays ($>$ 500 keV) associated with the secondary beam production. Such problems often interrupt the machine time for losing communication to these devices (such as the programmable logic controllers of the CRIB touch panel for the drive and vacuum systems). Therefore, controlling neutron radiation to protect them is particularly important in recent and future CRIB experiments with increase of beam intensity.

We firstly surveyed neutron radiation distribution in Room E7 of RIKEN Nishina Building, where CRIB settles, to identify the main neutron-ray source. The measurement was done with an actual beam (^{24}Mg, 7.5 MeV/u, 0.39 pμA) impinging on the primary target (^{3}He gas at 230 Torr confined by 3-μm-thick Ti windows) at F0 using eight thermoluminescence dosimeters (TLDs) and two permanent area monitors. The position arrangement of the TLDs and the area monitors and the measured doses after the machine time are shown in Fig 1. It clearly shows that F0 chamber is the main neutron-ray source with the highest dose of 7756 μSv rather than the bending magnet between F0 and the AVF cyclotron or the beam dump inside the D1 magnet. The distribution of the dose measured at each position is written in Fig. 1.

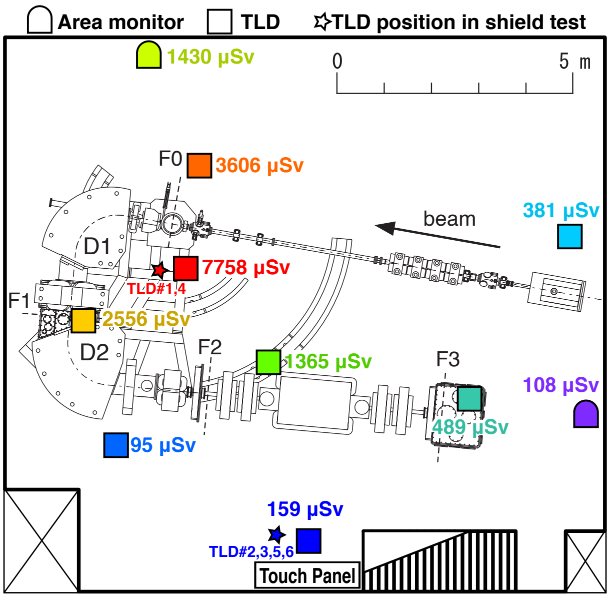

Figure 1. Neutron dose distribution in Room E7 of Nishina Building with the ^{24}Mg beam, surveyed by TLDs and the permanent neutron area monitors. The stars indicate the TLD positions and the numbers identify the TLDs used in the neutron shield test with the ^{16}O beam.

The result suggests that there is a possibility to reduce the neutron radiation by surrounding the F0 chamber with materials to primarily slow down neutron rays. Polyethylene (PE) is commonly used for this purpose because it contains many hydrogen atoms which effectively absorb neutron kinetic energy by elastic scattering. The energy of the neutron ray at CRIB is considered as of the order of MeV at most because the typical primary beam energy is less than 10 MeV/u. The dose of a-few-MeV neutron rays may be reduced to 1/10 by PE blocks with a thickness of 20–30 cm [5]. Once the neutron velocity distribution are moderated,

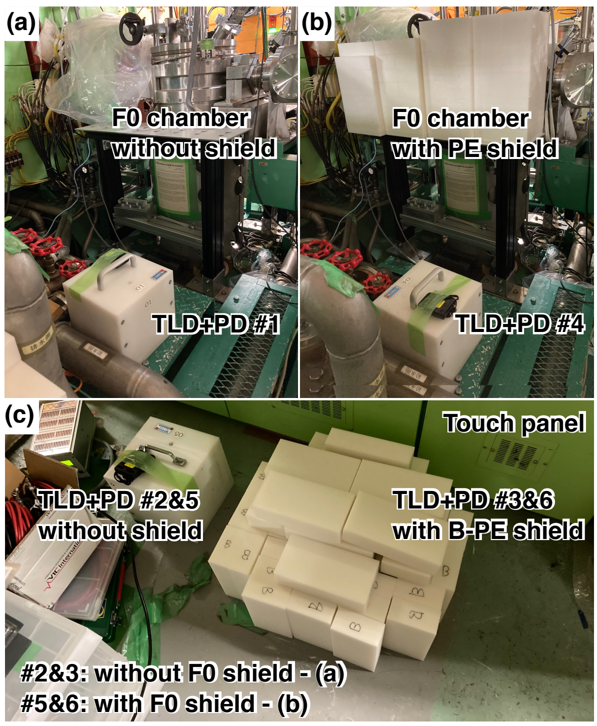

Figure 2. Photographs of the setups for the neutron shield test with the ^{16}O beam. The TLD numbers (TLD+PD #1, etc.) correspond to those in Fig. 1 and Table 1. (a) TLD+PD set by F0 chamber without neutron shield. (b) That with neutron shield of the pure PE blocks. (c) Two TLD+PD sets with and without neutron shield of the B-PE blocks in front of the touch panel.

Table 1. Neutron doses and the counts of the fast (FN) and slow (AN) neutrons with several neutron shield settings. The TLD numbers are according to those in Fig. 2. Note that the values with the F0 shield are normalized by the total injected beam charge to that without the F0 shield.

TLD No.	F0 PE Shield	TLD B-PE Shield	TLD dose (μSv)	PD dose (μSv)	FN counts	AN counts
1			2511.8±9.5	1150	72	431
2			78.0±7.4	62	2	42
3		Yes	6.9±4.5	13	1	3
4	Yes		1552±100.0	429.1	20	231
5	Yes		36.8±2.5	38.0	0	38
6	Yes	Yes	7.9±2.2	7.1	0	7

the slowed-down neutrons can be absorbed more easily by neutron-absorbing material such as boron. Boron-added PE blocks (B-PE, B_2O_3 content of 10%) are suitable for this purpose, surrounding the electronic devices to protect them.

To verify this assumption, we made another beam test with pure PE and B-PE blocks actually mounted, directing an ^{16}O primary beam (6.8 MeV/u, 0.3 pμA) on the F0 target (^{4}He gas at 230 Torr confined by 3-μm-thick Mo windows). We repeated measurements without and with putting PE blocks covering the F0 chamber for comparison. For each F0 shield setting, we put one TLD by the F0 chamber and two TLDs in front of the touch panel as shown in Fig. 2, of which positions indicated by star marks in Fig. 1. One of the two touch-panel TLDs had no shield, and the other was covered by B-PE blocks to compare their effect. A personal dosimeter (PD) is accompanied with each TLD for reference.

The results of the measurement are listed in Table 1. It shows neutron doses measured by the TLDs and the PDs for TLD#1–6, corresponding to different setting positions and neutron shield conditions. The PDs also measured the counts of the fast (> 500 keV) and slow (< 200 keV) neutrons, labeled as FN and AN in Table 1, respectively. Note that the values with the F0 shield (TLD#4–6) are normalized by the total injected beam charge to that without the F0 shield (TLD#1–3), namely, 1.97 pμAh/1.56 pμAh $\sim$ 1.26. Figure 3 visualizes the results of the TLD and PD doses. There is a clear trend that the dose decreases with the F0 shield; F0 dose (#1 $\rightarrow$ #4) was reduced to 40–60%, touch-panel dose without the B-PE shield (#2 $\rightarrow$ #5) to about 50%. The touch-panel dose with the B-PE shield (#3 $\rightarrow$ #6) was close to the detection limit of about 10 μSv, thus has larger errors than the other measurements and does not show a significant change. The reduction by the F0 shield was not a factor of 10 even with the PE thickness of 20 cm as mentioned above, but this is understandable because the coverage of the F0 chamber by the PE blocks is mostly limited to the horizontal direction (i.e., 1/4–1/3 of the total solid angle). By comparing doses of #2 to #3 or #5 to #6, we confirmed that the dose was reduced to 10–20% thanks to the B-PE shield. Another important fact was that the number of fast neutrons was reduced to about a half by taking ratios of FN/AN counts; at F0, FN/AN ratio was 0.17 (#1) and

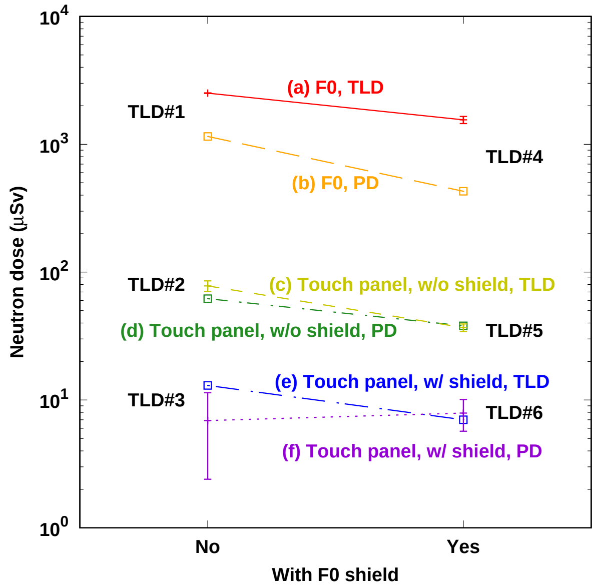

Figure 3. Neutron doses measured by the TLDs and the PDs with several neutron shield settings.

0.0087 (#4) without and with the F0 shield, respectively; at the touch panel, the FN counts (#5 and #6) were even zero with the F0 shield although the statistics were limited.

In conclusion, we have newly installed PE blocks surrounding the F0 chamber of CRIB to slow down the beam-induced neutron-rays, and B-PE blocks to protect principal electronic devices by further deceleration and absorption of neutrons. Since the coverage of the F0 shield is limited to the horizontal direction, it only offers the reduction of neutron dose of about 50% or so. However, we also confirmed that it significantly reduces the percentage of fast neutrons, so that the neutron dose would be more efficiently reduced by the B-PE blocks to about 1/5–1/10. The result suggests that the combination of the PE and B-PE blocks is useful to protect electronic devices in CRIB experiments, which should be evaluated in the actual future beam times. A further reduction of neutron radiation is possible in principle by thicken PE blocks and/or improving the coverage of the F0 chamber in case of necessity.

References

[1] S. Kubono *et al.*, Eur. Phys. J. A **13** (2002) 217.

[2] Y. Yanagisawa *et al.*, Nucl. Instrum. Meth. A **539** (2005) 74.

[3] H. Yamaguchi, D. Kahl and S. Kubono, Nucl. Phys. News Int. **30** (2020) 21.

[4] H. Yamaguchi *et al.*, Nucl. Instrum. Meth. A **589** (2008) 150.

[5] 原子力安全技術センター, “放射線施設のしゃへい計算実務マニュアル 2015”, 放射線障害防止法出版物編集委員会 (2015).

The effect of axis-buncher on the injection beam line of AVF Cyclotron

Y. Kotaka, K. Kamakura, H. Yamaguchi, N. Imai, Y. Sakemi, T. Nagatomo[a], T. Nakagawa[a], J. Ohnishi[a], A. Goto[a], M. Kase[a], K. Hatanaka[b], S. Shimoura

Center for Nuclear Study, Graduate School of Science, University of Tokyo
[a]RIKEN Nishina Center
[b]Research Center for Nuclear Physics, Osaka University

1. Introduction

To increase the beam intensity of AVF Cyclotron, it is necessary to optimize the injection beam transport system. Therefore, we have developed a pepper-pot emittance monitor [1] (PEM_IH10) and a method of calculating the beam trajectory by using the (x, y, x', y') distribution measured with PEM_IH10 [2, 3] as the initial distribution.

Our next step is to evaluate the space charge effect due to the beam compression in the longitudinal direction at the axis-buncher. To estimate this effect, the equations of 3-dimensional (3D) motion of ions need to be solved. Although some existing calculation codes of beam transport was considered, it was found that they did not fit our purpose. For example, OPAL is 3D beam transport calculation code [4] , but it meets only one bunch of beams and does not meet the change from DC beam to bunching beam. Thus, we decided to calculate the effect by macro-particle model.

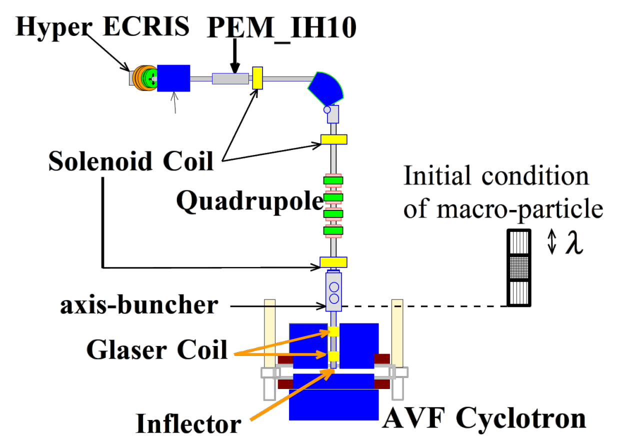

Figure 1. The schematic view of AVF cyclotron The axis-buncher is located just above AVF cyclotron. After axis-buncher, beam goes through 2 Glaser-Coils in the hole of iron yoke and reaches inflector.

2. the calculation with macro-particle model

A macro-particle is composed of multiple ions. In our case, we use the positions, angles, and electric charge measured by PEM_IH10 for the initial value of macro-particles. This time, 15.4 keV $^4He^{2+}$ ion beam of 261 eμA is measured. And the measured values are transported to the position of axis-buncher by our beam trajectory calculation. Then, the horizontal position (x, y) distribution at axis-buncher shown in Fig. 2 is given as initial values for the calculation of macro-particle model. In addition, macro-particle model needs to expand the (x, y) distribution, which we call "layer", into the longitudinal direction (z). The interval between layers should be shorter for reliability but it costs longer calculation time.

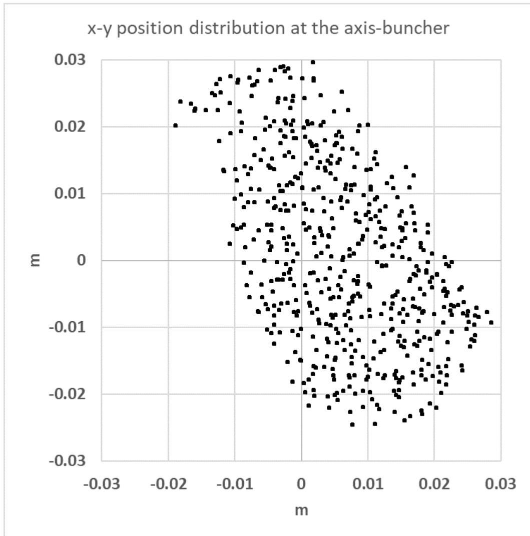

Figure 2. The horizontal position (x, y) distribution at axis-buncher transported from PEM_IH10 by our beam trajectory calculation.

To consider the longitudinal expansion length, we introduce "λ" as the flight length of ion beam during 1 cycle of periodic buncher voltage. Figure 3 shows the periodic buncher voltage with a cycle of 60 nsec, which is used for this calculation of macro-particle model. By the way, λ does not depend on the cycle and is always 52 mm for RIKEN AVF Cyclotron. Then, the longitudinal expansion length is set as 3 λ (=156 mm) like 3 hatching squares indicated in Fig. 1 because the macro-particles in the center λ indicated as the checked region in Fig. 1 are affected by the previous and next λ indicated as the striped region in Fig. 1. For analysis, only center λ region is used because it is close to real beam condition. The interval between layers is set as 5 mm so that 31 layers are used for the calculation of macro-particle model. The motion of a macro-particle is governed by the electromagnetic forces caused by all the other macro-particles. The equations of motion of all the macro-particles are solved. Then, they are sequentially moved forward at 5 mm interval from axis-buncher to the inflector of AVF Cyclotron indicated in Fig. 1. The initial beam intensity is assumed to be 500 eμA at the axis-buncher. The charges of macro-particles are given in proportion to their measured signal strength. This 500 eμA is two or three times as much as a typical injection beam intensity. Buncher voltage indicated in Fig.3 is given to every layer depending on the time(phase) only when evrey layer goes through the axis-buncher.

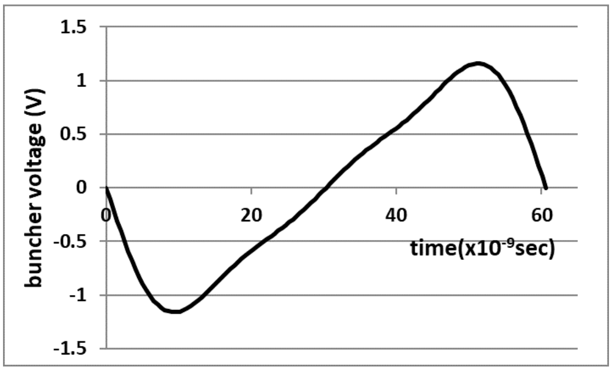

Figure 3. A cycle of buncher voltage.
$V = V_0 \cdot \{\sin(2\pi f \cdot t) - \sin(4\pi f \cdot t)/3 + \sin(6\pi f \cdot t)/9\}$
In this figure, V_0 = 1 V and f = 16500000 Hz

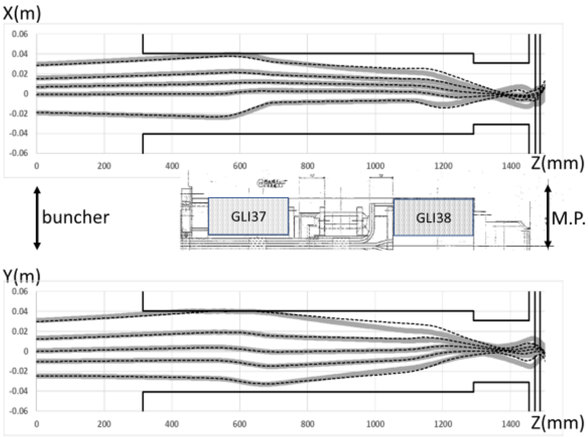

Figure 4. The comparison of beam envelope between our beam trajectory calculation (black dotted curve) and macro-particle model (gray heavy curve) for V_0 = 0 from axis-buncher to the inflector of AVF Cyclotron. Ion beam is $^4He^{2+}$ 15.4 keV of 500 eμA. The curve at the center (third one from the top in each panel) indicates the average of the position distribution at each z position along the beam direction. The curves on both sides of the curve at the center are the standard deviation of position distribution. Both outer curves are the orbits of the outermost particles. Top and bottom figures are X and Y envelopes, respectively. GLI37 and GLI38 are Glaser coils.

To see that the calculation of macro-particle model is reliable, it is compared with the result of our beam trajectory calculation indicated in Fig. 4. When V_0 defined in Fig. 3 is 0, both results are comparable and should be same. In Fig. 4, the beam envelope of our beam trajectory calculation is black dashed curves and macro-particle model is gray heavy curves. They are described from axis-buncher to the inflector of AVF Cyclotron. Although the degree of focusing by two Glaser Coils is a little different between them, both envelopes are very similar. From this result, the calculation of macro-particle model is found to be consistent to our beam trajectory calculation.

3. Estimating the effect of axis-buncher

As the calculation of macro-particle model is found to be reliable, the effect of axis-buncher is estimated. Using only macro-particle model in this comparison, we calculated the envelope with V_0 = 200 V and compared it with the envelope without buncher voltage (V_0 = 0). V_0 = 200 V is a little higher than typical buncher voltages. The result is shown in Fig. 5. The envelope of V_0 = 0 overlaps the envelope of V_0 = 200 V. This means that the beam envelope is not affected by axis-buncher if the beam intensity is less than 500 eμA and V_0 less than 200 V. Therefore, our beam trajectory calculation is valid with beam intensity of less than 500 eμA and standard buncher voltages.

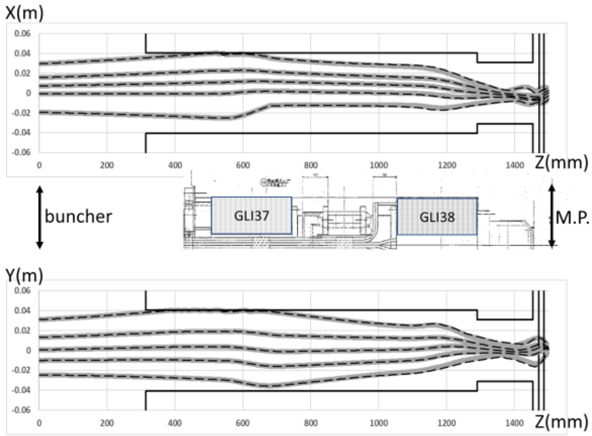

Figure 5. Same as Fig. 4, but with the buncher voltage setting of V_0 = 200 V.

References

[1] T. Hoffmann *et al.*, AIP Conf. Proc. **546**, 432 (2000).
[2] Y. Kotaka *et al.*, Proc. 14th Annual Meeting of PASJ, (2017), p.1118-1122.
[3] Y. Kotaka *et al.*, Proc. 8th IBIC2019, Malmö, Sweden (2020) p.351-354.
[4] OPAL, gitlab.psi.ch/OPAL/src/wikis/home

Development of emittance monitor for the accelerated ion beam by AVF Cyclotron

Y. Kotaka, K. Kamakura, H. Yamaguchi, N. Imai, Y. Sakemi, J. Ohnishi[a], A. Goto[a], M. Kase[a], K. Hatanaka[b], S. Shimoura

Center for Nuclear Study, Graduate School of Science, University of Tokyo
[a]RIKEN Nishina Center
[b]Research Center for Nuclear Physics, Osaka University

1. Introduction

There are 3 experiment courses performed by CNS in the E7 room of RIKEN Nishina Center shown in Fig. 1. The first one is CRIB experiment on the E7A beam course. The second is EDM experiment on the C12 beam course. The third is experiment for undergraduate students in the University of Tokyo on the E7B beam course. E7B and C12 are more and more used for RI production of RIKEN in recent years. Accordingly, requests of ion beams to AVF Cyclotron are increasing.

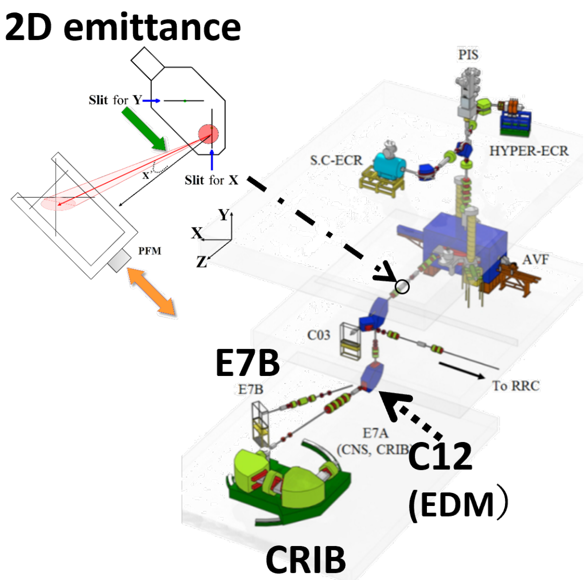

Figure 1. Experiment and beam course in E7 room. Ion beams accelerated by AVF Cyclotron are bent down to E7 room to supply for 3 experiment courses. CRIB experiment is on the E7A beam course. EDM experiment is on the C12 beam course. Undergraduate student experiment is on the E7B beam course.

2. The problem of beam transport efficiencyt

Figure 2 shows the beam transport efficiencies from AVF Cyclotron to CRIB, C12, and E7B as a function of beam intensities since 2019. At first, it is found that all of efficiencies cannot reach 1. When the beam intensity is less than 10 eμA, the average beam transport efficiency is 0.73. When the beam intensity is larger than 10 eμA, the average beam transport efficiency is 0.66. It is found that the stronger beam intensity tends to lower beam transport efficiency. We imagine that this reason is beam emittance is expanded in proportion to the beam intensity. However, we cannot understand the relation between the beam intensities and the emittance until we can measure a large amount of emittance of the strong intensity beam.

We have a plan to increase RI production yield. Increasing Francium (Fr) yield is necessary for EDM experiment. As a way of it, the intensity of ^{18}O ion beam must be more than 4 pμA and up to 25 pμA which is limited by shielding ability of building. Fr is produced by exposing 100MeV ^{18}O ion beam to Gold (Au) target and fusing ^{18}O with Au. Furthermore, the size of ^{18}O ion beam on the target is requested to be 1 mm diameter.

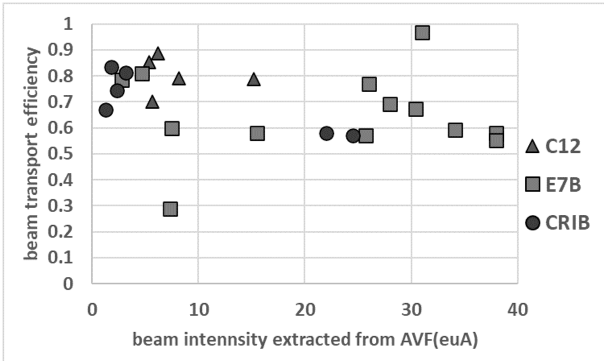

Figure 2. The beam transport efficiency from AVF Cyclotron to CRIB, C12, and E7B in relation to beam intensity.

Estimating the beam transport efficiency with Fig. 2, it would be less than 0.6 for ^{18}O ion beam at 25 pμA. In order to optimize the beam transport system for the high intensity beam, we must understand the reason of the decrease of the beam transport efficiency as a function of the beam intensity. To solve this problem, it is important to measure the strong intensity beam emittance.

3. Development of the emittance monitor for high power beam

We already have 2D emittance monitor located on the beam line at a distance of 3546 mm from the exit of AVF Cyclotron, which is shown by the circle in Fig. 1. However, this monitor cannot be useful for more than 100 or 200 W beam because the cooling power is not sufficient. Therefor, we need the emittance monitor which can be operated under high power beam and we start to develop the pepper-pot emittance monitor [1–3] for the accelerated beam of AVF Cyclotron.

Pepper-pot emittance monitor does not need cooling because the time for measurement is less than 1 sec. The measurement process is described in detail. At first, beam is stopped, and pepper-pot emittance monitor is inserted into beam center. Then, beam is exposed and the beam image on the fluorescent plate is immediately recorded by digital camera. At last, beam is stopped. By this set of processes, cooling is not thought to be necessary. The measurable high limit of beam power depends on the speed of remote-control system. About it, we will test by exposing high power beam to the pepper-pot emittance monitor.

Figure 3 shows the prototype of pepper-pot emittance monitor for high power beam. The thickness of peeper-pot mask is 1 mm. The beam energy to stop the beam is estimated from the relation between the range of charged particle and momentum [4]. The stoppable energy is less than 18 MeV for H^+, 11 MeV/u for $^2H^+$, and 16MeV/u for $^4He^{2+}$. To see the accelerated energy region of AVF Cyclotron, we have unmeasurable energy region for H^+ and $^2H^+$ but they are little. The other specifications of the prototype of the pepper-pot emittance monitor are shown Table 1.

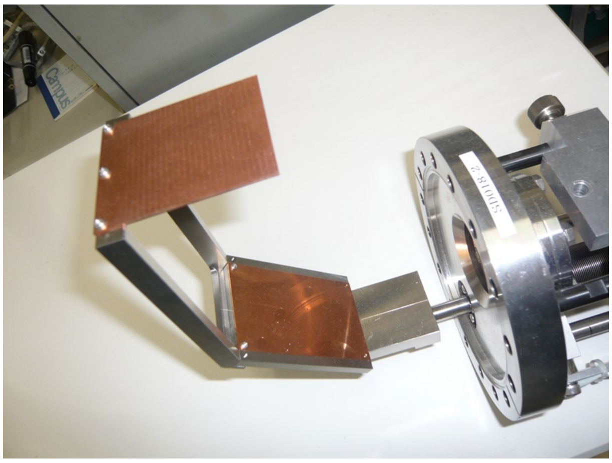

Figure 3. Prototype of the pepper-pot emittance monitor.

Table 1. specification of pepper-pot emittance monitor

Radius of hall in mask	0.3 mm
Interval of hall (horizontal: x)	2 mm
Interval of hall (vertical: y)	1 mm
Effective area of fluorescent plate	55×50 mm^2
Distance between mask and the center of fluorescent plate	100 mm
Promising position accuracy	0.1 mm
Promising Angle accuracy	2.5 mrad

In this fiscal year, we produced the prototype of pepper-pot emittance monitor for high power beam and its remote-control system. However, digital camera is easy to be damaged by radiation from ion beams. Before beam test, we decide to introduce the methods to mitigate the radiation damage of the digital camera. After we finish it, we will test the performance of the pepper-pot emittance monitor.

References

[1] T. Hoffmann *et al.*, AIP Conf. Proc. **546**, 432 (2000).

[2] Y. Kotaka *et al.*, Proc. 14th Annual Meeting of PASJ, (2017), p.1118-1122.

[3] Y. Kotaka *et al.*, Proc. 8th IBIC2019, Malmö, Sweden (2020) p.351-354.

[4] National Astronomical Observatory of Japan, Chronological Scientific Tables, Maruzen, (1990)

Current Status of Hyper ECR Ion Source

K. Kamakura, Y. Kotaka, T. Nakagawa[a], J. Ohnishi[a], A. Goto[a], M. Kase[a], K. Hatanaka[b], H. Yamaguchi, N. Imai, S. Shimoura and Y. Sakemi

Center for Nuclear Study, Graduate School of Science, the University of Tokyo
[a]*Nishina Center for Accelerator-Based Science, RIKEN*
[b]*Research Center for Nuclear Physics, Osaka University*

1. Introduction

14 GHz Hyper ECR ion source (ECRIS) was first introduced in 1989 at Institute for Nuclear Study, the University of Tokyo. In 2004, it was relocated to RIKEN Nishina Center, and has been providing various ion beams to RIKEN AVF cyclotron ever since. Over the course of past thirty years, the performance has been vastly improved. At the moment, it can be operated at high beam intensity to match the requirement of recent experiments, yet further improvement is expected to meet the requirement of higher intensity and more stable operation. In general, the beam intensity is determined by two factors; the amount of ions produced in the ECR plasma and the efficiency of beam extraction from the plasma chamber. In this report, recent research and improvements on both factors will be discussed.

2. Beam Extraction System

Extraction systems consist of several electrodes. The shapes of first two electrodes (Plasma Electrode and Ground Electrode) define the electric field distribution to extract ions from the plasma chamber. It determines not only intensity but also emittance of the extracted beam which plays a crucial role in beam transmission. Recently, beam trajectory analysis with space charge effect has been performed. As a result, a novel strong-convergence extraction system is introduced to improve the extraction efficiency (Figure 1). As a consequence, beam current of various ion species has been doubled compared to the conventional extraction system. [1]

Following the success of strong-convergence extraction system, it has been used in every injection to the AVF cyclotron since April 2020, greatly contributing to RIKEN AVF cyclotron operation. [2]

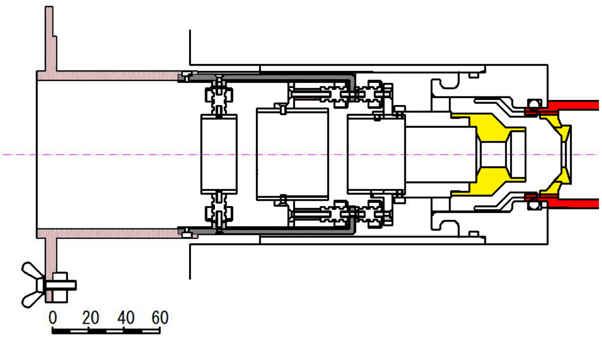

Figure 1. Cross-sectional view of the strong-convergence extraction system. Plasma Electrode forms the end of the plasma chamber on the right. Ground Electrode is located next to Plasma Electrode. A voltage of 7.5∼15 kV is applied between them.

3. ECR Plasma

Principally, a state of plasma is characterized by physical quantities such as electron density, electron temperature and confinement time of ions. Those can be controlled by various operating parameters; flow rate of main and support gasses, current induced in two mirror coils, RF power, position of RF tuner rod. Recent studies show voltage of Einzel electrode outside the plasma chamber also affects the plasma boundary and subsequently the plasma state. Observables are beam current, beam profile, emittance and visible light emitted from ECR plasma. Operating at its highest capability is a task of maximization problem with six to seven parameters. The most difficult part of operating ECRIS is that the relations between physical quantities of plasma, observables and controllables are intertwined. For example, when gas flow is increased, electron density increases, on the other hand, average electron temperature decreases. Operation of such a system always has the risk of parameters being trapped in a local maximum.

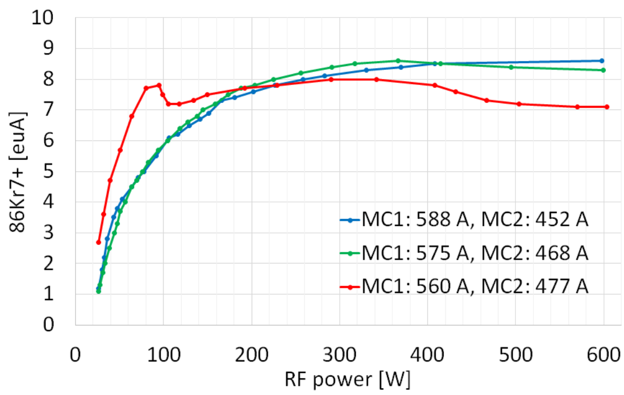

Figure 2. Beam current of $^{86}Kr^{7+}$ vs. RF power. Trends are measured with three sets of mirror coil currents. MC1 and MC2 are the current applied to upstream and downstream mirror coil, respectively. The rest of the parameters are kept the same.

Figure 2 shows RF power dependencies of $^{86}Kr^{7+}$ beam current. Under a certain condition (upstream mirror coil: 560 A, downstream mirror coil: 477 A), local maximums are located around 90 W and 300 W.

Using krypton as the ionization gas (main gas), characteristics of operating parameters for each charge state have been studied. Furthermore, various support gasses have been tested to evaluate the efficiency of mixing effect.

4. Beam Production using Solid Samples

Providing beams to AVF cyclotron using solid samples such as iron and lithium is one of the important roles of Hyper ECRIS.

4.1. Iron

The iron beam provided by Hyper ECRIS plays an important role in experiments for ion beam breeding in agricultural science. During last year, the beam intensity on target has been significantly improved due to developments of ECRIS and AVF cyclotron.

$^{56}Fe^{15+}$ beam is extracted from Hyper ECRIS and accelerated up to 5.01 MeV/u via AVF cyclotron. After going through a charge stripper, $^{56}Fe^{24+}$ beam is injected to RIKEN Ring Cyclotron (RRC). Table 1 and Figure 3 show a trend of improvement on transmissions through cyclotrons over the course of the past year. Beam current on target increased by a factor of 10.

Date	$^{56}Fe^{15+}$ [pnA]			$^{56}Fe^{24+}$ [pnA]
	IH10	I36	C01	D50
Dec. 11, 2019	140.0	106.7	14.0	0.7
Jul. 3, 2020	300.0	266.7	53.3	2.8
Sep. 16, 2020	506.7	266.7	45.3	4.0
Feb. 16, 2021	386.7	346.7	106.7	8.0

Table 1. Particle current of iron beam at Faraday cups from Hyper ECRIS to the target. IH10: Hyper ECRIS. I36: before injection to AVF. C01: after extraction from AVF. D50: before target.

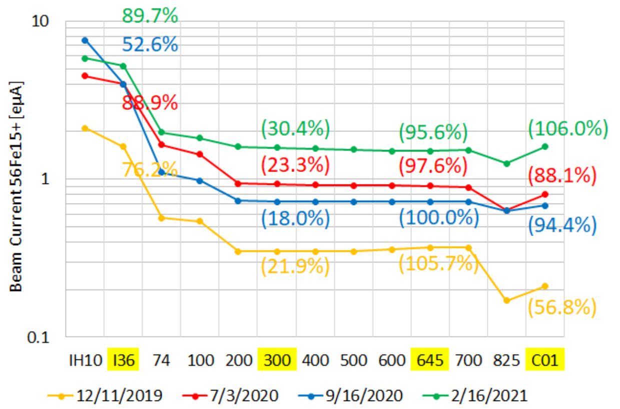

Figure 3. Beam current of $^{56}Fe^{15+}$ from low energy beam transport through AVF cyclotron to extraction. 74 to 825 indicates the radius of orbit in the AVF cyclotron in millimeters, measured by phase probe.

4.2. Lithium

Lithium-7 is used for astrophysics experiment at CNS RI beam separator (CRIB). $^{7}Li^{2+}$ and $^{7}Li^{3+}$ beams are required for different energies. Lithium sample is stored in a crucible and heated by ECR plasma. Lithium has low melting point of 180 °C. On the other hand, the boiling point is around 350∼400 °C in a vacuum of $10^{-4} \sim 10^{-5}$ Pa. When the lithium sample boils, it blows out in the plasma chamber and be lost instantly. Controlling vaporization and ionization at the same time had been a difficult task. However, recent studies made it possible to maintain the optimal condition by observing color distribution of ECR plasma through a view port (Figure 4).

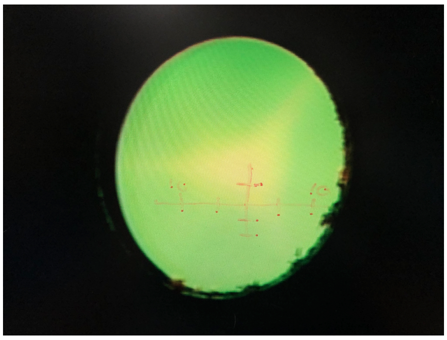

Figure 4. Image of an $^{7}Li^{2+}$ plasma observed through view port. Yellow star appears in the middle surrounded by green light. Parameters were adjusted to $^{7}Li^{2+}$ and the beam current at this time was 186 eμA (and that of $^{7}Li^{3+}$ was 110 eμA).

After extraction from the AVF cyclotron, maximum particle currents of $^{7}Li^{2+}$ and $^{7}Li^{3+}$ are improved up to 3.6 pμA and 5.2 pμA respectively. They have been doubled since 2018. [3]

References

[1] Y. Ohshiro et al., CNS Annual Report 2019, 53 (2021).
[2] K. Suda et al., Proceedings of the 18th PASJ Meeting, THSP01, 2021
[3] Y. Ohshiro et al., CNS Annual Report 2018, 51 (2020).

Theoretical Nuclear Physics

Variational approach with the superposition of the symmetry-restored quasi-particle vacua for large-scale shell-model calculations

N. Shimizu[a], Y. Tsunoda[a], Y. Utsuno[b,a], and T. Otsuka[c,d]

[a]*Center for Nuclear Study, Graduate School of Science, The University of Tokyo*
[b]*Advanced Science Research Center, Japan Atomic Energy Agency*
[c]*RIKEN Nishina Center for Accelerator-Based Science, RIKEN*
[d]*Department of Physics, The University of Tokyo*

1. Introduction

Nuclear shell model calculation is a configuration interaction method to describe any many-body correlations inside the valence shell on equal footing, and it is quite useful for the description of the ground and low-lying excited states of nuclei. However, the dimension of the shell-model Hamiltonian matrix to be diagonalized increases explosively depending on the model space and the number of the active particles, and thus it hampers the application of shell-model calculations to the medium-heavy nuclei severely.

In order to overcome this difficulty, a lot of efforts have been paid to develop various theoretical frameworks to obtain shell-model solutions where the conventional Lanczos diagonalization method cannot reach. Among them, the Monte Carlo shell model (MCSM) is one of the most successful schemes and has been applied to various mass regions [1]. The MCSM wave function is expressed as a linear combination of the angular-momentum and parity projected Slater determinants, which are determined by the variational and stochastic ways to minimize the projected energy. However, in the study of medium-heavy nuclei where the density of single-particle states per energy increases and the pairing correlation becomes important, a large number of the Slater determinants for the MCSM wave function are required in principle to describe pair-correlated many-body wave functions, which often makes the precise estimation of exact shell-model physical quantities difficult.

In the present report, we introduce quasi-particle vacua as a replacement of Slater determinants of the MCSM to study medium-heavy nuclei by treating pairing correlations efficiently. We perform the variational calculation to minimize the energy after the angular-momentum, parity, and number projections and superposition. We call this scheme the quasi-particle vacua shell model (QVSM). This report is condensed from Ref. [2].

2. Theoretical Framework

In the QVSM, the variational wave function is defined as a superposition of the angular-momentum, parity, and number projected quasi-particle vacua:

$$|\Psi_{N_b}\rangle = \sum_{n=1}^{N_b} \sum_{K=-J}^{J} f_{nK}^{(N_b)} P_{MK}^{J\pi} P^Z |\phi_n^{(\pi)}\rangle \otimes P^N |\phi_n^{(\nu)}\rangle \qquad (1)$$

where the $P_{MK}^{J\pi}$, P^Z, and P^N are the angular-momentum and parity projector, the proton number projector, and the neutron number projector, respectively. $|\phi_n^{(\pi)}\rangle$ ($|\phi_n^{(\nu)}\rangle$) denotes the quasi-particle vacuum of protons (neutrons). N_b is the number of the basis states, or the projected quasi-particle vacua. f_{nK} is a coefficient of the linear combination of the basis states and determined by solving the generalized eigenvalue problem of the $(2J+1)N_b \times (2J+1)N_b$ Hamiltonian and norm matrices in the subspace spanned by the projected basis states.

The quasi-particle vacuum $|\phi_n\rangle$ is parametrized by complex matrices $U_{ij}^{(n)}$ and $V_{ij}^{(n)}$ as

$$\begin{aligned} \beta_k^{(n)}|\phi_n\rangle &= 0 \quad \text{for any } k \\ \beta_k^{(n)} &= \sum_i (V_{ik}^{(n)*} c_i^\dagger + U_{ik}^{(n)*} c_i) \end{aligned} \qquad (2)$$

where β_k denotes a quasi-particle annihilation operator and $c_i^\dagger$ is the creation operator of the single-particle orbit i. Note that we do not assume any symmetry for this state except that proton-neutron pair is not considered for quasi particles.

As N_b increases from 1, the variational parameters $U^{(N_b)}$ and $V^{(N_b)}$ are determined at every N_b so that the energy expectation value, $E_{N_b} = \langle\Psi_{N_b}|H|\Psi_{N_b}\rangle$, is minimized using the conjugate gradient method iteratively. Obeying the variational principle, E_{N_b} is the variational upper limit for the exact shell-model energy, and E_{N_b} decreases gradually as N_b is increased. We increase N_b till E_{N_b} converges.

3. Benchmark Test

We perform the benchmark test of the QVSM taking ^{132}Ba with the SN100PN interaction [3] as an example. The model space is taken as the $50 < N,Z < 82$ valence shell, which consists of the $0g_{7/2}$, $1d_{5/2}$, $1d_{3/2}$, $2s_{1/2}$, and $0h_{11/2}$ orbits with the ^{100}Sn inert core. Although its M-scheme dimension is huge, 2.0×10^{10}, it is tractable by the conventional Lanczos diagonalization method [4].

Figure 1(a) shows the QVSM energy as a function of the number of the basis states N_b, which is defined in Eq. (1). As N_b increases the QVSM energy decreases gradually and approaches the exact values, which are shown as the horizontal dotted lines.

For comparison, the solid black lines in Fig. 1(a) show the MCSM energy expectation values as a function of the number of the basis states, N_b. Since Slater determinants cannot describe pairing correlations efficiently, the MCSM energy converges rather slowly in comparison with the QVSM. Even at $N_b = 1$, the QVSM energy is closer to the exact one than those of the MCSM.

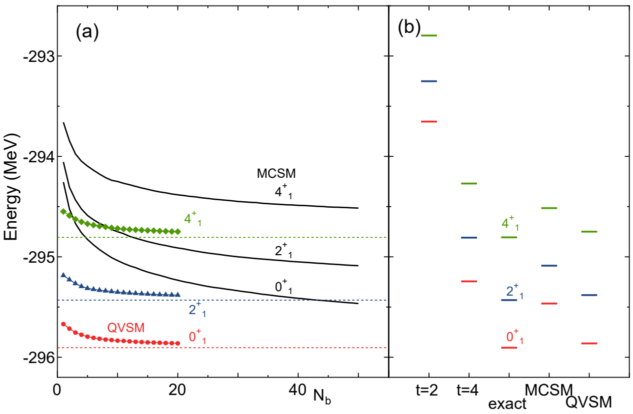

Figure 1. (a) Energy expectation values E_{N_b} of the 0_1^+ (red), 2_1^+ (blue), 4_1^+ (green) states of ^{132}Ba by the QVSM and the MCSM as a function of the number of the basis states N_b. The horizontal dotted lines show the exact shell-model energies. (b) The 0_1^+, 2_1^+, 4_1^+ energies of ^{132}Ba obtained by the conventional Lanczos method with $t=2$ truncation, by that with $t=4$ truncation, by the exact calculation without truncation, by the MCSM with 50 basis states, and by the QVSM with 20 basis states are shown from left to right.

Figure 1 (b) shows the energies obtained by the QVSM, the MCSM, and the Lanczos diagonalization method in truncated spaces. The diagonalization was performed in the truncated space restricting up to t-particle t-hole excitations across the $Z = N = 64$ shell gap from the filling configuration. The truncation scheme is taken as $t = 2$ (2.3×10^8 M-scheme dimension), $t = 4$ (3.4×10^9 M-scheme dimension), and the full space without truncation for the exact energy. The $t = 2$ ($t = 4$) energy is 2.3 MeV (0.7 MeV) higher than the exact one. The rightmost part of Fig. 1 (b) shows the results of the MCSM with $N_b = 50$ and the QVSM with $N_b = 20$. The MCSM result overcomes the truncated results, but it is still 440 keV higher than the exact one. The QVSM agrees with the exact one quite well within 50 keV. This small gap between the QVSM and exact ones can be filled by the energy-variance extrapolation method [2]. While the MCSM underestimates the excitation energies 100 keV, the QVSM excitation energies agree with the exact ones quite well.

While the QVSM converges as a function of N_b faster than the MCSM, the computational cost of the QVSM with the same N_b is heavier than that of the MCSM because of the necessity of the number projection. In practice, the total computational of the QVSM whose result is shown in Fig. 1 is about 10 times heavier than that of the MCSM. Even considering such difference, the QVSM is more efficient than the MCSM in the ^{132}Ba case since the QVSM energy with $N_b = 1$ is already lower than the MCSM energy with $N_b = 50$.

4. Summary

We have developed a variational method after the superposition of the fully projected quasi-particle vacua, named the QVSM for shell-model studies of medium-heavy nuclei. In Ref. [2], the capability of the QVSM to obtain other physical quantities such as the quadrupole moment and $B(E2)$ transition were discussed. In addition, we can introduce the energy-variance extrapolation to the QVSM framework to overcome the variational limit in the same way as the MCSM framework [5]. This extrapolation method enables us to estimate the energy eigenvalue precisely [2]. Since the QVSM wave function describes the pairing correlations efficiently, it is expected to be useful especially in heavy-mass nuclei. This proof-of-the-principle study opens a way to investigate the medium-heavy nuclei with configuration mixing utilizing nuclear shell-model calculations.

Acknowledgements

This research used computational resources of the supercomputer Fugaku (hp200130), and the Oakforest-PACS supercomputer (hp200130, hp190160, hp180179, hp170230, hp160211, xg18i035). The authors acknowledge valuable supports by “Priority Issue on post-K computer” and “Program for Promoting Researches on the Supercomputer Fugaku”, MEXT, Japan.

References

[1] N. Shimizu, T. Abe, M. Honma, T. Otsuka, T. Togashi, Y. Tsunoda, Y. Utsuno, and T. Yoshida, Phys. Scr. **92**, 063001 (2017); N. Shimizu, T. Abe, M. Honma, T. Otsuka, T. Togashi, Y. Tsunoda, Y. Utsuno, and T. Yoshida, Phys. Scr. **92**, 063001 (2017).

[2] N. Shimizu, Y. Tsunoda, Y. Utsuno, and T. Otsuka, Phys. Rev. C **103**, 014312 (2021).

[3] B. A. Brown, N. J. Stone, J. R. Stone, I. S. Towner, and M. Hjorth-Jensen, Phys. Rev. C **71**, 044317 (2005).

[4] N. Shimizu, T. Mizusaki, Y. Utsuno, and Y. Tsunoda, Comp. Phys. Comm. **244**, 372 (2019).

[5] N. Shimizu, Y. Utsuno, T. Mizusaki, T. Otsuka, T. Abe, and M. Honma, Phys. Rev. C **82**, 061305(R) (2010); N. Shimizu, Y. Utsuno, T. Mizusaki, M. Honma, Y. Tsunoda, and T. Otsuka, Phys. Rev. C **85**, 054301 (2012).

Triaxial rigidity of ^{166}Er and its Bohr-model realization

Y. Tsunoda[a] and T. Otsuka[b,c]

[a] *Center for Nuclear Study, the University of Tokyo*
[b] *Department of Physics, the University of Tokyo*
[c] *RIKEN Nishina Center*

Low-lying states of deformed nuclei are one of the most important properties of the nuclear structure. Many even-even nuclei are considered to be a prolate shape and have a ground-state rotational band of spin $J = 0,2,4,\ldots$ states. There is also another low-lying band of $J = 2,3,4,\ldots$ states. This band is conventionally considered to be a γ-vibrational band, where axially asymmetric vibration and rotation of a purely prolate nucleus are combined, and many nuclei have been described in this picture [1]. A triaxially deformed nucleus near prolate shape also has low-lying rotational bands of $J = 0,2,4,\ldots$ states and of $J = 2,3,4,\ldots$ states. Whether these bands come from γ-vibration or triaxiality has been discussed, e.g., in a review paper of experimental data [2]. Our recent paper [3] shows results of the Monte Carlo shell model (MCSM) calculations of the triaxially deformed ^{166}Er nucleus. We discuss triaxiality of ^{166}Er by using a simple model of the Bohr Hamiltonian [4, 5], which describes quadrupole deformations of a nucleus. This report is based on Ref. [6].

The Bohr Hamiltonian has 5 degrees of freedom of quadrupole deformations. They are represented as a magnitude of deformation β_2, a triaxiality of deformation γ, and Euler angles θ_i ($i = 1,2,3$) of rotation of a deformed nucleus. $\gamma = 0^\circ (60^\circ)$ corresponds to a prolate (oblate) shape and $0^\circ < \gamma < 60^\circ$ implies a triaxial shape. The Bohr Hamiltonian is written as

$$H_B = -\frac{\hbar^2}{2B}\Big[\frac{1}{\beta_2^4}\frac{\partial}{\partial\beta_2}\beta_2^4\frac{\partial}{\partial\beta_2} + \frac{1}{\beta_2^2\sin 3\gamma}\frac{\partial}{\partial\gamma}\sin 3\gamma\frac{\partial}{\partial\gamma} - \frac{1}{4\beta_2^2}\sum_\kappa \frac{Q_\kappa^2}{\sin^2(\gamma - \frac{2}{3}\pi\kappa)}\Big] + V(\beta_2,\gamma),$$

where B is a parameter, Q_κ ($\kappa = 1,2,3$) imply angular momentum operators in the body-fixed frame, and $V(\beta_2,\gamma)$ denotes the potential. The Schrödinger equation is written as

$$H_B\Psi(\beta_2,\gamma,\theta_i) = E\Psi(\beta_2,\gamma,\theta_i),$$

where E is the energy eigenvalue. For simplicity of calculation, we assume that β_2 is a constant. With this assumption, the above Schrödinger equation is reduced to

$$\frac{\hbar^2}{2B\beta_2}\Big[-\frac{1}{\sin 3\gamma}\frac{\partial}{\partial\gamma}\sin 3\gamma\frac{\partial}{\partial\gamma} + \frac{1}{4}\sum_\kappa \frac{Q_\kappa^2}{\sin^2(\gamma - \frac{2}{3}\pi\kappa)} + V_\gamma(\gamma)\Big]\Phi(\gamma,\theta_i) = E\Phi(\gamma,\theta_i),$$

where $V_\gamma(\gamma)$ is an appropriate potential. The wave function is represented as

$$\Phi(\gamma,\theta_i) = \sum_K g_K^I(\gamma) D_{MK}^I(\theta_i),$$

where I is the angular momentum of the eigensolution in the laboratory frame, $D_{MK}^I(\theta_i)$ means the Wigner D function, and $g_K^I(\gamma)$ is the K-component of the wave function. K corresponds to the z projection of the angular momentum in the body-fixed frame. K is even integer with $|K| \le I$ and $g_K^I(\gamma) = (-)^I g_{-K}^I(\gamma)$. The E2 transition operator is given, in the lowest order, by

$$T(E2) = t\beta_2\Big[D_{\mu,0}^{(2)}\cos\gamma + \frac{1}{\sqrt{2}}(D_{\mu,2}^{(2)} + D_{\mu,-2}^{(2)})\sin\gamma\Big],$$

where t is a parameter.

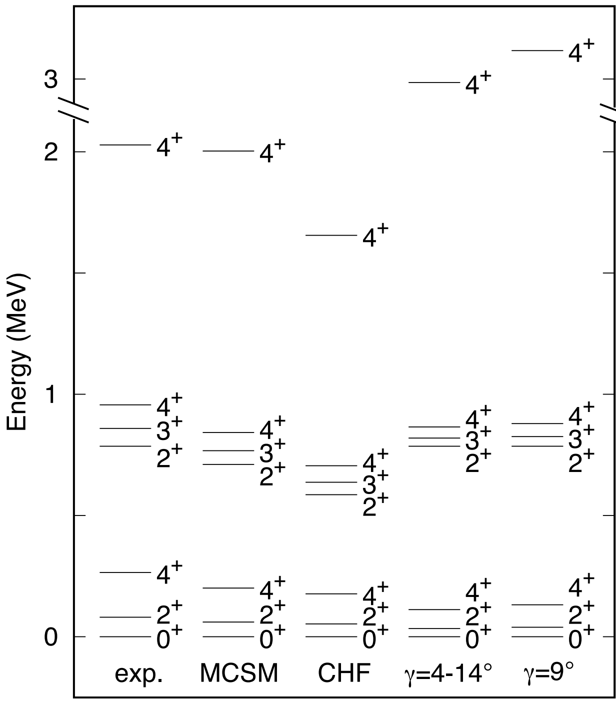

Figure 1. Energy levels of ^{166}Er nucleus. Experimental values (exp.) [7] are compared to various calculations by Monte Carlo shell model (MCSM) [3], constrained Hartree-Fock with the angular-momentum and parity projections after variation (CHF), Bohr Hamiltonian with the square-well potential (γ=4–14°) and rigid triaxial model (γ=9°). Taken from Ref. [6].

Figure 1 shows low-lying levels of ^{166}Er nucleus. The MCSM calculations reproduce experimental values well. The analysis using T-plot shows that the MCSM wave functions contain components of γ=4–14° [3]. The constrained Hartree-Fock calculations with the angular-momentum and parity projections after variation with $\beta_2 = 0.29$ and $\gamma = 9^\circ$

show similar results with lower energies. We use a square-well potential of γ=4–14° with virtually infinite depth for $V_\gamma(\gamma)$ of the Bohr Hamiltonian. The parameter B of the Bohr Hamiltonian is fitted so as to reproduce the observed excitation energy of the 2_2^+ state. Results of the Bohr Hamiltonian calculations show the higher 4_3^+ level and other levels are reproduced. The rigid triaxial model with $\gamma = 9°$ shows similar results to the Bohr Hamiltonian calculations.

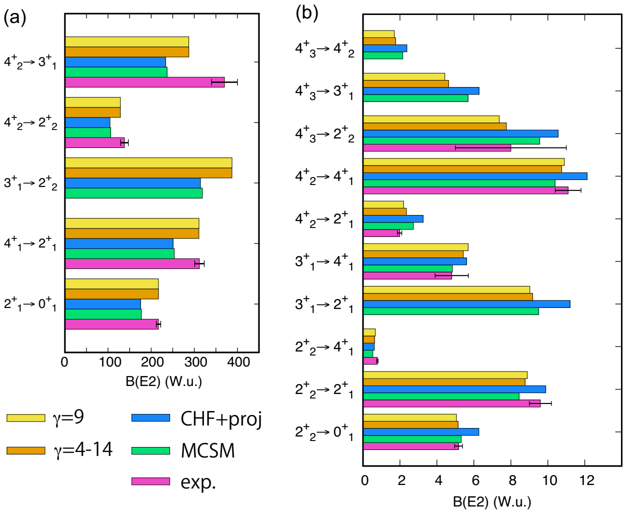

Figure 2. $B(E2)$ values between low-lying states in ^{166}Er nucleus. Experimental values (exp.) are included [7]. Theoretical calculations are labelled similarly to Fig. 1. Taken from Ref. [6].

Figure 2 shows $B(E2)$ values between low-lying states in ^{166}Er nucleus. Large values of intraband transition and small values of interband transition are shown separately. We fit the value of t in the E2 transition operator of the Bohr Hamiltonian so as to reproduce the observed $B(E2; 2_1^+ \to 0_1^+)$ value. All four theoretical calculations show similar results and reproduce experimental values well.

Figure 3 shows $g_K^I(\gamma)$ functions of the Bohr Hamiltonian calculations. Although the K quantum number is mixed generally for $\gamma \neq 0$, the mixing is weak with the present square-well potential. All non-zero $g_K^I(\gamma)$ functions show similar shapes. This means that the nucleus is deformed similarly and rotates with different J and K values in all calculated low-lying states. Thus, the calculations of the Bohr Hamiltonian with square-well potential show low-lying states of the rotation of triaxially deformed ^{166}Er nucleus and reproduce experimental values.

This work was supported in part by MEXT as "Program for Promoting Researches on the Supercomputer Fugaku" (Simulation for basic science: from fundamental laws of particles to creation of nuclei) (hp200130) and by JICFuS.

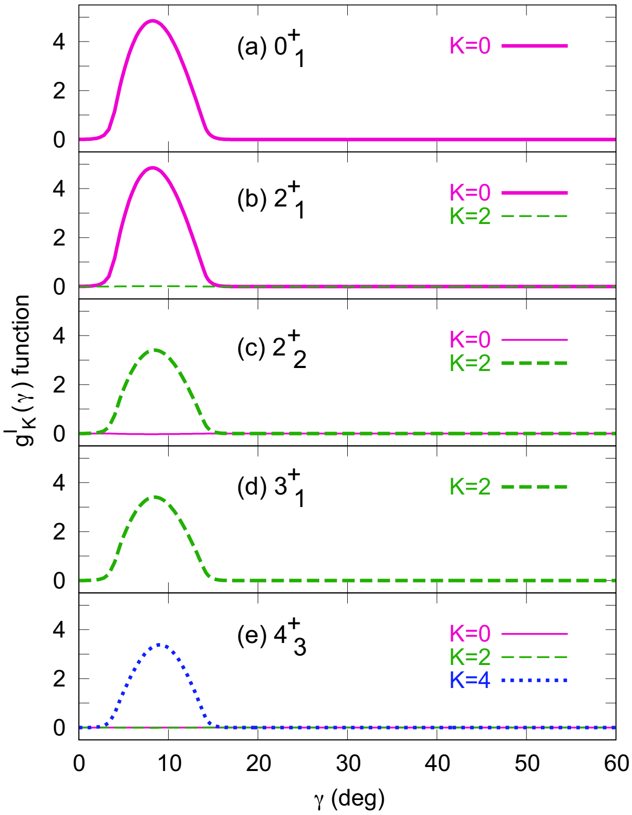

Figure 3. $g_K^I(\gamma)$ functions of various states of ^{166}Er in the Bohr model for (a) 0_1^+, (b) 2_1^+, (c) 2_2^+, (d) 3_1^+, and (e) 4_3^+ states, respectively. The $K^P = 0^+, 2^+$ and 4^+ functions are shown by pink solid, green dashed and blue dotted lines, respectively. Taken from Ref. [6].

References

[1] A. Bohr and B. R. Mottelson, *Nuclear Structure* (Benjamin, New York, 1975), Vol. II.

[2] J. F. Sharpey-Schafer, R. A. Bark, S. P. Bvumbi, T. R. S. Dinoko, and S. N. T. Majola, Eur. Phys. J. A **55**, 15 (2019).

[3] T. Otsuka, Y. Tsunoda, T. Abe, N. Shimizu, and P. Van Duppen, Phys. Rev. Lett. **123**, 222502 (2019).

[4] A. Bohr, Mat. Fys. Medd. K. Dan. Vid. Selsk. **26**, 14 (1952).

[5] A. Bohr and B. R. Mottelson, Mat. Fys. Medd. K. Dan. Vid. Selsk. **27**, 16 (1953).

[6] Y. Tsunoda and T. Otsuka, Phys. Rev. C **103**, L021303 (2021).

[7] National Nuclear Data Center, Evaluated Nuclear Structure Data File, https://www.nndc.bnl.gov/ensdf/.

Screening of nucleon electric dipole moments in atomic systems

K. Yanase

Center for Nuclear Study, Graduate School of Science, The University of Tokyo

The observation of a permanent electric dipole moment (EDM) of an atom implies the presence of parity (P) and time-reversal (T) violating interactions between constituent particles. The atomic EDM is defined by

$$\boldsymbol{d}_{\rm atom} = -\sum_{i=1}^{Z} e\boldsymbol{r}'_i, \tag{1}$$

where e is the elementary charge and $\boldsymbol{r}'_i$ indicates the coordinates of the atomic electrons. The interaction of the atomic EDM with an external electric field causes an energy shift to be measured.

In principle, the nuclear EDM $\boldsymbol{d}_{\rm nucl}$ and the EDMs of electrons $\boldsymbol{d}_i^{(e)}$ and nucleons $\boldsymbol{d}_a$ are independently coupled to the external electric field $\boldsymbol{E}_{\rm ext}$ as

$$V_{\rm ext} = -\left[\boldsymbol{d}_{\rm atom} + \boldsymbol{d}_{\rm nucl} + \sum_{i=1}^{Z} \boldsymbol{d}_i^{(e)} + \sum_{a=1}^{A} \boldsymbol{d}_a\right]\cdot \boldsymbol{E}_{\rm ext}. \tag{2}$$

According to the Schiff's theorem [1], the energy shift due to the EDM of a point-like nucleus is canceled by the contribution from the atomic EDM induced by the internal interaction of the nuclear EDM with the electrons. However, the P, T-odd meson-exchange NN interactions and the nucleon EDM allow a finite-size nucleus to have the nuclear Schiff moment (NSM) as well as the nuclear EDM. Since the atomic EDM induced by the NSM survives the screening, the atomic EDMs particularly of diamagnetic atoms are sensitive to those P, T-odd interactions.

In Ref. [2], I revisited the screening theory that involves the nucleon EDM and suggested the importance of the next-to-leading order contribution to the NSM. I briefly present the results in this report.

The screening of nucleon EDMs themselves in a finite-size nucleus causes the well-known form of the NSM. Using a numerical evaluation of this leading-order contribution, a recent measurement of the ^{199}Hg atomic EDM has provided the constraint on the neutron EDM [3]. The next-to-leading order contribution stems from the screening of the nuclear EDM induced by the internal interaction of the nucleon EDMs.

The atomic EDM induced from the NSM gives rise to the energy shift

$$\Delta E = \sum_m \frac{1}{E^{(e)}_{\rm g.s.} - E^{(e)}_m}\left\langle \psi^{(e)}_{\rm g.s.}\right| -\boldsymbol{d}_{\rm atom}\cdot\boldsymbol{E}_{\rm ext}\left|\psi^{(e)}_m\right\rangle \times \left\langle \psi^{(e)}_m\right| V_{\rm NSM}\left|\psi^{(e)}_{\rm g.s.}\right\rangle + c.c., \tag{3}$$

where $\left|\psi^{(e)}_{\rm g.s.}\right\rangle$ and $\left|\psi^{(e)}_m\right\rangle$ represent the ground state and the excited states of the electron system, respectively. The interaction of the NSM with the atomic electrons is of the form:

$$V_{\rm NSM} = -4\pi\langle \boldsymbol{S}\rangle\cdot\nabla\delta(\boldsymbol{r}), \tag{4}$$

where the NSM $\boldsymbol{S} = S\boldsymbol{I}/I$ for spin-I nuclei. The NSM depends on the nucleon EDMs d_N and the P, T-odd pion-exchange coupling constants $\bar{g}_T$ as

$$S = S_2 + S_3, \tag{5}$$

$$S_2 = \sum_{N=n,p} s_N d_N, \tag{6}$$

$$S_3 = \sum_{N=n,p} a_N d_N + \sum_{T=0,1,2} a_T \bar{g}_T. \tag{7}$$

where the existence of the first term in the third-order contribution (7) was suggested in Ref. [2].

The external interaction of the nucleon EDMs, the last term in Eq. (2), is obscured by the internal interaction of the nucleon EDMs with the atomic electrons. Consequently, the atomic EDM induced by the NSM as illustrated in Fig. 1 can be measured. The second-order contribution of the nucleon EDM to the NSM is given by

$$\langle \boldsymbol{S}_2\rangle = \left\langle \psi^{(N)}_{\rm g.s.}\right|\boldsymbol{S}_2\left|\psi^{(N)}_{\rm g.s.}\right\rangle, \tag{8}$$

where

$$S_{2,k} = \frac{1}{6}\sum_{a=1}^{A} d_{a,k}\left(r_a^2 - \langle r^2\rangle_{\rm ch}\right) + \frac{2}{15}\sum_{a=1}^{A} d_{a,j}\left(Q_{a,jk} - \langle Q_{jk}\rangle_{\rm ch}\right), \tag{9}$$

and $\left|\psi^{(N)}_{\rm g.s.}\right\rangle$ represents the nuclear ground state.

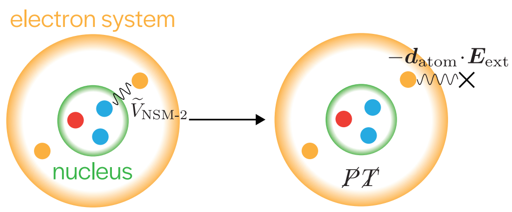

Figure 1. Schematic illustration of the leading order contribution of the nucleon EDMs to the atomic EDM $\boldsymbol{d}_{\rm atom}$.

The nuclear EDM induced by the nucleon EDM is screened by the interaction of the nucleon EDMs with the protons. The third-order contribution illustrated in Fig. 2 is given by

$$\langle \boldsymbol{S}_3\rangle = \sum_n \frac{1}{E^{(N)}_{\rm g.s.} - E^{(N)}_n} \times \left\langle \psi^{(N)}_{\rm g.s.}\right|\boldsymbol{S}_3\left|\psi^{(N)}_n\right\rangle\left\langle \psi^{(N)}_n\right|\widetilde{V}^{(NN)}\left|\psi^{(N)}_{\rm g.s.}\right\rangle + c.c. \tag{10}$$

where $\widetilde{V}_{NN}$ represents the P, T-odd meson-exchange NN interaction and the interaction between the nucleon EDM and the protons. The NSM operator is defined by

$$S_{3,k} = \frac{e}{10}\sum_{a=1}^{Z}\left[r_a^2 r_{a,k} - \frac{5}{3} r_{a,k}\left\langle r^2\right\rangle_{\text{ch}} - \frac{4}{3} r_{a,j}\left\langle Q_{jk}\right\rangle_{\text{ch}}\right], \tag{11}$$

where $\left\langle r^2\right\rangle_{\text{ch}}$ and $\left\langle Q_{jk}\right\rangle_{\text{ch}}$ denote the charge mean squared of radius and the charge mean value of the quadrupole moment.

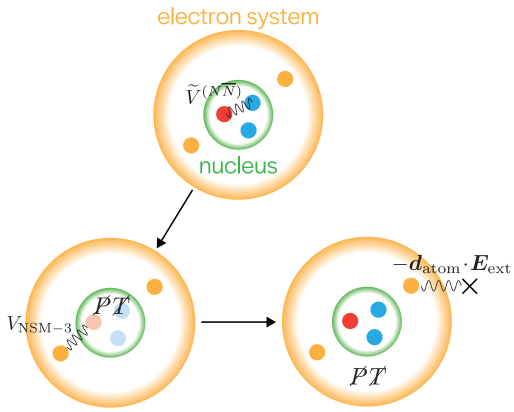

Figure 2. The next-to-leading order contribution to the Schiff moment from the nucleon EDM.

Using the independent particle model (IPM) [4], one obtains $S_2\left({}^{199}\text{Hg}\right) = 2.8 d_n\left(\text{fm}^2\right)$ and the correction S_3 is of the order of 5%. Here, the next-to-leading order contribution S_3 would be enhanced by orders of magnitude thanks to octupole correlations and the parity doubling of the ground states. The dependence of the Schiff moment on the nucleon EDM may then be dominated by S_3 rather than S_2 for actinide nuclei.

References

[1] L. I. Schiff, Phys. Rev. **132**, 2194 (1963).
[2] K. Yanase, Phys. Rev. C **103**, 035501 (2021).
[3] B. Graner, Y. Chen, E. G. Lindahl, and B. R. Heckel, Phys. Rev. Lett. **116**, 161601 (2016).
[4] K. Yanase and N. Shimizu, Phys. Rev. C **102**, 065502 (2020).

Other Activities

The 19th CNS International Summer School CNSSS20

N. Aoi[a], T. Gunji, N. Imai, H. Liang[b,c], S. Michimasa, H. Nagahama, S. Ota, T. Otsuka[b], H. Sakai[b], Y. Sakemi, H. Sakurai[b,c], N. Shimizu, S. Shimoura, H. Ueno[b], T. Uesaka[b], Y. Utsuno[d], K. Yako, H. Yamaguchi, K. Yoneda

Center for Nuclear Study, Graduate School of Science, University of Tokyo
[a]*RCNP, Osaka University*
[b]*RIKEN Nishina Center*
[c]*Department of Physics, Univ. of Tokyo*
[d]*Advanced Science Research Center, Japan Atomic Energy Agency*

The 19th CNS International Summer School (CNSSS20) was hosted by Center for Nuclear Study (CNS) from 17th to 21st in August, 2020. The school was co-organized by JSPS A3-Foresight program and supported by RIKEN Nishina Center and Asian Nuclear Physics Association (ANPhA).

Though we were aiming to hold the school in the countryside of Tokyo, due to the COVID-19 pandemic, we decided to hold the school only on-line for the first time.

The summer school was the nineteenth one in the series which aimed at fostering graduate students and postdocs by providing basic knowledge and perspectives of nuclear physics. It consisted of lectures by leading scientists in the fields of both experimental and theoretical nuclear physics. Each lecture started with an introductory talk from the fundamental point of view and ended with up-to-date topics in the relevant field.

The list of the lecturers and the title of lectures are following:

- Prof. Or Hen (MIT, USA), “Nuclear correlation via electron beams”
- Prof. Hiroari Miyatake (WNSC, KEK, Japan), “Energy-dissipated nuclear reactions”
- Prof. Kazuyuki Ogata (RCNP, Osaka University, Japan), “Knockout-reaction with RIB”
- Prof. Kazuyuki Sekizawa (Niigata University. Japan), “Time-Dependent Microscopic Approaches for Nuclear Dynamics: From Nuclei to Neutron Stars”
- Dr. Tetsuya Sato (JAEA, Japan), “Nuclear Chemistry of super heavy elements”
- Dr. Thomas Chillery (Univ. of Edinburgh, UK), “Nuclear astrophysics at LUNA”
- Dr. Sarah Naimi (RIKEN, Japan), “Overview of RIBF”

At the classes by Prof. Ogata, the lectures were given including the exercises with the knock-out reaction code which he developed. Participants tried to perform the calculation by themselves to deepen their understanding.

Seven lecturers and 193 participants registered at the school. This is the largest number of registrants ever. Because the school was held on-line, participants joined not only from Japan, Korea, China and Vietnam but also from India, Malaysia, south Africa. The time of each class was 50 minutes. There was 10 minutes break between the classes. The actual average number of participants is around 100. Figure 1 is a group photo of all the participants with the lecturers.

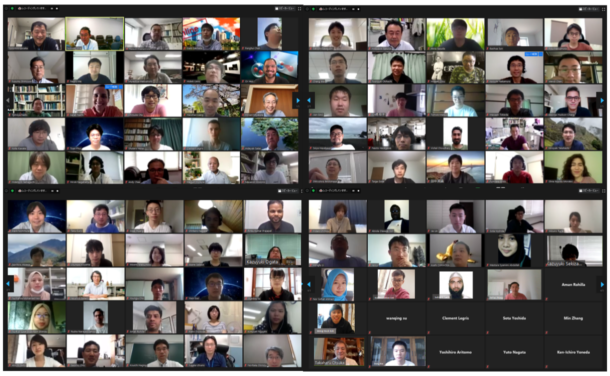

Figure 1. A group photos of the participants of CNSSS20 with the lecturers.

As traditional, there were four “Young Scientist Sessions”, where oral and poster presentations were given by graduate students and postdocs. There were twenty-one oral presentations and nine poster presentations. Since 2017, we have the CNSSS young scientist awards (CNSSSYS awards) for the good presentations. A few winners were selected from each young scientist session by the members of organizing committee and the lecturers. The winners of the second CNSSSYS award were;

- Dr. Junki Tanaka (RIKEN Nishina Center, Japan), “Probing surface alpha clustering in the ground state of stable heavy nuclei”
- Mr. Tri Toan Phuc Nguyen (University of Science, Vietnum), “Analysis of (p,pN) reactions with light nuclei in inverse kinematics”
- Mr. Masaaki Tokieda (Tohoku Univ., Japan), “Phenomenological modeling of energy dissipation in near-barrier fusion reactions”
- Ms. Atumi Saito (Titech, Japan) “Coulomb and Nuclear breakup of ^{6}He”
- Mr. Siwei Huang (RIKEN Nishina Center/Peking Univ.), “Experimental study of 4n with ^{8}He(p,2p) reaction”
- Mr. Tomoya Naito (Univ. of Tokyo/Riken), “Effects of nucleon electric form factors to nuclear binding en-

ergy"

- Mr. Yixin Guo (Univ. of Tokyo), "Non-relativistic expansion: A potential bridge to connect the relativistic and non-relativistic density functional theories"

The certificate of the awards were presented to them from the school master, Prof. Shimoura.

The best presenter among them, Mr. Masaaki Tokieda, was also awarded the APPS-DNP/ANPhA prize for young physicist, which was sponsered by AAPPS-DNP/ANPhA. He received the certificate as well as the prize money as prestend from Prof. W. Liu, the chair of ANPhA.

We are grateful to supports from ANPhA. We thank administration staffs of the CNS for their helpful supports. We also thank graduate students and postdocs in the CNS for their dedicated efforts. Finally we acknowledge all the lecturers and participants for their contributions to the CNSSS20.

Laboratory Exercise for Undergraduate Students

S. Ota, M. Niikura[a], S. Nagase,, R. Mizuno[a], K. Yako, M. Michimasa, N. Imai, H. Yamaguchi, S. H. Sakurai[a,b] and S. Shimoura

Center for Nuclear Study, Graduate School of Science, University of Tokyo
[a]*Department of Physics, University of Tokyo*
[b] *RIKEN Nishina Center*

Nuclear scattering experiments were performed as a laboratory exercise for undergraduate students of the University of Tokyo. This program was aiming at providing undergraduate students with an opportunity to learn how to study subatomic physics by using an ion beam from an accelerator. In 2020, 32 students attended this program.

The four beam times were scheduled in the second semester for third-year students, and 8 students participated in each beam time. The experiments were performed at the RIBF using a 26-MeV alpha beam accelerated by the AVF cyclotron. The alpha beam extracted from the AVF cyclotron was transported to the E7B beam line in the E7 experimental hall. The scattering chamber has two separate target ports which enable us to perform two independent experiments without opening the chamber during the beam time. In each beam time, the students were divided into two groups and took one of the following two subjects:

1. Measurement of elastic scattering of incident alpha particle with ^{197}Au, to learn how to determine nuclear size.

2. Measurement of gamma rays emitted from the cascade decay of highly excited ^{154}Gd and ^{184}Os, to learn the nuclear deformation.

Before the experiment, the students took a course on the basic handling of the semiconductor detectors and electronic circuits at the Hongo campus, and attended a radiation safety lecture at RIKEN. They also joined a tour to the RI beam factory at RIKEN.

In this year, due to the situation of COVID-19, we had to limit the number of participants. One group for the measurement of the elastic scattering came to RIKEN for the preparation on the first day and performed the measurement remotely from the hongo campus with the help of the local teacher and its assistant on the second day. The other group for the measurement of gamma rays had a remote lecture of the experiment preparation and came RIKEN to perform the experiment onsite.

In the α+^{197}Au measurement, α particles scattered with the Au target with a thickness of 1 μm were detected using a silicon PIN-diode located 15-cm away from the target. A collimator with a diameter of 6 mm was attached on the silicon detector. The energy spectrum of the scattered α particles was recorded by a multi-channel analyzer (MCA) system. The beam was stopped by a Faraday cup located downstream of the scattering chamber. The cross section for the alpha elastic scattering was measured in the angular range of $\theta_{\text{lab}} = 20-150^{\circ}$.

The measured cross section was compared with the calculated cross section of the Rutherford scattering. The cross section was also analyzed by the potential model calculation, and the radius of the ^{197}Au nucleus was discussed. Some students obtained the radius of $\sim$10 fm by using a classical model where the trajectory of the α particle in the nuclear potential is obtained using the Runge-Kutta method. Others tried to understand the scattering process by calculating the angular distribution using the distorted wave Born approximation method with a Coulomb wave function and a realistic nuclear potential.

In the measurement of gamma rays, excited states in ^{154}Gd and ^{184}Os nuclei were populated by the ^{152}Sm(α,2n) and ^{182}W(α,2n) reactions, respectively. The gamma rays emitted from the cascade decay of the rotational bands were measured by a high-purity germanium detector located 30-cm away from the target. The energy of the gamma ray were recorded by the MCA system. The gain and the efficiency of the detector system had been calibrated using standard gamma-ray sources of ^{22}Na, ^{60}Co, ^{133}Ba, and ^{137}Cs. The gamma rays from the 10^+ and 8^+ states in ^{154}Gd and ^{184}Os, respectively, were successfully identified. Based on the energies of the gamma rays, the moment of inertia and the deformation parameters of the excited states were discussed by using a classical rigid rotor model and a irrotational fluid model. The students found that the reality lies between the two extreme models. The initial population among the levels in the rotational band was also discussed by taking the effect of the internal conversion into account.

It was the first time for most of the students to use large experimental equipments. They learned basic things about the experimental nuclear physics and how to extract physics from the data. We believe this program was very impressive for the students. The authors would like to thank Dr. K. Tanaka, the CNS accelerator group, and the RIBF cyclotron crew for their helpful effort in the present program.

Appendices

Symposium, Workshop, Seminar, and PAC
CNS Reports
Publication List
Talks and Presentations
Awards, Press Releases, and Others
Personnel

Symposium, Workshop, Seminar, and PAC

A. Symposium and Workshop

1. OEDO/SHARAQ collaboration meeting 2020
   on-line, September 7, 2020.

2. International mini-workshop on ”Physics in resonant reaction induced by low-energy RI beam”
   web meeting hosted by CNS, the University of Tokyo/ IBS Center for Exotic Nuclear Studies/ Department of Pure and Applied Physics, Kansai University/ Research Center for Nuclear Physics (RCNP), Osaka University. February 22, 2021.

B. CNS Seminar

1. N. Kitamura (oral), ”In-beam spectroscopy of 30Mg: structural evolution approaching the island of inversion,” CNS seminar, on-line, July 29, 2020.

2. S. Koyama (oral), ”Spectroscopy of resonance states in light proton-rich nuclei via missing mass method,” CNS seminar, on-line, August 7, 2020.

C. Program Advisory Committee for Nuclear-Physics Experiments at RI Beam Factory

1. The 21st NP-PAC meeting
   Date: December 14-16, 2020
   on-line

CNS Reports

#99 "CNS Annual Report 2019"
Edited by H. Nagahama
March, 2021

Publication List

A. Original Papers

1. Z.H. Yang, Y. Kubota, A. Corsi, K. Yoshida, X.-X. Sun, J.G. Li, M. Kimura, N. Michel, K. Ogata, C.X. Yuan, Q. Yuan, G. Authelet, H. Baba, C. Caesar, D. Calvet, A. Delbart, M. Dozono, J. Feng, F. Flavigny, J.-M. Gheller, J. Gibelin, A. Giganon, A. Gillibert, K. Hasegawa, T. Isobe, Y. Kanaya, S. Kawakami, D. Kim, Y. Kiyokawa, M. Kobayashi, N. Kobayashi, T. Kobayashi, Y. Kondo, Z. Korkulu, S. Koyama, V. Lapoux, Y. Maeda, F.M. Marqúes, T. Motobayashi, T. Miyazaki, T. Nakamura, N. Nakatsuka, Y. Nishio, A. Obertelli, A. Ohkura, N.A. Orr, S. Ota, H. Otsu, T. Ozaki, V. Panin, S. Paschalis, E.C. Pollacco, S. Reichert, J.-Y. Roussé, A.T. Saito, S. Sakaguchi, M. Sako, C. Santamaria, M. Sasano, H. Sato, M. Shikata, Y. Shimizu, Y. Shindo, L. Stuhl, T. Sumikama, Y.L. Sun, M. Tabata, Y. Togano, J. Tsubota, F.R. Xu, J. Yasuda, K. Yoneda, J. Zenihiro, S.-G. Zhou, W. Zuo, T. Uesaka, "Quasifree Neutron Knockout Reaction Reveals a Small s-Orbital Component in the Borromean Nucleus ^{17}B," Phys. Rev. Lett. **126**, 082501 (2021).

2. Y. Kubota, A. Corsi, G. Authelet, H. Baba, C. Caesar, D. Calvet, A. Delbart, M. Dozono, J. Feng, F. Flavigny, J.-M. Gheller, J. Gibelin, A. Giganon, A. Gillibert, K. Hasegawa, T. Isobe, Y. Kanaya, S. Kawakami, D. Kim, Y. Kikuchi, Y. Kiyokawa, M. Kobayashi, N. Kobayashi, T. Kobayashi, Y. Kondo, Z. Korkulu, S. Koyama, V. Lapoux, Y. Maeda, F.M. Marqués, T. Motobayashi, T. Miyazaki, T. Nakamura, N. Nakatsuka, Y. Nishio, A. Obertelli, K. Ogata, A. Ohkura, N.A. Orr, S. Ota, H. Otsu, T. Ozaki, V. Panin, S. Paschalis, E.C. Pollacco, S. Reichert, J.-Y. Roussé, A.T. Saito, S. Sakaguchi, M. Sako, C. Santamaria, M. Sasano, H. Sato, M. Shikata, Y. Shimizu, Y. Shindo, L. Stuhl, T. Sumikama, Y.L. Sun, M. Tabata, Y. Togano, J. Tsubota, Z.H. Yang, J. Yasuda, K. Yoneda, J. Zenihiro, T. Uesaka, "Surface Localization of the Dineutron in ^{11}Li," Phys. Rev. Lett. **125**, 252501 (2020).

3. N. Kitamura, K. Wimmer, N. Shimizu, V.M. Bader, C. Bancroft, D. Barofsky, T. Baugher, D. Bazin, J.S. Berryman, V. Bildstein, A. Gade, N. Imai, T. Kröll, C. Langer, J. Lloyd, E. Lunderberg, G. Perdikakis, F. Recchia, T. Redpath, S. Saenz, D. Smalley, S. R. Stroberg, J.A. Tostevin, N. Tsunoda, Y. Utsuno, D. Weisshaar, A. Westerberg, "Structure of ^{30}Mg explored via in-beam γ-ray spectroscopy," Phys. Rev. C **102**, 054318 (2020).

4. S. Momiyama, K. Wimmer, D. Bazin, J. Belarge, P. Bender, B. Elman, A. Gade, K.W. Kemper, N. Kitamura, B. Longfellow, E. Lunderberg, M. Niikura, S. Ota, P. Schrock, J.A. Tostevin, D. Weisshaar, "Shell structure of ^{43}S and collapse of the N = 28 shell closure," Phys. Rev. C **102**, 034325 (2020).

5. Tetsuo Noro, Tomotsugu Wakasa, Takashi Ishida, Hidetomo P. Yoshida, Masahiro Dozono, Hisako Fujimura, Kunihiro Fujita, Kichiji Hatanaka, Takatsugu Ishikawa, Masatoshi Itoh, Junichiro Kamiya, Takahiro Kawabata, Yoshikazu Maeda, Hiroaki Matsubara, Masanobu Nakamura, Harutaka Sakaguchi, Yasuhiro Sakemi, Yohei Shimizu, Hiroyuki Takeda, Yuji Tameshige, Atsushi Tamii, Keisuke Tamura, Satoru Terashima, Makoto Uchida, Yusuke Yasuda, Masaru Yosoi, "Experimental study of $(p,2p)$ reactions at 392 MeV on ^{12}C, ^{16}O, ^{40}Ca and ^{208}Pb nuclei leading to low-lying states of residual nuclei," Prog. Theor. Exp. Phys. **2020**, 093D02 (2020).

6. K.B. Howard, U. Garg, M. Itoh, H. Akimune, M. Fujiwara, T. Furuno, Y.K. Gupta, M.N. Harakeh, K. Inaba, Y. Ishibashi, K. Karasudani, T. Kawabata, A. Kohda, Y. Matsuda, M. Murata, S. Nakamura, J. Okamoto, S. Ota, J. Piekarewicz, A. Sakaue, M.Şenyiğit, M. Tsumura, Y. Yang, "Compressional-mode resonances in the molybdenum isotopes: Emergence of softness in open-shell nuclei near A=90," Phys. Lett. B **807**, 135608 (2020).

7. A. Frotscher, M. Gómez-Ramos, A. Obertelli, P. Doornenbal, G. Authelet, H. Baba, D. Calvet, F. Château, S. Chen, A. Corsi, A. Delbart, J.-M. Gheller, A. Giganon, A. Gillibert, T. Isobe, V. Lapoux, M. Matsushita, S. Momiyama, T. Motobayashi, M. Niikura, H. Otsu, N. Paul, C. Péron, A. Peyaud, E.C. Pollacco, J.-Y. Roussé, H. Sakurai, C. Santamaria, M. Sasano, Y. Shiga, N. Shimizu, D. Steppenbeck, S. Takeuchi, R. Taniuchi, T. Uesaka, H. Wang, K. Yoneda, T. Ando, T. Arici, A. Blazhev, F. Browne, A. M. Bruce, R. Carroll, L.X. Chung, M. L. Cortées, M. Dewald, B. Ding, Zs. Dombradi, F. Flavigny, S. Franchoo, F. Giacoppo, M. Górska, A. Gottardo, K. Hadyńska-Klęk, Z. Korkulu, S. Koyama, Y. Kubota, A. Jungclaus, J. Lee, M. Lettmann, B.D. Linh, J. Liu, Z. Liu, C. Lizarazo, C. Louchart, R. Lozeva, K. Matsui, T. Miyazaki, K. Moschner, S. Nagamine, N. Nakatsuka, C. Nita, S. Nishimura, C.R. Nobs, L. Olivier, S. Ota, Z. Patel, Zs. Podolyák, M. Rudigier, E. Sahin, T.Y. Saito, C. Shand, P.-A. Söderström, I.G. Stefan, T. Sumikama, D. Suzuki, R. Orlandi, V. Vaquero, Zs. Vajta, V. Werner, K. Wimmer, J. Wu, Z. Xu, "Sequential Nature of (p,3p) Two-Proton Knockout from Neutron-Rich Nuclei," Phys. Rev. Lett. **125** 012501 (2020).

8. A.E. Barzakh, D. Atanasov, A.N. Andreyev, M. Al Monthery, N.A. Althubiti, B. Andel, S. Antalic, K. Blaum, T.E. Cocolios, J.G. Cubiss, P. Van Duppen, T. Day Goodacre, A. de Roubin, G.J. Farooq-Smith, D.V. Fedorov, V.N. Fedosseev, D.A. Fink, L.P. Gaffney, L. Ghys, R.D. Harding, M. Huyse, N. Imai, S. Kreim, D. Lunney, K.M. Lynch, V. Manea, B.A. Marsh, Y. Martinez Palenzuela, P.L. Molkanov, D. Neidherr, M. Rosenbusch, R.E. Rossel, S. Rothe, L. Schweikhard, M.D. Seliverstov, S. Sels, C. Van Beveren, E. Verstraelen, A. Welker, F. Wienholtz, R.N. Wolf, K. Zuber, "Shape coexistence in ^{187}Au studied by laser spectroscopy," Phys. Rev. C **101**, 064321 (2020).

9. R.D. Harding, A.N. Andreyev, A.E. Barzakh, D. Atanasov, J.G. Cubiss, P. Van Duppen, M. Al Monthery, N.A. Althubiti, B. Andel, S. Antalic, K. Blaum, T.E. Cocolios, T. Day Goodacre, A. de Roubin, G.J. Farooq-Smith, D. V. Fedorov, V. N. Fedosseev, D.A. Fink, L.P. Gaffney, L. Ghys, D.T. Joss, F. Herfurth, M. Huyse, N. Imai, S. Kreim, D. Lunney, K.M. Lynch, V. Manea, B.A. Marsh, Y. Martinez Palenzuela, P.L. Molkanov, D. Neidherr, R.D. Page, A. Pastore, M. Rosenbusch, R.E. Rossel, S. Rothe, L. Schweikhard, M.D. Seliverstov, S. Sels, C. Van Beveren, E. Verstraelen, A. Welker, F. Wienholtz, R.N. Wolf, K. Zuber "Laser-assisted decay spectroscopy for the ground states of ^{180,182}Au," Phys. Rev. C **102**, 024312 (2020).

10. J.G. Cubiss, A.N. Andreyev, A. E. Barzakh, V. Manea, M. Al Monthery, N.A. Althubiti, B. Andel, S. Antalic, D. Atanasov, K. Blaum, T.E. Cocolios, T. Day Goodacre, A. de Roubin, G.J. Farooq-Smith, D.V. Fedorov, V.N. Fedosseev, D.A. Fink, L.P. Gaffney, L. Ghys, R.D. Harding, F. Herfurth, M. Huyse, N. Imai, D.T. Joss, S. Kreim, D. Lunney, K.M. Lynch, B.A. Marsh, Y. Martinez Palenzuela, P.L. Molkanov, D. Neidherr, G.G. O'Neill, R.D. Page, M. Rosenbusch, R.E. Rossel, S. Rothe, L. Schweikhard, M. D. Seliverstov, S. Sels, A. Stott, C. Van Beveren, P. Van Duppen, E. Verstraelen, A. Welker, F. Wienholtz, R. N. Wolf, K. Zuber, "Laser-assisted decay spectroscopy and mass spectrometry of ^{178}Au," Phys. Rev. C **102**, 044332 (2020).

11. T.L. Tang, T. Uesaka, S. Kawase, D. Beaumel, M. Dozono, T. Fujii, N. Fukuda, T. Fukunaga, A. Galindo-Uribarri, S.H. Hwang, N. Inabe, D. Kameda, T. Kawahara, W. Kim, K. Kisamori, M. Kobayashi, T. Kubo, Y. Kubota, K. Kusaka, C.S. Lee, Y. Maeda, H. Matsubara, S. Michimasa, H. Miya, T. Noro, A. Obertelli, K. Ogata, S. Ota, E. Padilla-Rodal, S. Sakaguchi, H. Sakai, M. Sasano, S. Shimoura, S.S. Stepanyan, H. Suzuki, M. Takaki, H. Takeda, H. Tokieda, T. Wakasa, T. Wakui, K. Yako, Y. Yanagisawa, J. Yasuda, R. Yokoyama, K. Yoshida, K. Yoshida, J. Zenihiro, "How Different is the Core of ^{25}F from $^{24}O_{g.s.}$," Phys. Rev. Lett. **124**, 212502 (2020).

12. S. Michimasa, M. Kobayashi, Y. Kiyokawa, S. Ota, R. Yokoyama, D. Nishimura, D.S. Ahn, H. Baba, G.P.A. Berg, M. Dozono, N. Fukuda, T. Furuno, E. Ideguchi, N. Inabe, T. Kawabata, S. Kawase, K. Kisamori, K. Kobayashi, T. Kubo, Y. Kubota, C.S. Lee, M. Matsushita, H. Miya, A. Mizukami, H. Nagakura, H. Oikawa, H. Sakai, Y. Shimizu, A. Stolz, H. Suzuki, M. Takaki, H. Takeda, S. Takeuchi, H. Tokieda, T. Uesaka, K. Yako, Y. Yamaguchi, Y. Yanagisawa, K. Yoshida, S. Shimoura, "Mapping of a New Deformation Region around ^{62}Ti," Phys. Rev. Lett. **125**, 122501 (2020).

13. D. Nagae, Y. Abe, S. Okada, S. Omika, K. Wakayama, S. Hosoi, S. Suzuki, T. Moriguchi M. Amano, D. Kamioka, Z. Ge, S. Naimi, F. Suzaki, N. Tadano, R. Igosawa, K. Inomata H. Arakawa, K. Nishimuro, T. Fujii, T. Mitsui, Y. Yanagisawa, H. Baba, S. Michimasa, S. Ota, G. Lorusso, Yu.A. Litvinov, A. Ozawa, T. Uesaka, T. Yamaguchi, Y. Yamaguchi, M. Wakasugi, "Development and operation of an electrostatic time-of-flight detector for theRare RI storage Ring," Nucl. Instrum. Methods Phys., Res. Sect. A **986**, 164713 (2021).

14. H. Suzuki, K. Yoshida, N. Fukuda, H. Takeda, Y. Shimizu, D.S. Ahn, T. Sumikama, N. Inabe, T. Komatsubara, H. Sato, Z. Korkulu, K. Kusaka, Y. Yanagisawa, M. Ohtake, H. Ueno, T. Kubo, S. Michimasa, N. Kitamura, K. Kawata, N. Imai, O.B. Tarasov, D. Bazin, J. Nolen, W.F. Henning "Experimental studies of the two-step scheme with an intense radioactive ^{132}Sn beam for next-generation production of very neutron-rich nuclei," Phys. Rev. C **102**, 064615 (2020).

15. T. Sumikama. D.S. Ahn. N. Fukuda, Y. Shimizu, H. Suzuki, H. Takeda, H. Wang, K. Yoshida, J. Amano, N. Chiga, K. Chikaato, A. Hirayama, N. Inabe, S. Kawase, S. Kubono, M. Matsushita, S. Michimasa, K. Nakano, H. Otsu, H. Sakurai, A. Saito, S. Shimoura, J. Suwa, M. Takechi, S. Takeuchi, Y. Togano, T. Tomai, Y. Watanabe, "Energy-control and novel particle-identification methods combined with range in a multi-sampling ionization chamber for experiments using slowed-down RI beams," Nucl. Instrum. Methods Phys., Res. Sect. A **986**, 164687 (2021).

16. Y.L. Sun, T. Nakamura, Y. Kondo, Y. Satou, J. Lee, T. Matsumoto, K. Ogata, Y. Kikuchi, N. Aoi, Y. Ichikawa, K. Ieki, M. Ishihara, T. Kobayshi, T. Motobayashi, H. Otsu, H. Sakurai, T. Shimamura, S. Shimoura, T. Shinohara, T. Sugimoto, S. Takeuchi, Y. Togano, K. Yoneda, "Three-body breakup of ^{6}He and its halo structure," Phys. Lett. B **814**, 136072 (2021).

17. S. Go, E. Ideguchi, R. Yokoyama, N. Aoi, F. Azaiez, K. Furutaka, Y. Hatsukawa, A. Kimura, K. Kisamori, M. Kobayashi, F. Kitatani, M. Koizumi, H. Harada, I. Matea, S. Michimasa, H. Miya, S. Nakamura, M. Niikura, H. Nishibata, N. Shimizu, S. Shimoura, T. Shizuma, M. Sugawara, D. Suzuki, M. Takaki, Y. Toh, Y. Utsuno, D. Verney, A. Yagi, "High-spin states in ^{35}S," Phys. Rev. C **103**, 034327 (2021)

18. G.G. Kiss, M. La Cognata, C. Spitaleri, R. Yarmukhamedov, I. Wiedenhöver, L.T. Baby, S. Cherubini, A. Cvetinović, G. D'Agata, P. Figuera, G.L. Guardo, M. Gulino, S. Hayakawa, I. Indelicato, L. Lamia, M. Lattuada, F. Mudò, S. Palmerini, R.G. Pizzone, G.G. Rapisarda, S. Romano, M.L. Sergi, R. Spartà, O. Trippella, A. Tumino, M. Anastasiou, S.A. Kuvin, N. Rijal, B. Schmidt, S.B. Igamov, S.B. Sakuta, K.I. Tursunmakhatov, Zs. Fülöp, Gy. Gyürky, T. Szücs, Z. Halász, E. Somorjai, Z. Hons, J. Mrázek, R.E. Tribble, A.M. Mukhamedzhanov, "Astrophysical S-factor for the ^{3}He$(\alpha,\gamma)^7$Be reaction via the asymptotic normalization coefficient (ANC) method," Phys. Lett. B **807**, 135606 (2020).

19. L. Yang, C.J. Lin, Y.X. Zhang, P.W. Wen, H.M. Jia, D.X. Wang, N.R. Ma, F. Yang, F.P. Zhong, S.H. Zhong, T.P. Luo, "Bayesian analysis on interactions of exotic nuclear systems," Phys. Lett. B **807**, 135540 (2020).

20. L. Yang, C.J. Lin, H. Yamaguchi, J. Lei, P.W. Wen, M. Mazzocco, N.R. Ma, L.J. Sun, D.X. Wang, G.X. Zhang, K. Abe, S.M. Cha, K.Y. Chae, A. Diaz-Torres, J.L. Ferreira, S. Hayakawa, H.M. Jia, D. Kahl, A. Kim, M.S. Kwag, M. La Commara, R. Navarro Pérez, C. Parascandolo, D. Pierroutsakou, J. Rangel, Y. Sakaguchi, C. Signorini, E. Strano, X.X. Xu, F. Yang, Y.Y. Yang, G.L. Zhang, F.P. Zhong, J. Lubian, "Insight into the reaction dynamics of proton drip-line nuclear system ^{17}F+^{58}Ni at near-barrier energies," Phys. Lett. B **813**, 136045 (2021).

21. N. Iwasa S. Ishikawa, S. Kubono, T. Sakakibara, K. Kominato, K. Nishio, M. Matsuda, K. Hirose, H. Makii, R. Orlandi, K. Asada, D. Guru, S. Nishimura, S. Hayakawa, T. Kawabata, "Experimental study of the $Gamma_{p1}/Gamma_{p0}$ ratios of resonance states in ^{8}Be for deducing the ^{7}Be$(n,p_1)^7$Li* reaction rate relevant to the cosmological lithium problem," Phys. Rev. C **103**, 015801 (2021).

22. D.X. Wang, C.J. Lin, L. Yang, N.R. Ma, L.J. Sun, F. Yang, H.M. Jia, F.P. Zhong, P.W. Wen, "Compact 16-channel integrated charge-sensitive preamplifier module for silicon strip detectors," Nucl. Sci. Tech. **31**, Article number:48 (2020).

23. Y.J. Yao, C.J. Lin, L. Yang, N.R. Ma, D.X. Wang, G.L. Zhang, G.X. Zhang, H.M. Jia, F. Yang, F.P. Zhong, P.W. Wen, X.B. Qin, H.M. Zhao, "Relative probabilities of breakup channels in reactions of ^{6,7}Li with ^{209}Bi at energies around and above the Coulomb barrier," Chin. Phys. C **45**, 054104 (2021).

24. Y.J. Yao, C.J. Lin, L. Yang, N.R. Ma, D.X. Wang, G.L. Zhang, G.X. Zhang, H.M. Jia, F. Yang, "The effects of beam drifts on elastic scattering measured by the large solid-angle covered detector array," Nucl. Sci. Tech. **32**, Article number:14 (2021).

25. ALICE Collaboration (Shreyasi Acharya et al.), "Production of light-flavor hadrons in pp collisions at $\sqrt{s}$ = 7 and $\sqrt{s}$ = 13 TeV," Eur. Phys. J. C **81**, 256 (2021).

26. PHENIX Collaboration (U.A. Acharya et al.), "Transverse single-spin asymmetries of midrapidity π^0 and η mesons in polarized p+p collisions at $\sqrt{s}$ =200 GeV," Phys. Rev. D **103**, 052009 (2021).

27. ALICE TPC Collaboration (J. Adolfsson et al.), "The upgrade of the ALICE TPC with GEMs and continuous readout," J. Instrum. **16**, P03022 (2021).

28. PHENIX Collaboration (U.A. Acharya et al.), "Transverse momentum dependent forward neutron single spin asymmetries in transversely polarized p+p collisions at $\sqrt{s}$ = 200 GeV," Phys. Rev. D **103**, 032007 (2021),

29. ALICE Collaboration (Shreyasi Acharya et al.), "Pion-kaon femtoscopy and the lifetime of the hadronic phase in Pb-Pb collisions at $\sqrt{s_{NN}}$ = 2.76 TeV," Phys. Lett. B **813**, 136030 (2021).

30. ALICE Collaboration (Shreyasi Acharya et al.), "Transverse-momentum and event-shape dependence of D-meson flow harmonics in Pb-Pb collisions at $\sqrt{s_{NN}}$ = 5.02 TeV," Phys. Lett. B **813**, 136054 (2021).

31. ALICE Collaboration (Shreyasi Acharya et al.), "Centrality dependence of J/ψ and ψ(2S) production and nuclear modification in p-Pb collisions at $\sqrt{s_{NN}}$ = 8.16 TeV," J. High Energy Phys. **2102**, 002 (2021).

32. T. Awes et al., "Design and performance of a silicon tungsten calorimeter prototype module and the associated readout," Nucl. Instrum. Methods Phys. Res. A **988**, 164796 (2021).

33. ALICE Collaboration (Shreyasi Acharya et al.), ”Unveiling the strong interaction among hadrons at the LHC,” Nat. Phys. **588**, 232–238 (2020).

34. ALICE Collaboration (Shreyasi Acharya et al.), ”Search for a common baryon source in high-multiplicity pp collisions at the LHC,” Phys. Lett. B **811**, 135849 (2020).

35. PHENIX Collaboration (U. Acharya et al.), “ Production of π^0 and η mesons in U+U collisions at $\sqrt{s_{NN}}$ = 192 GeV,” Phys. Rev. C **102**, 064905 (2020).

36. ALICE Collaboration (Shreyasi Acharya et al.), ”Dielectron production in proton-proton and proton-lead collisions at $\sqrt{s_{NN}}$ = 5.02 TeV,” Phys. Rev. C **102**, 055204 (2020).

37. PHENIX Collaboration (U. Acharya et al.), ”Measurement of jet-medium interactions via direct photon-hadron correlations in Au+Au and d+Au collisions at $\sqrt{s_{NN}}$ = 200 GeV,” Phys. Rev. C **102**, 054910 (2020).

38. ALICE Collaboration (Shreyasi Acharya et al.), ”Elliptic and triangular flow of (anti)deuterons in Pb-Pb collisions at $\sqrt{s_{NN}}$ = 5.02 TeV,” Phys. Rev. C **102**, 055203 (2020).

39. PHENIX Collaboration (U. Acharya et al.), ”Production of b-bbar at forward rapidity in p+p collisions at $\sqrt{s}$ =510 GeV,” Phys. Rev. D **102**, 092002 (2020).

40. PHENIX Collaboration (U. Acharya et al.), ”Polarization and cross section of midrapidity J/ψ production in p+p collisions at $\sqrt{s}$ = 510 GeV,” Phys. Rev. D **102**, 072008 (2020).

41. ALICE Collaboration (Shreyasi Acharya et al.), ”J/ψ elliptic and triangular flow in Pb-Pb collisions at $\sqrt{s_{NN}}$ = 5.02 TeV,” J. High Energy Phys. **2010**, 141 (2020).

42. ALICE Collaboration (Shreyasi Acharya et al.), ”Azimuthal correlations of prompt D mesons with charged particles in pp and p-Pb collisions at $\sqrt{s_{NN}}$ = 5.02 TeV,” Eur. Phys. J. C **80**, 979 (2020).

43. ALICE Collaboration (Shreyasi Acharya et al.), ”Measurement of isolated photon-hadron correlations in $\sqrt{s_{NN}}$ = 5.02 TeV pp and p-Pb collisions,” Phys. Rev. C **102**, 044908 (2020).

44. ALICE Collaboration (Shreyasi Acharya et al.), ”Measurement of the low-energy antideuteron inelastic cross section,” Phys. Rev. Lett. **125**, 162001 (2020).

45. ALICE Collaboration (Shreyasi Acharya et al.), ”J/ψ production as a function of charged-particle multiplicity in p-Pb collisions at $\sqrt{s_{NN}}$ = 8.16 TeV,” J. High Energy Phys. **2009**, 162 (2020).

46. ALICE Collaboration (S. Acharya et al.), ”(Anti-)deuteron production in pp collisions at $\sqrt{s}$ =13 TeV,” Eur. Phys. J. C **80**, 889 (2020).

47. ALICE Collaboration (Shreyasi Acharya et al.), ”Constraining the Chiral Magnetic Effect with charge-dependent azimuthal correlations in Pb-Pb collisions at $\sqrt{s_{NN}}$ = 2.76 and 5.02 TeV,” J. High Energy Phys. **2009**, 160 (2020).

48. ALICE Collaboration (Shreyasi Acharya et al.), ”Z-boson production in p-Pb collisions at $\sqrt{s_{NN}}$ =8.16 TeV and Pb-Pb collisions at $\sqrt{s_{NN}}$ =5.02 TeV,” J. High Energy Phys. **2009**, 076 (2020)

49. ALICE Collaboration (Shreyasi Acharya et al.), ”Multiplicity dependence of J/ψ production at midrapidity in pp collisions at $\sqrt{s}$ = 13 TeV,” Phys. Lett. B **810**, 135758 (2020).

50. ALICE Collaboration (Shreyasi Acharya et al.), ”K*(892)^0 and $\phi(1020)$ production at midrapidity in pp collisions at $\sqrt{s}$ = 8 TeV,” Phys. Rev. C **102**, 024912 (2020).

51. ALICE Collaboration (Shreyasi Acharya et al.), ”Multiplicity dependence of K*(892)^0 and $\phi(1020)$ production in pp collisions at $\sqrt{s}$ =13 TeV ” , Phys. Lett. B **807**, 135501 (2020).

52. ALICE Collaboration (Shreyasi Acharya et al.), ”Global baryon number conservation encoded in net-proton fluctuations measured in Pb-Pb collisions at $\sqrt{s_{NN}}$ = 2.76 TeV,” Phys. Lett. B **807**, 135564 (2020).

53. PHENIX Collaboration (U.A. Acharya et al.), ”Measurement of charged pion double spin asymmetries at midrapidity in longitudinally polarized p+p collisions at $\sqrt{s}$= 510 GeV,” Phys. Rev. D **102**, 032001 (2020).

54. ALICE Collaboration (Shreyasi Acharya et al.), ”Multiplicity dependence of π, K, and p production in pp collisions at $\sqrt{s}$ = 13 TeV,” Eur. Phys. J. C **80**, 693, (2020).

55. ALICE Collaboration (Shreyasi Acharya et al.), ”Measurement of nuclear effects on ψ(2S) production in p-Pb collisions at $\sqrt{s_{NN}}$= 8.16 TeV,” J. High Energy Phys. **2007**, 237 (2020).

56. ALICE Collaboration (Shreyasi Acharya et al.), ”Probing the effects of strong electromagnetic fields with charge-dependent directed flow in Pb-Pb collisions at the LHC,” Phys. Rev. Lett. **125**, 022301 (2020).

57. PHENIX Collaboration (U. Acharya et al.), ”Measurement of J/ψ at forward and backward rapidity in p+p, p+Al, p+Au, and ^{3}He+Au collisions at $\sqrt{s_{NN}}$ =200 GeV,” Phys. Rev. C **102**, 014902 (2020).

58. ALICE Collaboration (Shreyasi Acharya et al.), ”Production of ω mesons in pp collisions at $\sqrt{s}$ = 7 TeV,” Eur. Phys. J. C **80**, 1130 (2020).

59. ALICE Collaboration (Shreyasi Acharya et al.), ”Evidence of Spin-Orbital Angular Momentum Interactions in Relativistic Heavy-Ion Collisions,” Phys. Rev. Lett. **125**, 012301 (2020).

60. ALICE Collaboration (Shreyasi Acharya et al.), ”Non-linear flow modes of identified particles in Pb-Pb collisions at $\sqrt{s_{NN}}$ = 5.02 TeV,” J. High Energy Phys. **2006**, 147 (2020).

61. ALICE Collaboration (Shreyasi Acharya et al.), ”Investigation of the p-Σ^0 interaction via femtoscopy in pp collisions,” Phys. Lett. B **805**, 135419 (2020).

62. ALICE Collaboration (Shreyasi Acharya et al.), ”Centrality and transverse momentum dependence of inclusive J/ψ production at midrapidity in Pb-Pb collisions at $\sqrt{s_{NN}}$ = 5.02 TeV,” Phys. Lett. B **805**, 135434 (2020).

63. ALICE Collaboration (Shreyasi Acharya et al.), ”Measurement of the (anti-)^{3}He elliptic flow in Pb-Pb collisions at $\sqrt{s_{NN}}$ = 5.02 TeV,” Phys. Lett. B **805**, 135414 (2020).

64. ALICE Collaboration (Shreyasi Acharya et al.), ”Coherent photoproduction of ρ^0 vector mesons in ultra-peripheral Pb-Pb collisions at $\sqrt{s_{NN}}$ = 5.02 TeV,” J. High Energy Phys. **2006**, 035 (2020).

65. ALICE Collaboration (Shreyasi Acharya et al.), ”Jet-hadron correlations measured relative to the second order event plane in Pb-Pb collisions at $\sqrt{s_{NN}}$ = 2.76 TeV,” Phys. Rev. C **101**, 064901 (2020).

66. ALICE Collaboration (Shreyasi Acharya et al.), ”Higher harmonic non-linear flow modes of charged hadrons in Pb-Pb collisions at $\sqrt{s_{NN}}$ = 5.02 TeV,” J. High Energy Phys. **2005**, 085 (2020).

67. ALICE Collaboration (Shreyasi Acharya et al.), “ Longitudinal and azimuthal evolution of two-particle transverse momentum correlations in Pb-Pb collisions at $\sqrt{s_{NN}}$ = 2.76 TeV,” Phys. Lett. B **804**, 135375 (2020).

68. ALICE Collaboration (Shreyasi Acharya et al.), ”Measurement of electrons from semileptonic heavy-flavour hadron decays at midrapidity in pp and Pb-Pb collisions at $\sqrt{s_{NN}}$ = 5.02 TeV,” Phys. Lett. B **804**, 135377 (2020).

69. ALICE Collaboration (Shreyasi Acharya et al.), ”Production of charged pions, kaons, and (anti-)protons in Pb-Pb and inelastic pp collisions at $\sqrt{s_{NN}}$ = 5.02 TeV,” Phys. Rev. C **101**, 044907 (2020).

70. ALICE Collaboration (Shreyasi Acharya et al.), ”Production of (anti-)^{3}He and (anti-)^{3}H in p-Pb collisions at $\sqrt{s_{NN}}$ = 5.02 TeV,” Phys. Rev. C **101**, 044906 (2020).

71. ALICE Collaboration (Shreyasi Acharya et al.), ”Underlying Event properties in pp collisions at $\sqrt{s}$=13 TeV,” J. High Energy Phys. **2004**, 192 (2020).

72. ALICE Collaboration (Shreyasi Acharya et al.), ”Global polarization of $\Lambda\ \bar{\Lambda}$ hyperons in Pb-Pb collisions at $\sqrt{s_{NN}}$ = 2.76 and 5.02 TeV,” Phys. Rev. C **101**, 044611 (2020).

73. A. Kastberg, B.K. Sahoo, T. Aoki, Y. Sakemi, B.P. Das, ”Analysis of an Optical Lattice Methodology for Detection of Atomic Parity Nonconservation,” Symmetry **12**, 974 (2020).

74. N. Shimizu, Y. Tsunoda, Y. Utsuno, T. Otsuka, ”The variational approach with the superposition of the symmetry-restored quasi-particle vacua for nuclear shell-model calculaions,” Phys. Rev. C **103**, 014312 (2021).

75. K. Kaneko, N. Shimizu, T. Mizusaki, Y. Sun, ”Triple enhancement of quasi-SU(3) quadrupole collectivity in Strontium-Zirconium N Z isotopes,” Phys. Lett. B **817**, 136286 (2021).

76. S. Go, E. Ideguchi, R. Yokoyama, F. Azaiez, N. Aoi, K. Furutaka, Y. Hatsukawa, A. Kimura, K. Kisamori, M. Kobayashi, F. Kitatani, M. Koizumi, H. Harada, I. Matea, S. Michimasa, H. Miya, S. Nakamura, M. Niikura, H. Nishibata, N. Shimizu, S. Shimoura, T. Shizuma, M. Sugawara, D. Suzuki, M. Takaki, Y. Utsuno, Y. Toh, D. Verney, A. Yagi, "High-spin states in ^{35}S," Phys. Rev. C **103**, 034327 (2021).

77. N. Kitamura, K. Wimmer, N. Shimizu, V.M. Bader, C. Bancroft, D. Barofsky, T. Baugher, D. Bazin, J.S. Berryman, V. Bildstein, A. Gade, N. Imai, T. Koll, C. Langer, J. Lloyd, E. Lunderberg, G. Perdikakis, F. Recchia, T. Redpath, S. Saenz, D. Smalley, S.R. Stroberg, J.A. Tostevin, N. Tsunoda, Y. Utsuno, D. Weisshaar, A. Westerberg "Structure of ^{30}Mg explored via in-beam γ-ray spectroscopy," Phys. Rev. C **102**, 054318 (2020).

78. N. Tsunoda, T. Otsuka, K. Takayanagi, N. Shimizu, T. Suzuki, Y. Utsuno, H. Ueno, "The impact of nuclear shape on the emergence of the neutron dripline," Nature **587**, 66 (2020).

79. K. Kaneko, N. Shimizu, T. Mizusaki, Y. Sun, "Quasi-SU(3) coupling of $(1h_{11/2}, 2f_{7/2})$ across the $N = 82$ shell gap: Enhanced $E2$ collectivity and shape evolution in Nd isotopes," Phys. Rev. C **103**, L021301 (2021).

80. N. Shimizu, T. Togashi, Y. Utsuno, "Gamow-Teller transitions of neutron-rich $N = 82$ and $N = 81$ nuclei by shell-model calculations," Prog. Theor. Exp. Phys. **2021**, 033D01 (2021).

81. K. Yanase, N. Shimizu, "Large-scale shell-model calculations of nuclear Schiff moments of ^{129}Xe and ^{199}Hg," Phys. Rev. C **102**, 065502 (2020).

82. K. Yanase, "Screening of nucleon electric dipole moments in atomic systems," Phys. Rev. C **103**, 035501 (2021).

83. P.A. SÖderstrÖm, L. Capponi, E. Açiksöz, T. Otsuka, N. Tsoneva, Y. Tsunoda, D.L. Balabanski, N. Pietralla, G.L. Guardo, D. Lattuada, H. Lenske, C. Matei, D. Nichita, A. Pappalardo, T. Petruse, "Electromagnetic character of the competitive $\gamma\gamma/\gamma$-decay from ^{137m}Ba,"

84. N. Mărginean, D. Little, Y. Tsunoda, S. Leoni, R.V.F. Janssens, B. Fornal, T. Otsuka, C. Michelagnoli, L. Stan, F.C.L. Crespi, C. Costache, R. Lica, M. Sferrazza, A. Turturica, A.D. Ayangeakaa, K. Auranen M. Barani, P.C. Bender, S. Bottoni, M. Boromiza, A. Bracco, S. Călinescu, C.M. Campbell, M.P. Carpenter, P. Chowdhury, M. Ciemala, N. Cieplicka-Oryǹczak, D. Cline, C. Clisu, H.L. Crawford, I.E. Dinescu, J. Dudouet, D. Filipescu, N. Florea, A.M. Forney, S. Fracassetti, A. Gade, I. Gheorghe, A.B. Hayes, I. Harca, J. Henderson, A. Ionescu, L.W. Iskra, M. Jentschel, F. Kandzia, Y.H. Kim, F.G. Kondev, G. Korschinek, U. Köster, Krishichayan, M. Krzysiek, T. Lauritsen, J. Li, R. Mărginean, E.A. Maugeri, C. Mihai, R.E. Mihai, A. Mitu, P. Mutti, A. Negret, C.R. Niţă, A. Olăcel, A. Oprea, S. Pascu, C. Petrone, C. Porzio, D. Rhodes, D. Seweryniak, D. Schumann, C. Sotty, S.M. Stolze, R. Şuvăilă, S. Toma, S. Ujeniuc, W.B. Walters, C.Y. Wu, J. Wu, S. Zhu, S. Ziliani, "Shape Coexistence at Zero Spin in 64Ni Driven by the Monopole Tensor Interaction," Phys. Rev. Lett. **125**, 102502 (2020).

85. F.L. Bello Garrote, E. Sahin, Y. Tsunoda, T. Otsuka, A. Görgen, M. Niikura, S. Nishimura, G. de Angelis, G. Benzoni, A.I. Morales, V. Modamio, Z.Y. Xu, H. Baba, F. Browne, A.M. Bruce, S. Ceruti, F.C.L. Crespi, R. Daido, M.-C. Delattre, P. Doornenbal, Zs. Dombradi, Y. Fang, S. Franchoo, G. Gey, A. Gottardo, K. Hadyńska-Klęk, T. Isobe, P.R. John, H.S. Jung, I. Kojouharov, T. Kubo, N. Kurz, I. Kuti, Z. Li, G. Lorusso, I. Matea, K. Matsui, D. Mengoni, T. Miyazaki, S. Momiyama, P. Morfouace, D.R. Napoli, F. Naqvi, H. Nishibata, A. Odahara, R. Orlandi, Z. Pate, S. Rice, H. Sakurai, H. Schaffner, L. Sinclair, P.-A. Söderström, D. Sohler, I.G. Stefan, T. Sumikama, D. Suzuki, R. Taniuchi, J. Taprogge, Zs. Vajta, J.J. Valiente-Dobón, H. Watanabe, V. Werner, J. Wu, A. Yagi, M. Yalcinkaya, R. Yokoyama, K. Yoshinaga, "β decay of 75Ni and the systematics of the low-lying level structure of neutron-rich odd-A Cu isotopes," Phys. Rev. C **102**, 034314 (2020).

86. C. Porzio, C. Michelagnoli, N. Cieplicka-Oryńczak, M. Sferrazza, S. Leoni, B. Fornal, Y. Tsunoda, T. Otsuka, S. Bottoni, C. Costache, F.C.L. Crespi, L.W. Iskra, M. Jentschel, F. Kandzia, Y.-H. Kim, U. Köster, N. Mărginean, C. Mihai, P. Mutti, and A. Turturică, "Detailed low-spin spectroscopy of 65Ni via neutron capture reaction," Phys. Rev. C **102**, 064310 (2020).

87. Y. Tsunoda and T. Otsuka, "Triaxial rigidity of ^{166}Er and its Bohr-model realization," Phys. Rev. C **103**, L021303 (2021).

88. A. Kundu, Md.S.R. Laskar, R. Palit, R. Raut, S. Santra, N. Shimizu, T. Togashi, E. Ideguchi, H. Pai, S. Ali, F.S. Babra, R. Banik, S. Bhattacharya, B. Das, P. Dey, R. Donthi, A. Goswami, S. Jadhav, G. Mukherjee, B.S. Naidu, L.P. Singh, S. Rajbanshi, H.P. Sharma, S.S. Tiwary, A.T. Vazhappilly, "New lifetime measurement for the 2_1^+ level of ^{112}Sn by the Doppler Shift Attenuation Method," Phys. Rev. C **103**, 034315 (2021).

89. H. Yamaguchi, D. Kahl, S. Kubono, ”CRIB: The Low Energy In-Flight RI Beam Separator,” Nuclear Physics News International 30, No. 2, 21–27 (2020).

B. Proceedings

1. L. Lamia, R.G. Pizzone, M. Mazzocco, S. Hayakawa, M. La Cognata, C.A. Bertulani, S. Cherubini, G. D ’ Agata, G.L. Guardo, M. Gulino, I. Indelicato, G.G. Rapisarda, S. Romano, M.L. Sergi, R. Spartà, C. Spitaleri, A. Tumino, Journal of Physics: Conference Series **1643**, 012096 (2020).

2. A. Inoue, A. Tamii, P. Chan, S. Hayakawa, N. Kobayashi, Y. Maeda, K. Nonaka, T. Shima, H. Shimizu, D.T. Tran, X. Wang, H. Yamaguchi, L. Yang, Z. Yang, Journal of Physics: Conference Series **1643**, 012049 (2020).

3. H. Yamaguchi, S. Hayakawa, N. Ma, H. Shimizu, L. Yang, D. Kahl, K. Abe, T. Suhara, N. Iwasa, A. Kim, D. Kim, S. Cha, M. Kwag, J. Lee, E. Lee, K. Chae, Y. Wakabayashi, N. Imai, N. Kitamura, P. Lee, J. Moon, K. Lee, C. Akers, H. Jung, N. Duy, L. Khiem, C. Lee, S. Cherubini, M. Gulino, C. Spitaleri, G. Rapisarda, L. Cognata, L. Lamia, S. Romano, A. Coc, N. de Sereville, F. Hammache, G. Kiss, S. Bishop, T. Teranishi, T. Kawabata, Y. Kwon, D. Binh, Journal of Physics: Conference Series **1643**, 012069 (2020).

4. M. Mazzocco, N. Keeley, A. Boiano, C. Boiano, M.L. Commara, A. Lagni, C. Manea, C. Parascandolo, D. Pierroutsakou, C. Signorini, E. Strano, D. Torresi, H. Yamaguchi, D. Kahl, L. Acosta, D. Meo, J.P. Fernandez-Garcia, T. Glodariu, J. Grebosz, A. Guglielmetti, Y. Hirayama, N. Imai, H. Ishiyama, N. Iwasa, S.C. Jeong, H.M. Jia, Y.H. Kim, S. Kimura, S. Kubono, G.L. Rana, C.J. Lin, P. Lotti, G. Marquínez-Duran, I. Martel, H. Miyatake, M. Mukai, T. Nakao, M. Nicoletto, A. Pakou, K. Rusek, Y. Sakaguchi, A.M. Sanchez-Benitez, T. Sava, O. Sgouros, V. Soukeras, F. Soramel, E. Stiliaris, L. Stroe, T. Teranishi, N. Toniolo, Y. Wakabayashi, Y.X. Watanabe, L. Yang, Y.Y. Yang, H.Q. Zhang, Journal of Physics: Conference Series **1643**, 012096 (2020).

5. H. Yamaguchi, S. Hayakawa, L. Yang, H. Shimizu, D. Kahl, T. Suhara, N. Iwasa, S.M. Cha, M.S. Kwag, J.H. Lee, E.J. Lee, K.Y. Chae, A. Kim, D.H. Kim, Y. Wakabayashi, N. Imai, N. Kitamura, P. Lee, J.Y. Moon, K.B. Lee, C. Akers, N.N. Duy, L.H. Khiem, C.S. Lee, JPS Conf. Proc. **32**, 010055 (2020).

6. S. Hayakawa, L. Lamia, C. Spitaleri, C.A. Bertulani, S.Q. Hou, M.L. Cognata, M. Mazzocco, R.G. Pizzone, D. Pierroutsakou, S. Romano, M.L. Sergi, A. Tumino, JPS Conf. Proc. **32**, 010058 (2020).

7. R.G. Pizzone, G. D ’ Agata, I. Indelicato, M.L. Cognata, P. Figuera, G.L. Guardo, S. Hayakawa, L. Lamia, M. Lattuada, M. Milin, G.G. Rapisarda, S. Romano, M.L. Sergi, N. Skukan, N. Soic, C. Spitaleri, A. Tumino, JPS Conf. Proc. **32**, 010062 (2020).

8. A. Tumino, C. Spitaleri, M.L. Cognata, S. Cherubini, G.L. Guardo, M. Gulino, S. Hayakawa, I. Indelicato, L. Lamia, H. Petrascu, R.G. Pizzone, S.M.R. Puglia, G.G. Rapisarda, S. Romano, M.L. Sergi, R. Sparta, L. Trache, Proceedings of 13th International Conference on Nucleus-Nucleus, JPS Conf. Proc. **32**, 010059 (2020).

9. Y. Kotaka, Y. Ohshiro, H. Yamaguchi, N. Imai, Y. Sakemi, S. Shimoura, T. Nagatomo, J. Ohnishi, T. Nakagawa, M. Kase, A. Goto, K. Hatanaka, H. Muto, ”Development of the calculation method of injection beam trajectory of RIKEN AVF Cyclotron with 4D emittance measured by the developed pepper-pot emittance monitor,” Proceedings of the 8th International Beam Instrumentation Conference (IBIC2019), JACoW-IBIC2019-TUPP022 (2020).

10. Y. Sakemi, T. Aoki, R. Calabrese, H. Haba, K. Harada, T. Hayamizu, Y. Ichikawa, K. Jungmann, A. Kastberg, Y. Kotaka, Y. Matsuda, H. Nagahama, K. Nakamura, M. Otsuka, N. Ozawa, K.S. Tanaka, A. Uchiyama, H. Ueno, L. Willmann, ”Fundamental physics with cold radioactive atoms,” AIP Conference Proceedings **2319**, 080020 (2021).

C. Theses

1. S. Hanai: ”Development of heavy-ion tracking detector with fast readout of electron avalanche”: Master thesis, the University of Tokyo. March 2020.

2. N. Shimizu: "Search for Exotic Strange Hadrons at the LHC–ALICE": Master thesis, the University of Tokyo, March 2020.

Talks and Presentations

A. International Conference

1. N. Imai (invited), ”Preparation status of NP1912-SHARAQ18,” OEDO/SHARAQ collabotration meeting 2020, on-line, September 7, 2020.
2. S. Michimasa (invited), ”Mapping background X-rays from OEDO RFD,” OEDO/SHARAQ collabotration meeting 2020, on-line, September 7, 2020.
3. M. Dozono (invited), ”Probing exotic structures of highly excited nuclei: OEDO-SHARAQ activities,” RIBF user meeting, on-line, September 8–10, 2020
4. S. Michimasa (invited), ”Development of energy-degraded RI beam and expansion of nuclear reaction studies,” Symposium of Nuclear Data 2020 (hybrid), Saitama, Japan, November 26–27, 2020.
5. S. Ota (invited), ”Study of nuclear matter property via nuclear scattering and reactions,” JPS/NRF/NSFC A3 Foresight Program ”Nuclear Physics in the 21st Century” Joint Annual Meeting, Huizhou, China and on-line, November 18–19, 2020.
6. H. Yamaguchi (oral), ”Activities at the low-energy RI beam separator CRIB,” RIBF Users Meeting 2020 (on-line), Saitama, Japan, Sepember 8–10, 2020.
7. H. Yamaguchi (oral), ”Overview of alpha resonant scattering experiments at CRIB,” International mini-workshop on “Physics in resonant reaction induced by low-energy RI beam”, web meeting hosted by CNS, the University of Tokyo/IBS Center for Exotic Nuclear Studies/Department of Pure and Applied Physics, Kansai University/Research Center for Nuclear Physics (RCNP), Osaka, Japan, February 22, 2021.
8. N.R. Ma (oral), ”Primary result of 14O+α clustering study at CRIB,” International mini-workshop on “Physics in resonant reaction induced by low-energy RI beam”, web meeting hosted by CNS, the University of Tokyo/IBS Center for Exotic Nuclear Studies/Department of Pure and Applied Physics, Kansai University/Research Center for Nuclear Physics (RCNP), Osaka, Japan, February 22, 2021.
9. D. Sekihata for the ALICE Collaboration (oral), “Low-mass dielectron measurements in pp, p-Pb and Pb-Pb collisions with ALICE at the LHC,” 10th International Conference on Hard and Electromagnetic Probes of High-Energy Nuclear Collisions, online, June.2020.
10. T. Hayamizu (oral), ”Development of ultracold francium atomic sources towards the permanent EDM search,” Yamada Conference LXXII: The 8th Asia-Pacific Conference on Few-Body Problems in Physics (APFB2020), Kanazawa, Japan, March 4, 2021.
11. N. Shimizu (oral), ”Data-driven approaches in nuclear shell-model calculations,” Nuclear data symposium 2020 (RIKEN Nishina Center), Saitama, Japan, November 27, 2020.
12. Y. Tsunoda (invited), ”Structure of Medium-mass Nuclei Studied by Monte Carlo Shell Model Calculations,” The RIBF Users Meeting 2020, online, September 9, 2020.
13. Y. Tsunoda (oral), ”Nuclear shapes and collective motions in the region of Sm,” 12th symposium on Discovery, Fusion, Creation of New Knowledge by Multidisciplinary Computational Sciences, online, October 6, 2020.
14. K. Yanase (oral), ”Large-scale shell-model calculations of nuclear Schiff moments of 129Xe and 199Hg,” Beyond-the-Standard-Model Physics with Nucleons and Nuclei (INT 20-2b), online, July 23, 2020.

B. Domestic Conference

1. 今井伸明 (招待講演), [不安定核の中性子捕獲率測定プロジェクト」, 研究会「星の錬金術から銀河考古学へ」, 東京都三鷹市（国立天文台）, 2020 年 10 月 26–29 日.

2. 下浦亨（招待講演）, ”Direct Reactions as Quantum Probes of Nuclear System,” Symposium on ”JPS Nuclear Physics and Physical Review C”, 日本物理学会 2020 年秋季大会, オンライン, 2020 年 9 月 14 日–17 日.

3. 花井周太郎 (口頭発表), 「分割電極型 PPAC(SR-PPAC) における位置較正手法の開発」, 日本物理学会 2020 年秋季大会, on-line, 2020 年 9 月 14 日–17 日.

4. 道正新一郎（口頭発表）, 「中性子過剰 ^{62}Ti 核および近傍核の質量測定」, 日本物理学会 第 76 回年次大会, オンライン講演, 2021 年 3 月 12–15 日.

5. 堂園昌伯（口頭発表）, 「(^{4}He,^{6}He) 反応による錫同位体の対振動状態の研究」, 日本物理学会 第 76 回年次大会, オンライン講演, 2021 年 3 月 12–15 日.

6. 郡司卓（招待講演）, ”ALICE Upgrade and Physics Topics (II),” 第 4 回クラスター階層領域研究会, オンライン講演, 2020 年 5 月 28 日.

7. 関畑大貴（口頭発表）, 「機械学習を用いた ALICE-TPC 検出器内部の空間電荷効果補正」, MPGD & Active 媒質 TPC 研究会 2020（神戸大学+オンライン）, 兵庫県神戸市, 2020 年 12 月.

8. 関畑大貴 for the ALICE Collaboration（口頭発表）, 「機械学習を用いた ALICE-TPC 検出器内部の空間電荷効果補正」, 日本物理学会 第 76 回年次大会, オンライン講演, 2021 年 3 月 12–15 日.

9. 関畑大貴（基調講演）, 「核子対あたり重心系エネルギー 5.02 における中性中間子と直接光子測定」(受賞記念企画公演), 日本物理学会 第 76 回年次大会, オンライン講演, 2021 年 3 月 12–15 日.

10. 関口裕子 for the ALICE Collaboration（口頭発表）, 「LHC-ALICE 実験を用いた小さな衝突系における方位角異方性の擬ラピディティ依存性測定」, 日本物理学会 第 76 回年次大会, オンライン講演, 2021 年 3 月 12–15 日.

11. 清水夏輝 for the ALICE Collaboration （口頭発表）, 「ALICE 実験における Run2 全統計を用いたエキゾチックハドロン探索」, 日本物理学会 第 76 回年次大会, オンライン講演, 2021 年 3 月 12–15 日.

12. 佐藤幹（口頭発表）, 「高効率フランシウム原子線のための吸着防止コーティング材の評価」, 日本物理学会 第 76 回年次大会, オンライン講演, 2021 年 3 月 12–15 日.

13. 君塚大樹（口頭発表）, 「狭線幅光会合を用いた極低温 Sr_2 分子生成のための高安定な光源開発」, 日本物理学会 第 76 回年次大会, オンライン講演, 2021 年 3 月 12–15 日.

14. 池田英彦（口頭発表）, 「電場の量子センシングに向けた Sr リドベルグ原子の分光」, 日本物理学会 第 76 回年次大会, オンライン講演, 2021 年 3 月 12–15 日.

15. 小澤直也（口頭発表）, 「フランシウム原子の電気双極子能率探索のための表面電離イオン源の開発」, 日本物理学会 第 76 回年次大会, オンライン講演, 2021 年 3 月 12–15 日.

16. 鎌倉惠太 (Oral), 「東大 HyperECR イオン源の現状」, 第 19 回 AVF 合同打ち合わせ, オンライン講演, 2021 年 3 月 10 日.

17. 小高康照 (Oral), 「理研 AVF のビーム輸送系最適化の現状」, 第 19 回 AVF 合同打ち合わせ, オンライン講演, 2021 年 3 月 10 日.

18. 清水則孝（口頭発表）, 「準粒子真空基底によるモンテカルロ殻模型の拡張」, 日本物理学会 第 76 回年次大会, オンライン講演, 2021 年 3 月 12–15 日.

19. 角田佑介（口頭発表）, 「モンテカルロ殻模型による二重ベータ崩壊の核行列要素の計算」, 新学術領域「地下宇宙」2020 年度領域研究会、オンライン講演, 2020 年 6 月 2 日.

20. 角田佑介（口頭発表）, 「モンテカルロ殻模型による二重ベータ崩壊の核行列要素の計算」, 日本物理学会 第 76 回年次大会, オンライン講演, 2021 年 3 月 12–15 日.

21. 柳瀬宏太（口頭発表）, 「原子核殻模型による電気双極子モーメントの精密計算」, 「富岳で加速する素粒子・原子核・宇宙・惑星」シンポジウム, オンライン講演, 2021 年 1 月 28 日.

22. 柳瀬宏太（口頭発表）, 「清水則孝、原子核殻模型による電気双極子モーメントの精密計算」, 日本物理学会 第 76 回年次大会, オンライン講演, 2021 年 3 月 12–15 日.

C. Lectures

1. Y. Sakemi, H. Yamaguchi: ”Nuclear Physics III”, Summer, 2020.
2. T. Gunji (with K. Fukushima, K. Ozawa, H. Liang): ”Hadron Physics”, Summer, 2020.
3. K. Yako (with M. Yokoyama): ”Experimental Techniques in Particle and Nuclear Physics”, Summer, 2020.
4. N. Imai: ”Nuclear Physics I/II”, Autumn, 2020.
5. K. Yako: ”Classical mechanics A for undergraduate students”, Summer, 2020.
6. S. Ota: ”Physics Experiment II”, Autumn, 2020.

Awards, Press Releases, and Others

A. Awards

1. 関畑大貴, 第 15 回日本物理学会若手奨励賞 (実験核物理領域).
2. 関畑大貴, 第 27 回原子核談話会新人賞.

B. Press Releases

1. 道正新一郎, 小林幹, 下浦享, 上坂友洋, 井手口栄治, 西村太樹, 「チタン同位体でおこる新たな安定化現象を発見—質量測定で迫る原子核存在限界」, 2020 年 9 月 16 日.
2. 大塚孝治, 角田直文, 高柳和雄, 清水則孝, 鈴木俊夫, 宇都野穣, 吉田聡太, 上野秀樹, 「原子核の存在限界（中性子ドリップライン）の新たなメカニズム」, 2020 年 11 月 5 日, https://www.s.u-tokyo.ac.jp/ja/press/2020/7074/

C. Others

1. 道正新一郎, 「質量から探る原子核の秩序と存在限界」, 学部生に伝える研究最前線, 東京大学理学部ニュース 2021 年 1 月号.

Personnel

Director

SHIMOURA, Susumu	*Professor, Graduate School of Science* *Center for Nuclear Study*

Scientific Staff

SAKEMI, Yasuhiro	*Professor*
YAKO, Kentaro	*Associate Professor*
IMAI, Nobuaki	*Associate Professor*
GUNJI, Taku	*Associate Professor*
SHIMIZU, Noritaka	*Project Associate Professor*
YAMAGUCHI, Hidetoshi	*Lecturer*
MICHIMASA, Shin'ichiro	*Assistant Professor*
OTA, Shinsuke	*Assistant Professor*
NAGAHAMA, Hiroki	*Assistant Professor*

Guest Scientists

UTSUNO, Yutaka	*JAEA*
NISHIMURA, Daiki	*Tokyo City University*
KAJINO, Toshitaka	*NAOJ*
HAMAMOTO, Ikuko	*Lund University*

Technical Staff

KOTAKA, Yasuteru

Technical Assistants

YAGYU, Masayoshi

Project Research Associates

DOZONO, Masanori
HAYAKAWA, Seiya

Post Doctoral Associates

SEKIHATA, Daiki
NAKAMURA, Keisuke
KAMAKURA, Keita
Ma, Nanru
TSUNODA, Yusuke
YANASE, Kota
CHILLERY, Thomas William

Academic Support Staff

KOJIMA, Reiko

Assistant Teaching Staff

SEKIGUCHI, Yuko
KAWATA, Keita
KITAMURA, Noritaka
KOYAMA, Shumpei

Graduate Students

MASUOKA, Shoichiro
SHIMIZU, Hideki
TSUNODA, Rieko
OZAWA, Naoya
HANAI, Shutaro
SHIMIZU, Natsuki
NAGASE, Shintaro
KOHARA, Ryotaro

Research Student

LI, Jiatai

Administration Staff

SHIMANE, Noriko
YAMAMOTO, Ikuko
ENDO, Takako
KISHI, Yukino

Committees

Steering Committee

TAKEDA, Hiroyuki	*Department of Physics, Graduate School of Science, UT*
HOSHINO, Masahiro	*Department of Earth and Planetary Physics, Graduate School of Science, UT*
YAMAMOTO, Satoshi	*Department of Physics, Graduate School of Science, UT*
SAKURAI, Hiroyoshi	*Department of Physics, Graduate School of Science, UT*
MORI, Toshinori	*International Center for Elementary Particle Physics, UT*
TAKAHASHI, Hiroyuki	*Department of Nuclear Engineering and Management, Graduate School of Engineering, UT*
SHIMOURA, Susumu	*Center for Nuclear Study, Graduate School of Science, UT*
SAKEMI, Yasuhiro	*Center for Nuclear Study, Graduate School of Science, UT*
YAKO, Kentaro	*Center for Nuclear Study, Graduate School of Science, UT*
TAMURA, Hirokazu	*Department of Physics, Graduate School of Science, Tohoku University*